

$^{19}\text{F}(p,\gamma)^{20}\text{Ne}$  AND THE STELLAR CNO BURNING CYCLE

A Dissertation

Submitted to the Graduate School  
of the University of Notre Dame  
in Partial Fulfillment of the Requirements  
for the Degree of

Doctor of Philosophy

by

Aaron Couture, B.Sc., M.Sc.

---

Michael Wiescher, Director

Graduate Program in Physics

Notre Dame, Indiana

December 2005

# $^{19}\text{F}(\text{p},\gamma)^{20}\text{Ne}$ AND THE STELLAR CNO BURNING CYCLE

Abstract

by

Aaron Couture

A new measurement of the  $^{19}\text{F}(\text{p},\gamma)$  breakout reaction to CNO cycle has been completed at the University of Notre Dame, covering energies from 200-800 keV. The sensitivity of the measurement is a significant improvement over past measurements, including measurements of sufficient accuracy to observe previously unmeasured interference terms. As part of the development for the measurements, an particle accelerator of nuclear astrophysics was refurbished and installed in the Nuclear Structure Laboratory at the University of Notre Dame. A gamma-ray detector system was designed for isolating high Q-value reactions in a strong gamma-ray background.

The new measurements decreased the resonance strengths for the  $^{19}\text{F}(\text{p},\gamma)$  reaction which decrease the stellar reaction rate by a factor of four. As  $^{19}\text{F}(\text{p},\gamma)$  represents the only possible breakout path from the cold CNO cycle, this confirmed that the CNO cycle is closed in typical stellar burning scenarios.

To Jennifer,  
who makes the sun rise and the stars shine.

## CONTENTS

FIGURES . . . . .	v
TABLES . . . . .	vii
ACKNOWLEDGMENTS . . . . .	viii
CHAPTER 1: INTRODUCTION . . . . .	1
1.1 Stellar Burning Scenarios . . . . .	9
1.1.1 Hydrogen Burning Cycles . . . . .	10
1.2 Stellar Reaction Rates . . . . .	14
1.3 Relating Reaction Rates to Laboratory Measurements . . . . .	23
1.4 Reaction Networks . . . . .	25
1.5 The Status of $^{19}\text{F} + p$ . . . . .	27
1.5.1 The Sinclair Measurement . . . . .	28
1.5.2 The Farney Measurement . . . . .	28
1.5.3 The Berkes Measurement . . . . .	29
1.5.4 The Subotić Measurement . . . . .	30
1.5.5 The Present Status . . . . .	32
CHAPTER 2: EXPERIMENTAL APPARATUS AND PROCEDURE . . . . .	33
2.1 Detector Types . . . . .	34
2.2 The BaF <sub>2</sub> Experiment . . . . .	36
2.2.1 Detector Array . . . . .	37
2.2.2 Accelerator . . . . .	38
2.2.3 Targets and Charge Collection . . . . .	39
2.2.4 Electronics . . . . .	41
2.3 The NaI(Tl) Experiment . . . . .	47
2.3.1 The JN Van de Graaff Accelerator . . . . .	48
2.3.2 Detector Array . . . . .	57
2.3.3 Electronics . . . . .	61
2.3.4 Target Production and Monitoring . . . . .	62

CHAPTER 3: DATA REDUCTION AND ANALYSIS . . . . .	69
3.1 Experimental Systematics . . . . .	69
3.1.1 Detector Calibration . . . . .	70
3.1.2 Corrections for Target Degradation . . . . .	75
3.1.3 Efficiency Calculations . . . . .	81
3.2 Fitting Systematics . . . . .	93
3.2.1 Yield Extraction . . . . .	98
3.2.2 The Fitting Function . . . . .	98
3.2.3 The Fitting Methodology . . . . .	103
3.3 Determination of Uncertainty . . . . .	110
3.3.1 Statistical Uncertainties . . . . .	110
3.3.2 Fitting Uncertainties . . . . .	111
3.3.3 Systematic Uncertainties . . . . .	111
3.4 Resonance Parameters . . . . .	113
CHAPTER 4: RESULTS AND CONCLUSIONS . . . . .	115
4.1 Comparison of Resonance Parameters . . . . .	115
4.2 Astrophysical Implications . . . . .	120
APPENDIX A: ELECTRONICS ABBREVIATIONS . . . . .	124
APPENDIX B: CNO NETWORK . . . . .	126
APPENDIX C: MAGNET REFRESHING PROCEDURE . . . . .	129
APPENDIX D: SUMMING CORRECTION COEFFICIENTS . . . . .	130
D.1 $^{28m}\text{Si}$ , $E_x^R=12239.4$ keV . . . . .	130
D.2 $^{60}\text{Co} \rightarrow ^{60m}\text{Ni}$ , $E_x=2505.7$ keV . . . . .	134
APPENDIX E: JN RUNNING PARAMETERS . . . . .	136

## FIGURES

1.1	Carbon Burning Stellar Structure . . . . .	4
1.2	Solar System Abundance Distribution . . . . .	6
1.3	The pp Chains . . . . .	11
1.4	CNO Cycle . . . . .	13
2.1	$^{20}\text{Ne}$ Level Diagram . . . . .	34
2.2	BaF <sub>2</sub> Array Images . . . . .	37
2.3	BaF <sub>2</sub> Trigger Generation Schematic . . . . .	43
2.4	BaF <sub>2</sub> Gate Schematic . . . . .	44
2.5	BaF <sub>2</sub> Shaping Schematic . . . . .	44
2.6	BaF <sub>2</sub> Yield Curve . . . . .	46
2.7	JN Beamline Schematic . . . . .	49
2.8	Ion Source Control Interface . . . . .	52
2.9	Acceleration and Optics Control Interface . . . . .	53
2.10	Beam Metering Interface . . . . .	54
2.11	JN Energy Calibration . . . . .	56
2.12	JN Energy Reproducibility . . . . .	58
2.13	NaI(Tl) Array Images . . . . .	60
2.14	NaI(Tl) Trigger Schematic . . . . .	63
2.15	NaI(Tl) Master Trigger Schematic . . . . .	64
2.16	NaI(Tl) Shaping Schematic . . . . .	64
2.17	NaI(Tl) Thin Target Yield Curve . . . . .	68
3.1	HPGe Energy Calibration . . . . .	72

3.2	NaI(Tl) Energy Calibration . . . . .	73
3.3	Target Degradation Effects . . . . .	76
3.4	FWHM v. $Q_T$ . . . . .	79
3.5	Plateau Loss v. $Q_T$ . . . . .	80
3.6	Area v. Charge . . . . .	82
3.7	Sum Energy Spectra . . . . .	84
3.8	Detector Face for Summing Correction . . . . .	89
3.9	Absolute Photopeak Efficiency . . . . .	90
3.10	Single and Double Escape Efficiencies . . . . .	91
3.11	Gamma-ray Singles Spectrum, $E_{cm}=632$ keV . . . . .	94
3.12	Gamma-ray Gated Spectrum, $E_{cm}=632$ keV . . . . .	95
3.13	Gamma-ray Singles Spectrum, $E_{cm}=324$ keV . . . . .	96
3.14	Gamma-ray Gated Spectrum, $E_{cm}=324$ keV . . . . .	97
3.15	Resonant Yield Example . . . . .	100
3.16	Interference Yield Example . . . . .	101
3.17	Fit to $^{19}\text{F}(p,\gamma_1)$ . . . . .	106
3.18	Fit to $^{19}\text{F}(p,\alpha_2)$ . . . . .	107
3.19	Fit to $^{19}\text{F}(p,\alpha_3)$ . . . . .	108
3.20	Fit to $^{19}\text{F}(p,\alpha_3)$ . . . . .	109
4.1	Predicted Yield for $\Gamma_{\gamma_1}=12$ eV . . . . .	119
4.2	Astrophysical Reaction Rate for $^{19}\text{F}(p,\gamma)$ . . . . .	121
4.3	Stellar $^{20}\text{Ne}$ Production . . . . .	122
D.1	$^{28m}\text{Si}$ Decay Schematic, $E_x^R=12239.4$ keV . . . . .	131
D.2	$^{60m}\text{Ni}$ Decay Schematic, $E_x=2505.7$ keV . . . . .	134

## TABLES

1.1	SOLAR SYSTEM ABUNDANCES OF SELECTED ELEMENTS . .	15
1.2	COULOMB BARRIER FOR PROTON CAPTURE ON SELECTED ISOTOPES . . . . .	16
1.3	PRIOR MEASUREMENTS OF RESONANCE PARAMETERS . .	31
2.1	DETECTOR PROPERTIES . . . . .	36
2.2	TARGET PARAMETERS . . . . .	66
3.1	GAMMA-RAY CALIBRATION ENERGIES . . . . .	71
3.2	DETECTOR ENERGY CALIBRATION . . . . .	74
3.3	DATASETS USED FOR RESONANCE CONTRIBUTIONS . . . .	106
3.4	LORENZ-WIRZBA RESONANCE STRENGTHS . . . . .	112
3.5	DEDUCED RESONANCE PARAMETERS . . . . .	114
4.1	COMPARISON OF MEASUREMENTS OF RESONANCE PARAMETERS . . . . .	116
A.1	ELECTRONICS ABBREVIATIONS . . . . .	125
D.1	$^{28m}\text{Si}$ DECAY SUMMING PARAMETERS, $E_x^R=12239.4$ keV . . . .	132
D.2	$^{60m}\text{Ni}$ DECAY SUMMING PARAMETERS, $E_x=2505.7$ keV . . . .	135
E.1	JN RUNNING PARAMETERS . . . . .	137

## ACKNOWLEDGMENTS

This work was only possible through the help and friendship of many people to whom I owe a great debt.

Almost twelve years ago, I watched as a slip of paper with my name on it fluttered down, likely to be swallowed by the precariously arranged books, after having met my now advisor, Dr. Michael Wiescher, for the first time, not expecting to him to ever find me again or the paper again, nor having any concept of the world to which he would introduce me. His guidance and insight have been invaluable. Michael's passion and brilliance continue to both humble and inspire me.

Dr. Joachim Görres provided continual advice and expertise in how to improve and optimize every aspect of the experiment and analysis. In addition to the treasure of technique which I have learned from him, I will carry with me a standard by which to judge the quality of scientific work.

Dr. Jason Daly and Dr. Edward Stech have, in many ways, helped to make graduate school livable. I am indebted to them for their friendship and the many conversations and perspectives, both on physics and without, that have made this journey possible. Here's to the end of another, well, week.

To my many collaborators over the years: Dr. Steve Graff, who introduced me to Van de Graaff accelerators, Dr. Michael Heil and Dr. Rene Reifarh, who first introduced my to the wonders of GEANT simulations, Dr. Richard Azuma who gave me much insight into the behavior of fitting functions, penetrabilities, and computational techniques, Dr. Claudio Ugalde, Hye-Young Lee, Elizabeth Strand-

berg, Dr. Manoël Couder, Dr. Wanpeng Tan, Annalia Palumbo, Shawn O'Brien, and P. J. LeBlanc for the assistance in the running of the experiments, thank you much. Ethan Uberseder gave the project needed assistance and energy when it was lagging. I am indebted to Dr. Larry Lamm and Mr. Bradley Mulder for their many useful discussions and suggestions regarding the installation of the JN accelerator at Notre Dame. My thanks as well to Mr. Jim Kaiser, Mr. Jerry Lingle, and Mr. Charlie Guy at the Nuclear Structure Laboratory for their work in keeping the ancillary systems, whether electronic or mechanical, in running order so that this work could be done.

Last, but most definitely not least, I am indebted to my family. My wife Jennifer has been a sounding board for ideas, a support when things were falling apart, a stalwart companion on this journey, and always, an inspiration. My daughter, Mary, though she might not yet know it has been a motivation and delightful distraction.

Thank you, all.

## CHAPTER 1

### INTRODUCTION

Since the Greeks looked to the heavens, watching Apollo's fiery chariot race across the skies, we have wondered as to the nature and power of the sun and the stars above us. Theories for the power driving the light and energy we see from the sun have evolved as our understanding of the world around us has changed. Early theories of a wood fired sun gave way to the coal powered sun, both falling to the theory that the energy of the sun was powered by gravitational attraction in the 1800's. Unfortunately, none of these theories could account for the longevity of the lifetime of the stars.

Finally, in 1920, Eddington proposed that the sun was supported against gravitational collapse by the energy released from the nuclear fusion of four protons to form a helium atom [22]. The difference in mass of these isotopes is converted directly into the energy that supports and heats the sun as well as life here on earth. In 1938, Hans Bethe proposed the CN cycle as an alternative method to convert hydrogen into helium, using carbon and nitrogen isotopes as catalysts [9]. These seeds have continued to drive our understanding of the lifetimes of stars to this day. The details have been refined, but the core concept is still how stars are explained today. This gave us a glimpse of the critical roles stars play in our lives. Yet, stars do even more. Further investigation of the burning processes and stellar evolution showed that they are no less than the foundries in which are forged the elements

of our selves, our world, and our imaginations. Almost all of the elements except hydrogen and helium were created in their fiery furnaces.

In 1957, Burbidge, Burbidge, Fowler and Hoyle published a review entitled “Synthesis of the Elements in the Stars” which gathered and synthesized the understanding at that time of both the life cycles of the stars and how those lives affected the production of the chemical elements observed in the cosmos [13]. This seminal paper (ubiquitously known as B<sup>2</sup>FH) has largely guided the development and evolution of nuclear astrophysics for almost 50 years. The following discussion both of stellar burning and element synthesis is drawn from their discussion except if noted otherwise. The stellar evolution will be addressed first, followed by a discussion of the nucleosynthesis that can take place during each stage.

The proto-star is formed from the collapse of gravitationally bound gasses available in the environs of the proto-star. For Population I stars, or stars formed after the early universe, the initial composition of material is basically a solar distribution, predominantly hydrogen and helium, with a small percentage (<1%) of carbon, nitrogen, and oxygen, and trace amounts of individual heavier elements (typically ranging from 0.01-100 parts per million) [36]. This gravitational collapse will continue until there is some counter-balancing force to stop it. The condensation increases the temperature and pressure of the material in the core until it is hot enough for nuclear reactions to begin. The first reactions are those with the lowest barrier to overcome, namely, hydrogen burning reactions. The energy released from the conversion of hydrogen into helium in the core of the star provides an outward force, called the radiation pressure, which stops the star from contracting further. The additional heat from the nuclear reactions can further increase the local temperature, increasing the reaction rate which can provide an overabundance of radiation pressure, causing the star to expand outward. The stellar hydrodynamics

continue to evolve with the star, but typically come in to equilibrium on a fairly short timescale relative to the lifetime of the star. The temperatures and densities achieved at equilibrium depend upon the initial mass and composition of the star. The hydrogen burning process can be either the process proposed by Eddington or Bethe, depending on the initial mass [41]. The core of the star will continue to burn hydrogen while there is an outer layer of hydrogen that is too cool and diffuse to ignite nuclear burning.

Once a star exhausts its hydrogen fuel, there is no longer an energy source to sustain it against gravitational attraction. It then starts to collapse, heating and growing more dense. Eventually the core temperatures and densities increase to the point at which further nuclear reactions can begin. The core of the star is now very rich in helium, since almost all of the hydrogen has been converted into helium. The helium is burned via the triple- $\alpha$  process into carbon and oxygen. This three-body process, while unlikely, is the only method for helium burning because a fusion of two helium atoms is energetically unbound. Similar to the situation with hydrogen burning, outside of the helium burning core, there is a shell of helium in which there is no burning. The ignition of helium burning provides a heat source below the dormant hydrogen shell which remained from the hydrogen burning. This allows a very thin hydrogen burning region between the helium shell and the hydrogen shell. This additional energy source causes the outer shell to expand to over 50 times the initial stellar radius.

When the helium is consumed, the star will again contract and heat. The core is now predominantly carbon and oxygen while there are shells of helium and hydrogen. Once sufficient temperatures are reached, the carbon in the core will start to burn. At this point, the star has started to resemble an onion—layer of burning nestled inside layer of burning. Outside of the carbon core is a carbon shell. On the surface

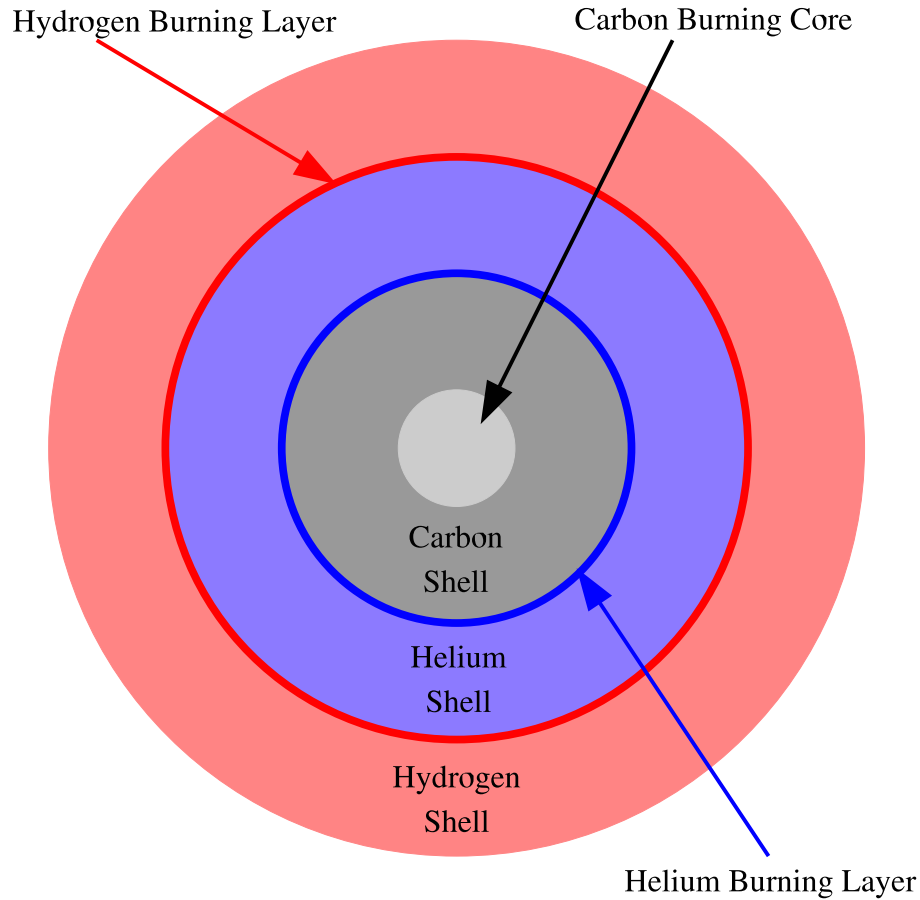


Figure 1.1. The onion-layer structure of a star with a carbon-burning core is shown. The diagram is not to scale. The shells, particularly the hydrogen burning shell, are much thicker than the inner layer and the core.

of the carbon shell is a thin helium burning layer. On top of the helium burning layer is a shell of helium. On the surface of the helium shell is a thin hydrogen burning layer. On top of the hydrogen burning layer is the final shell of hydrogen. This is illustrated in figure 1.1.

Stellar burning phases of oxygen burning, magnesium burning, and silicon burning will continue sequentially, ending with an iron core. Layers of dormant shells and thin burning zones build up for each of these layers. Most stars will not burn through all of these stages as their initial mass is not sufficient to provided the ex-

tremely high temperatures necessary for the next burning stage. It is not expected that our sun will even burn carbon in its core, but will stop after the helium burning stage. A star with insufficient mass can step out of the burning sequence at any time when its core has depleted a fuel. The star will then “die” as nuclear burning processes will cease and its core is supported against further collapse by what is called electron degeneracy, a purely quantum mechanical phenomenon. The star no longer behaves like a gas as it had previously. It is a hot, dense, but not very luminous object that will slowly cool very time and eventually disappear from view.

If the core of the star has burned into iron and nickel, no further energy can be gained by continued nuclear fusion. The mass of the star is so great ( $\geq 8 M_{sun}$ ) that the electron degeneracy pressure cannot support core. There is no further energy to support the star against gravitational collapse, leading to the cataclysmic event known as a core-collapse supernova. In a core-collapse supernova, the matter in the core of the star falls inward unchecked until it reaches nuclear densities. The material then bounces back with great velocity, smashing into the collapsing outer shells, releasing great energy and spawning nuclear reactions and ejecting much of the now processed material of the star into the cosmos. The core itself will form into a neutron star or a black hole.

The question that remains is what this cycle of the stars can tell us about the nucleosynthesis, or production, of the elements observed in the universe. Shown in figure 1.2 is the distribution of elements observed in the universe. One of the reasons that B<sup>2</sup>FH is such a critical work is because they, in a self-consistent manner, explained or predicted sources for all of the major features of the distribution.

The lightest elements, hydrogen and helium, are produced in primordial nucleosynthesis, the cooling in the immediate aftermath of the big bang. Most of that material has never been processed in a stellar core, which why there is still so much

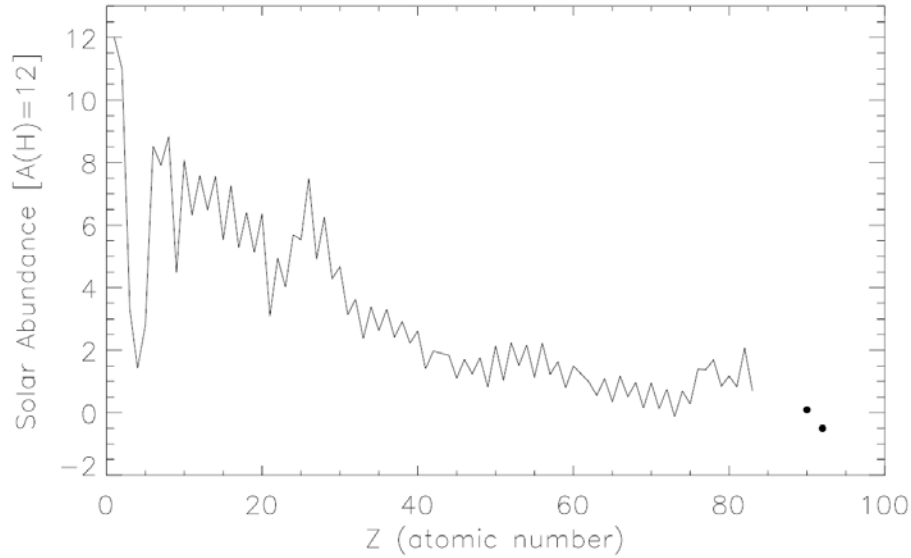


Figure 1.2. The solar system abundances are shown as a function of mass number  $A$ . The vertical axis is in somewhat idiosyncratic astronomical units. It is the logarithm of the abundance of the elements relative to the abundance of hydrogen being  $10^{12}$ . The figure is courtesy of Grevesse and Sauval [30].

today. Hydrogen burning converts the core hydrogen into helium. If the CNO cycle operates in the star, in addition to converting hydrogen into helium, most of the CNO isotopes are converted into  $^{14}\text{N}$  as that reaction limits the rate. The triple-alpha process, or core helium burning, converts helium into carbon, oxygen, and neon. The carbon, oxygen, and neon burning produce elements up to silicon. Silicon burning produces elements up to the iron region. At any stage along this sequence, a star may exit the stellar due to mass constraints. As a result, a perusal of the literature of isotopic abundances such as Anders and Grevesse or Lodders [4, 36] will show abundance peaks corresponding to a build-up at each of the appropriate departure points.

This still leaves us, however, in a universe void of gold, silver, lead, and uranium, as well as many other important, but perhaps less commonly recognized elements.

Because fusion is no longer energetically favorable, there has to be a fundamentally different mechanism for their production. That mechanism is neutron capture. Because the neutron is neutral, there is no longer the prohibitive Coulomb barrier to capture reactions. The difficulty is producing neutrons for these capture reactions. Burbidge, Burbidge, Fowler, and Hoyle postulated that the abundance distribution of heavy elements recommended two different neutron capture processes. There are peak doublets along the abundance distribution that correspond to particular nuclear structure properties of the isotopes. One of the peaks is broad while the other is very sharp. The broad peak recommended a fairly indiscriminate path of neutron capture that did not care so much about individual isotope, but only broad nuclear structure properties. The sharp peak suggests a very narrow path of synthesis which is occasionally impeded and a particular isotope was built up in abundance. The two different processes were dubbed the *r*-process, or rapid-neutron capture process, and *s*-process, or slow-neutron capture process, respectively. Each of these processes contributes about 50% of the heavy elements.

The *r*-process takes place in an environment where the neutron capture rate is so high that beta-unstable isotopes do not have the time to decay until after the entire process has ended. Captures continue all the way out until further neutron capture competes with  $\gamma$ -induced disintegration. In such unstable and hot environments, the nuclear structure effects are smeared so that once the process has ended, the isotopes which decay back to stability are distributed broadly about any reaction bottlenecks, corresponding to the broad abundance peaks in the heavy isotopes.

The astrophysical site of the *r*-process is still not conclusively known, nor even that the *r*-process is unique [18]. A preferred site is the core-collapse supernova that occurs at the end of the life of the heaviest stars when there is no further fusion to support the iron core. The bounce liberates an extremely high number

of neutrons in an extremely hot environment. The material quickly races out far beyond the valley of stability to the point at which neutron captures compete with photo-disintegrations. After the flash has ended, this material decays back to the valley of stability. This sequence produces large amounts of heavy isotopes all the way up to thorium and uranium. Because of the explosion that fueled the reactions, much of the material is expelled into the cosmos, allowing it to be condensed into new stars that are being formed.

The *s*-process takes place while the star is burning carbon and oxygen in the core. The onion-skin structure allows a separation of a helium rich zone from a hydrogen rich zone. Because the equilibrium in the shells is rather unstable, there is a regular pulsing of the shells, allowing a small amount of hydrogen to be mixed in to the helium shell. The hydrogen combines with carbon to form  $^{13}\text{C}$ . In this helium rich environment,  $^{13}\text{C}$  and  $^{22}\text{Ne}$  left from the ashes of the CNO cycle can capture alpha particles, releasing neutrons, though in much lower neutron densities than observed in the explosive environment of supernovae. If the star began with an initial composition of heavy elements, neutron capture processes can take place. Heavy elements can capture neutrons over a relatively long time scale, typically on the order of years, slowly converting into heavier and heavier isotopes. Because the time scale is so long, detailed nuclear structure effects are dominant resulting in the sharply peaked structure that is the signature of the *s*-process.

One of the most important things to note in this discussion is that the star can only produce elements heavier than helium after hydrogen burning has been exhausted in the core. For that reason, the only elements available for Bethe's catalysts in hydrogen burning are those isotopes that were present in the initial composition for the star. This has important implications for the first stars in the universe, before significant element synthesis had been completed.

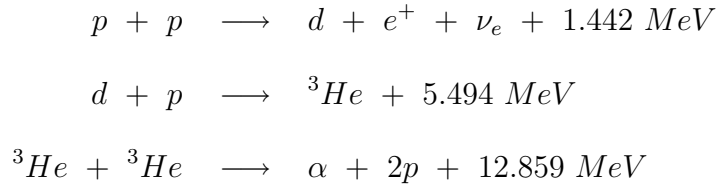
## 1.1 Stellar Burning Scenarios

The primary focus of this thesis is the measurement of a weak reaction in main-sequence hydrogen burning. To foster an understanding of the role played by the  $^{19}\text{F}(p,\gamma)^{20}\text{Ne}$  reaction, the two hydrogen cycles will be discussed in some detail, highlighting the differences between them and noting when each is expected to be dominant. In order to aid in the discussion, some basic nuclear physics terminology should be introduced. Reactions, both in the laboratory and in stars are denoted by  $A + x \longrightarrow B + y$ . In the before reaction, species  $A$  combined with species  $x$  to give species  $B$  and  $y$ . While  $A$  and  $B$  are usually nuclei,  $x$  and  $y$  can be nuclei, electrons, positrons, neutrino, gamma-rays, etc. It is also possible for there to be more than two species on either side of the reaction. When describing the same reaction done in the laboratory, if there is a target of  $A$  impinged upon by a beam of  $x$ , it will often be written  $A(x,y)B$ . Nuclei are indicated by their mass number and chemical name,  $^m\text{N}$ , where  $m$  is the mass number and  $\text{N}$  is the chemical name. The hydrogen and helium isotopes deviate from this rule, with  $^1\text{H}$ ,  $^2\text{H}$ , and  $^3\text{H}$  being denoted  $p$  (proton),  $d$  (deuteron), and  $t$  (tritium) respectively.  $^4\text{He}$  is commonly denoted  $\alpha$ . For the reaction of interest in this thesis, fluorine-19 ( $^{19}\text{F}$ ) combines with a proton to form neon-20 ( $^{20}\text{Ne}$ ), giving off a gamma-ray. This would be denoted  $^{19}\text{F} + p \longrightarrow ^{20}\text{Ne} + \gamma$ . Since a stationary  $^{19}\text{F}$  target was hit with protons, the laboratory shorthand for the reaction would be  $^{19}\text{F}(p,\gamma)^{20}\text{Ne}$ . Lower indices on the exit particles are typically used to indicate the population of a particular excited state in the residual nucleus.

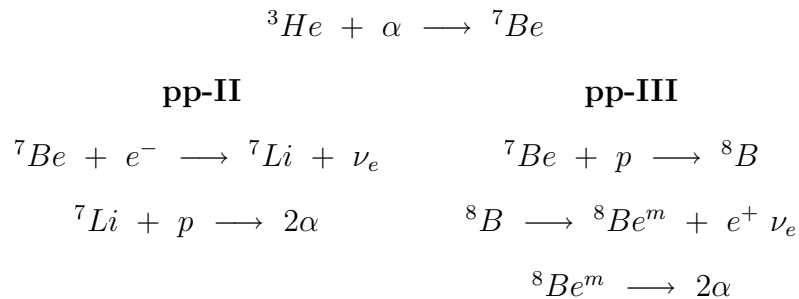
### 1.1.1 Hydrogen Burning Cycles

#### *The p-p Chains*

The first reaction sequence for burning hydrogen can be seen illustrated in figure 1.3. Starting with pure hydrogen, the reaction sequence proceeds as follows. First is a proton-proton reaction. Once sufficient deuterium accumulates, a proton capture takes place on deuterium. Finally, once there is sufficient  ${}^3\text{He}$ , the  ${}^3\text{He} + {}^3\text{He}$  reaction produces  ${}^4\text{He}$ , the net result of all of the steps being the conversion of four protons into one  $\alpha$  and 26.731 MeV of energy.



Once sufficient  ${}^3\text{He}$  and  ${}^4\text{He}$  accumulate, additional reaction channels become available. The pp-II and pp-III chains are shown as breakout in figure 1.3 and detailed below.



For all of the p-p chains, the limiting reaction is the first one, the creation of deuterium. Because it proceeds via the weak interaction, the cross-section is significantly smaller than for all of the other reactions in the sequence. This is a fortuitous situation as it provides a timescale for stellar evolution that is slow enough to make for an interesting universe. It is again worth noting that none of the above reactions produce heavy isotopes.

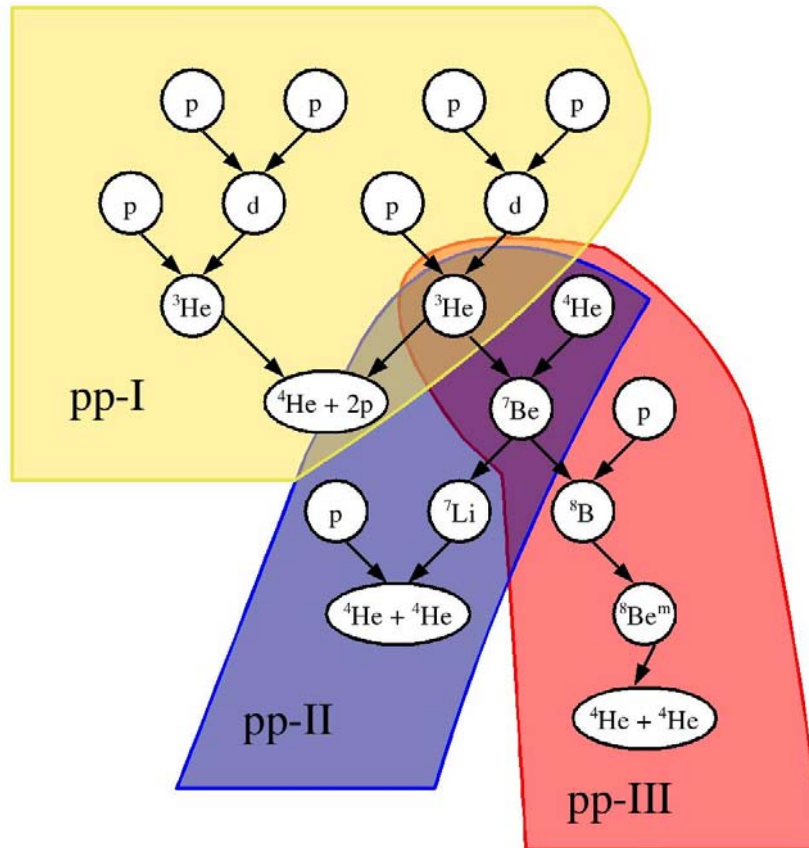
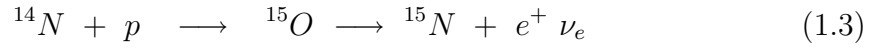


Figure 1.3. The three pp-chains are shown above. Each of the three chains convert a total of four protons into a  $^4\text{He}$  ion.

## The CNO Cycles

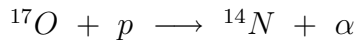
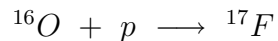
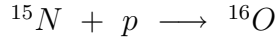
When Hans Bethe proposed the CN cycle in 1938, he proposed what is now known to be the first stage of the network, the catalytic burning of hydrogen on carbon and nitrogen as can be followed below.



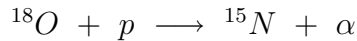
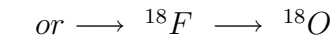
By carefully following the steps of the reaction, it can be seen that once again, four protons are converted into an  $\alpha$ . While various carbon, nitrogen, and oxygen isotopes (thus the CNO cycle) are represented, it is important to note that there is no net production of any nucleus of other than  $^4\text{He}$ . The carbon, nitrogen, and oxygen used must be present before the cycle starts and is left after the cycle ends, functioning merely as a catalyst while burning is taking place.

It was later observed that if the  $^{15}\text{N} + p$  decayed to the ground-state of  $^{16}\text{O}$  rather than emitting an  $\alpha$ , the breakout would give rise to an additional cycle. The CNO-II, -III, and -IV chains detailed below are further breakout cycles that all feed back into the original cycle, maintaining the principle that no catalytic material actually leave the cycle.

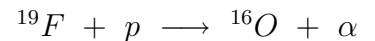
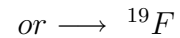
### CNO-II



### CNO-III



### CNO-IV



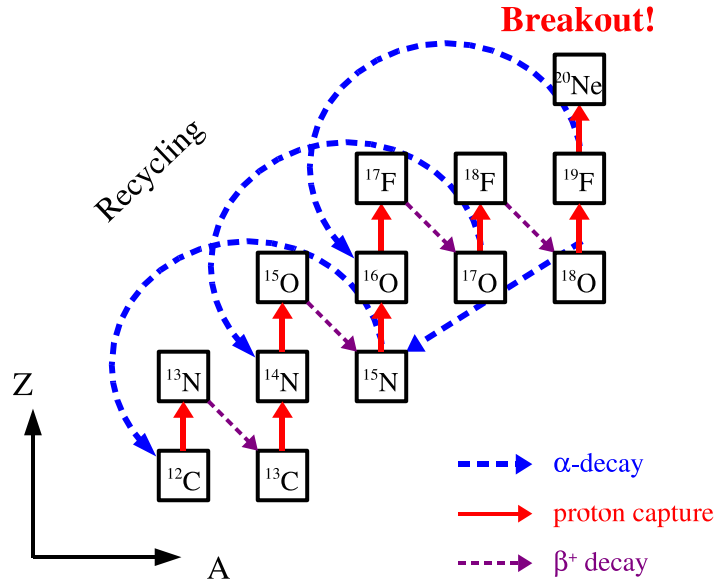


Figure 1.4. The CNO cycle for hydrogen burning is illustrated above. As one moves from left to right on the plot, the number of neutrons (N) is increasing. As one moves from bottom to top, the number of protons (Z) is increasing.

Since a significant initial abundance of the CNO materials is found as  $^{16}\text{O}$  [4], these additional burning cycles are important to correctly determine the energy generation and burning time-scale for CNO burning stars. The situation becomes more interesting should the  $^{19}\text{F}(p,\gamma)^{20}\text{Ne}$  reaction show any significant strength. As a competing reaction with the  $^{19}\text{F}(p,\alpha\gamma)^{16}\text{O}$  reaction which closes the CNO-IV cycle, breakout to  $^{20}\text{Ne}$  represents the only possible breakout from the CNO cycle at temperatures relevant for quiescent hydrogen burning [50]. Because back-processing is energetically forbidden, this breakout permanently removes catalytic material from the CNO cycles, potentially changing the energy production rate and stellar lifetime for hydrogen burning. The situation is best illustrated graphically, showing all of the cycles operating at once complete with breakout as can be seen in figure 1.4.

## 1.2 Stellar Reaction Rates

The reactions which have been discussed so far are certainly effective means to convert hydrogen into helium, no discussion was given of why they are the only players—Ne-Na and Al-Mg cycles similar to the CNO cycles can also convert hydrogen into helium. Among the hundreds of stable nuclei, there are certainly other cycles which would allow a similar conversion. There are two primary reasons that the pp-chains and the CNO cycles are the only reaction sequences that are considered. The first is the simple reason of abundances. Hydrogen, helium, carbon, nitrogen, oxygen, magnesium, and silicon are the most abundant elements in the solar system, with carbon and oxygen being by far the most abundant after hydrogen and helium [4]. For this reason, the rate of any competing process would have to be orders of magnitude larger than those for the pp chain and the CNO cycle in order to contribute significantly to stellar energy production.

The second reason involves the rates themselves. In order for any nuclear reaction to take place, the nuclei must come close enough to interact. The Coulomb repulsion between two bare nuclei is proportional to the product of the charges of the nuclei. Explicitly,

$$B_C = \frac{Z_1 Z_2 q_e^2}{R} \quad (1.5)$$

where

$$R = 1.4(A_1^{\frac{1}{3}} + A_2^{\frac{1}{3}}), \quad (1.6)$$

$q_e$  is the electron charge, and the  $A$ 's and  $Z$ 's are the mass numbers and atomic numbers of the particles. As a result the necessary energy to overcome the Coulomb barrier increases linearly with the atomic number of the target. The corresponding barriers have been calculated and can be seen in table 1.2. The temperatures in stellar interiors range from 10 to as much as 1000 MK. But this corresponds to a

TABLE 1.1

## SOLAR SYSTEM ABUNDANCES OF SELECTED ELEMENTS

Element	Abundance	Mass Fraction (%)
1 H	$2.79 \times 10^{10}$	70.683
2 He	$2.72 \times 10^9$	27.431
6 C	$1.01 \times 10^7$	0.302
7 N	$3.13 \times 10^6$	0.109
8 O	$2.38 \times 10^7$	0.948
10 Ne	$3.44 \times 10^6$	0.173
12 Mg	$1.074 \times 10^6$	0.065
14 Si	$1.00 \times 10^6$	0.070
16 S	$5.15 \times 10^5$	0.041
26 Fe	$9.00 \times 10^5$	0.125

NOTE: The abundances of the ten most abundant elements in the solar system as reported by Anders and Grevesse [4] are shown for comparison. The first columns give the elemental names and proton number. The abundance is given relative to  $\text{Si}=1.0 \times 10^6$ . Si is at least an order of magnitude more abundant than any element not listed above. The mass fraction given in the last column is based on the elemental masses of the elements. Because of the difficulty in separating spectral lines of isotopes, only elemental abundances are given.

TABLE 1.2

## COULOMB BARRIER FOR PROTON CAPTURE ON SELECTED ISOTOPES

Reaction	Coulomb Barrier (MeV)
$p + p$	0.514
$d + p$	0.455
${}^3\text{He} + {}^3\text{He}$	1.43
${}^{12}\text{C} + p$	1.88
${}^{14}\text{N} + p$	2.11
${}^{16}\text{O} + p$	2.34
${}^{28}\text{Si} + p$	3.57

Maxwell-Boltzmann energy of only hundreds of eV up to a little less than 100 keV, far less than is classically needed to overcome the Coulomb barriers seen in table 1.2. For this reason, almost all nuclear reactions in quiescent nuclear burning are allowed because of quantum mechanical tunneling effects. For energies much below the coulomb barrier, the penetrability, or probability of penetrating the Coulomb barrier, can be approximated by

$$P = \exp(-2\pi\eta) \quad (1.7)$$

where

$$\eta \equiv \frac{Z_1 Z_2 q_e^2}{\hbar v} \quad (1.8)$$

$$2\pi\eta = 31.29 Z_1 Z_2 \left(\frac{\mu}{E}\right)^{\frac{1}{2}} [41] \quad (1.9)$$

if E is expressed in keV and  $\mu$  is the reduced mass in amu. The exponential dependence of the tunneling probability provides a very strong selection criterion favoring reactions of only the smallest Z.

Between the Maxwell-Boltzmann particle energy distribution in the stellar interior and the varying barrier penetrability based on energy, in order to determine

the reaction rate per particle pair, the particle energy distribution must be folded into the cross-section over all energies, yielding

$$\langle\sigma v\rangle = \left(\frac{8}{\pi\mu}\right)^{\frac{1}{2}} \left(\frac{1}{kT}\right)^{\frac{3}{2}} \int_0^\infty \sigma(E) E \exp\left(\frac{-E}{kT}\right) dE \quad [26] \quad (1.10)$$

where  $\sigma$  is the nuclear cross-section and  $k$  is Boltzmann's constant. At this point it is convenient to rewrite the cross-section and separate the different contributions. As was discussed above, the Coulomb repulsion plays a significant role in sub-barrier reactions. A function  $S$  called the astrophysical S-factor can be defined such that

$$\sigma(E) = S(E) \frac{1}{E} \exp(-2\pi\eta). \quad (1.11)$$

Then  $S$  is solely of nuclear physics effects, the Coulomb and De Broglie terms being factored out. There are several advantages to this formalism. First, the Coulomb term is so dominant at low energies that it is difficult to see what other effects are playing a role. By separating the nuclear effects from the repulsion, it is possible to determine the source of the different contributions more easily. Furthermore, any purely nuclear effects, such as resonance structures, can be seen and treated independently.

### *Non-Resonant Reaction Rates*

Assuming that the nuclear effects are constant (i.e., the region is non-resonant),  $S(E)$  can be treated as a constant  $S_0$  and equation 1.10 can be rewritten

$$\langle\sigma v\rangle_{NR} = \left(\frac{8}{\pi\mu}\right)^{\frac{1}{2}} \left(\frac{1}{kT}\right)^{\frac{3}{2}} \int_0^\infty S(E) \frac{1}{E} \exp(-2\pi\eta) E \exp\left(-\frac{E}{kT}\right) dE \quad (1.12)$$

$$= \left(\frac{8}{\pi\mu}\right)^{\frac{1}{2}} \left(\frac{1}{kT}\right)^{\frac{3}{2}} S_0 \int_0^\infty \exp\left(-\frac{E}{kT} - 2\pi\eta\right) dE \quad (1.13)$$

$$= \left(\frac{8}{\pi\mu}\right)^{\frac{1}{2}} \left(\frac{1}{kT}\right)^{\frac{3}{2}} S_0 \int_0^\infty \exp\left(-\frac{E}{kT} - 31.29 Z_1 Z_2 \left(\frac{\mu}{E}\right)^{\frac{1}{2}}\right) dE \quad (1.14)$$

It is then trivial to differentiate the integrand with respect to energy and solve for a maximum,  $E_G = 1.22(Z_1^2 Z_2^2 \mu T_6^2)^{\frac{1}{3}}$ , the Gamow energy. Because the tails of

the two exponential components each fall so rapidly, it is only in a small region near this maximum that there will be any significant contribution to the total rate. By applying the method of steepest descent and approximating the integrand as a Gaussian, the  $1/e$  width is given approximately by

$$\Delta = \frac{4}{3^{\frac{1}{2}}}(E_0 kT)^{\frac{1}{2}} = 0.749 (Z_1^2 Z_2^2 \mu T_6^5)^{\frac{1}{6}} [keV] \quad [41]. \quad (1.15)$$

For a detailed discussion of the method of steepest descent, the reader is referred to a standard mathematical methods text such as Arfken and Weber [6]. Provided that the  $S$ -factor is constant, it then is only necessary to integrate over the region given by  $E_G$  and  $\Delta$  in order to determine the total reaction rate.  $S_0$  can be measured in a convenient non-resonant region where the coulomb barrier does not so strongly inhibit the reaction as it is assumed to be constant over all energies well below the Coulomb barrier.

This formalism is particularly useful in trying to identify the energy regions which have a significant impact on the reaction rates. It can also be used to easily look at the relative contribution from several different components.

### *Resonant Reaction Rates*

For a sharp, but narrow resonance, the cross-section  $\sigma(E)$  varies rapidly, often by several orders of magnitude over a small range in energies. If the width of the resonance is much smaller than the resonant energy, the Maxwell-Boltzmann term in equation 1.10 is basically constant over the region where the cross-section varies. Because the cross-section is so much larger over this small width where it is strong, the reaction rate will be dominated by the resonance contribution. We can then rewrite equation 1.10

$$\langle \sigma v \rangle_R = \left( \frac{8}{\pi \mu} \right)^{\frac{1}{2}} \left( \frac{1}{kT} \right)^{\frac{3}{2}} \int_0^{\infty} \sigma(E) E \exp\left(\frac{-E}{kT}\right) dE$$

$$= \left( \frac{8}{\pi\mu} \right)^{\frac{1}{2}} \left( \frac{1}{kT} \right)^{\frac{3}{2}} E_R \exp\left(\frac{-E_R}{kT}\right) \int_0^\infty \sigma(E) dE. \quad (1.16)$$

From equation 1.16, it is clear that the energy dependence of the  $\sigma$  is critical and must be accounted for properly in order to extract the reaction rate. The energy dependence of nuclear resonances follows a Breit-Wigner resonance shape [11] so that

$$\sigma(E) \propto \frac{\Gamma_a \Gamma_b}{(E - E_R)^2 + (\frac{1}{2}\Gamma)^2} \quad (1.17)$$

where  $E_R$  is the resonance energy,  $\Gamma_a$  is the partial width of the entrance channel,  $\Gamma_b$  is the partial width of the exit channel, and  $\Gamma$  is the total width of the state, defined as the sum over all possible channels.

Most generally, the Breit-Wigner cross section for a particle in—gamma-ray out reaction is given by

$$\sigma_{\alpha_1\alpha_2} = \pi \bar{\lambda}_{\alpha_1}^2 \omega \frac{1}{(E - E_0)^2 + (\frac{1}{2}\Gamma)^2} \sum_{s_1 l_1 L_2} \Gamma_{\alpha_1 s_1 l_1} \Gamma_{\alpha_2 L_2} \quad (1.18)$$

where

$$\bar{\lambda}_{\alpha_1} = \frac{M_t + m_p}{M_t} \frac{\hbar}{\sqrt{2m_p E_L}}, \quad (1.19)$$

$$\omega = \frac{(2J_1 + 1)}{(2j_1 + 1)(2J_0 + 1)}, \quad (1.20)$$

$$E_L = \frac{M_t + m_p}{M_t m_p} E, \quad (1.21)$$

and

$M_t$  is the target mass,

$m_p$  is the projectile mass,

$J_0$  is the spin of the target nucleus,

$j_1$  is the spin of the projectile,

$J_1$  is the spin of the compound state,

$J_2$  is the spin of the final state,

$\Gamma$  is the total width of the state,

$E$  is the center-of-mass energy,

$E_R$  is the resonance energy,

$\Gamma_{\alpha_1 s_1 l_1}$  is the partial width of the entrance channel,

$\Gamma_{\alpha_2 L_2}$  is the partial width of the exit channel.

The summation is over all possible spins  $s_1$ , angular momenta  $l_1$ , and gamma-ray multipolarities  $L_2$  satisfying the vector equations

$$\mathbf{s}_1 = \mathbf{j}_1 + \mathbf{J}_0 \quad (1.22)$$

$$\mathbf{J}_1 = \mathbf{s}_1 + \mathbf{l}_1 \quad (1.23)$$

$$= \mathbf{J}_2 + \mathbf{L}_2. \quad (1.24)$$

A separate term enters for each resonance and entrance—exit pair. For a particle in—particle out reaction, the second term in the summation would be replaced with  $\Gamma_{\alpha_2 L_2} \longrightarrow \Gamma_{\alpha_2 s_2 l_2}$  and the summation over gamma-ray multipolarities would be replaced by a sum over possible spins and angular momenta satisfying

$$\mathbf{s}_2 = \mathbf{j}_2 + \mathbf{J}_2 \quad (1.25)$$

$$\mathbf{J}_1 = \mathbf{s}_2 + \mathbf{l}_2, \quad (1.26)$$

with  $j_2$  the spin of the emitted particle [29].

In the case of  $^{19}\text{F} + p$ , the ground-state spins are both  $\frac{1}{2}^+$ , so the possible values of  $s_1$  are 0 and 1. Because the states being populated are known to be unnatural

parity states, ( $1^+$  and  $2^-$ ),  $s = 0$  is disallowed. We can further simplify by looking at the behaviour for different  $l$ -values. The partial width can be written as

$$\Gamma_{\alpha sl} = P_{\alpha l} \gamma_{\alpha sl}^2. \quad (1.27)$$

The reduced width  $\gamma^2$  is a purely nuclear property and can be either predicted by nuclear theory or measured experimentally. The penetrability  $P_{\alpha l}$  for a charged particle is the solution to the Coulomb wave equation and is independent of nuclear properties. Thus, the partial widths reported in the literature, should, more precisely, be reported as a partial width at an energy equal to the resonance energy. The penetrability  $P_{\alpha l}$  for a charged particle is the solution to the Coulomb wave equation and is independent of nuclear properties. It is strongly energy and angular momentum dependent. Because  $P_l \gg P_{l+1}$ , one can generally neglect all higher  $l$  terms. In this case, the entrance channel sum collapses to a single term. Finally, because the detection method integrated over all multipolarities, the exit channel sum collapses, and for  $^{19}\text{F} + p$ , there only remains a term  $\Gamma_p \Gamma_\gamma$  for each resonance.

This treatment is often sufficient for the yield near a resonance. If, however, there is interest in the contribution from a resonance at an energy  $E$  far from the resonance ( $|E - E_0| > \Gamma$ ), then the energy dependence of several terms needs to be considered explicitly. First we consider the partial widths. Recall from equation 1.27 that the partial width is equal to the penetrability times the reduced width,  $\Gamma_{\alpha sl} = P_{\alpha l} \gamma_{\alpha sl}^2$ . The reduced width  $\gamma^2$  is independent of energy. We then have

$$\Gamma_{\alpha sl}(E) \propto P_{\alpha l}(E) \quad (1.28)$$

$\implies$

$$\frac{\Gamma_{\alpha sl}(E)}{\Gamma_{\alpha sl}(E_R)} = \frac{P_{\alpha l}(E)}{P_{\alpha l}(E_R)} \quad (1.29)$$

$\implies$

$$\Gamma_{\alpha sl}(E) = \frac{P_{\alpha l}(E)}{P_{\alpha l}(E_R)} \Gamma_{\alpha sl}(E_R). \quad (1.30)$$

The penetrabilities  $P_{\alpha l}$  are calculable given the target and projectile, the energy, and the  $l$ -value.  $\Gamma_{\alpha sl}(E_R)$  is the value measured experimentally. From this, we can then calculate the partial width at any energy  $E$ .

The energy dependence of the gamma-ray partial width behaves differently. The partial width is given by

$$\Gamma_\gamma = \hbar\lambda_\gamma, \quad (1.31)$$

where  $\lambda_\gamma$  is the gamma-ray transition probability. This expression is not unique to gamma-rays, but the following transition probability is. For a gamma-ray of energy  $E_\gamma$  and angular momentum  $l$ , the transition probability is given by the approximation

$$\lambda_\gamma(E_\gamma, l) \approx \frac{8\pi(l+1)}{l[(2l+1)!!]^2} \frac{e^2}{4\pi\hbar c} \left(\frac{E_\gamma}{\hbar c}\right)^{2l+1} \left(\frac{3}{l+3}\right)^2 c(R_0 A^{\frac{1}{3}})^{2l}. \quad (1.32)$$

From this, it can be seen that for some incident energy off resonance, the correction to the gamma width will go as the ratio of the energies of the primary gamma-rays to the  $(2l+1)$  [34].

The energy dependence of the total width  $\Gamma$  could be calculated in this way as well, though it would be more computationally intensive because of the many terms that might enter. In practice, the energy dependence is negligible. Recall that the condition in which energy dependence became a concern was when  $|E - E_0| > \Gamma$ . But under this condition, the energy term in the denominator will be dominant, and any change in  $\Gamma$  will have little to no effect on the cross-section.

The final energy dependent term that should be mentioned is the resonance energy  $E_0$ . The resonance energy from equation 1.18 is not actually the experimental resonance energy, but the formal resonance energy from the matching of the internal and external parts of the wave function. This formal resonance energy has a small dependence on the energy of the incoming particle. It is defined such that at

resonance, the formal resonance energy and the experimental resonance energy are the same. The Thomas Correction (or Shift) is the difference between the formal resonance energy (which has an energy dependence) and the experimental resonance energy (which is fixed). It is calculable from the Coulomb wave functions. For the analysis in this thesis, the resonance energy was assumed to be a constant equal to the experiment resonance energy. The shift for the nuclei and energies of interest was on the order of, at most, ones of eV. Since this correction was so much smaller than the other factors in the expression, it was neglected in order to speed calculations. For a comprehensive discussion of the differences between the formal and experiment resonances energies as well as the Thomas Correction, the reader is referred to Blatt and Weisskopf’s standard text [11] as well as Thomas’s discussion of the correction [44].

### 1.3 Relating Reaction Rates to Laboratory Measurements

While it would be ideal to exactly recreate the stellar scenario in the laboratory in order to measure reaction rates, it is impractical to do so. Instead, measurements are made at specific energies. By looking at many different energies, the partial widths can be determined and then put into equation 1.10 in order to get at the rate. In the typical laboratory experiment a beam of particles at a “fixed” energy  $E_b$  is impingement upon a target of material with a thickness  $t$ , which may or may not be a pure substance. This introduces several effects which must be accounted for. First, while the beam of particles has a mean energy  $E_b$ , the particles will have some distribution of energies about  $E_b$  which can be written as  $g(E_b, E_i)dE_i$ , a probability distribution that for a mean energy  $E_b$ , a particle has energy between  $E$  and  $E + dE$ . Second, as the particles pass through the target, particles will lose energy due to scattering so that particles reacting at the back of the target will have

some energy less than  $E_b$ . This can be written as a probability  $w(E_i, E, x)dE$  that a particle incident on the target with energy  $E_i$  has energy between  $E$  and  $E + dE$  at a depth  $x$ . Quantitatively, this gives a yield

$$Y(E, t) = n \int_{x=0}^t \int_{E_1=-\infty}^{\infty} \int_{E_2=-\infty}^{\infty} g(E, E_1) w(E_2, E_1, x) \sigma(E_2) dE_1 dE_2 dx \quad (1.33)$$

where  $n$  is a number density of target atoms. For simplicity, the energy integrals are written to run over all energies since  $\sigma$ ,  $g$ , and  $w$  vanish rapidly above and below their maxima. It is further reasonable to assume that the beam distribution has a constant width, so that it only depends on  $E - E_i$  rather than on  $E$  and  $E_i$  independently.

The beam resolution can be represented by a Gaussian of the form

$$g(E_1) = \frac{1}{\zeta} \left( \frac{1}{2\pi} \right)^{1/2} e^{-\frac{(E_1-E)^2}{2\zeta^2}} \quad (1.34)$$

where  $2\zeta$  is the width of the beam resolution and  $E$  is the nominal beam energy. The integration over the target thickness can be converted into an energy integral. The straggling can be approximated by either a Gaussian or a Lorentzian distribution. A Lorentzian would give a more accurate correction due to the tailing at lower energies, but because this should be a small correction, representing it as a Gaussian should be sufficient. Then  $w$  can be written

$$w((E_2 - E_3), (E_1 - E_2)) = \frac{1}{\Delta(E_1 - E_2)} \left( \frac{1}{2\pi} \right)^{1/2} e^{-\frac{(E_2-E_3)^2}{2(\Delta(E_1-E_2))^2}}. \quad (1.35)$$

The  $E_i$  are energy integrations that should be more clear with the full yield and  $\Delta(E_1 - E_2)$  is the straggling as a function of energy loss. This allows the integration to be rewritten

$$Y(E, \xi) = \int_{E_1=E-3\zeta}^{E_1=E+3\zeta} g(E - E_1) \int_{E_2=E_1}^{E_2=E_1-\xi} \int_{E_3=E_2-3\Delta}^{E_3=E_1} w((E_2 - E_3), (E_1 - E_2)) \sigma(E_3) dE_3 dE_2 dE_1 \quad (1.36)$$

The integrations have been truncated for computational simplicity and because while straggling can decrease the energy of a particle, it cannot increase it above the incident energy. Fortunately, these corrections are expected to have a rather limited effect on the yield for the reaction being investigated.

Once the dispersion terms are accounted for, all that is left is the reaction cross-section, the same term that determines the stellar reaction rate. By fitting an experimental yield curve in this way, the signs of the interference terms in addition to the widths can be extracted, giving all of the information necessary to apply to the reaction rate analysis. While there are several further simplifications that can be made in the case of thin or thick targets, unfortunately the resonances under scrutiny vary rather widely in width, making such approximations limited in scope.

#### 1.4 Reaction Networks

Now that the concept of a reaction rate is established, the next question becomes what this means in terms of element synthesis and the evolution of the stellar composition over time. A system of differential equations can be set up to describe the evolution over time of the different species of interest. For pedagogical purposes, we will consider a simple network with two reactions,



*and*



We have four species to track.  $A$  and  $B$  are only destroyed in the network,  $D$  is only created, and  $C$  is both created and destroyed. The destruction rate of  $A$  will depend on the rate of a reaction of  $A + B$  for a single pair of particles, upon the amount of  $A$ , and the amount of  $B$ . This gives

$$\frac{d}{dt}A = -\lambda_{AB} N_A N_B$$

where  $N_A$  refers to the amount of  $A$ ,  $N_B$  is the amount of  $B$ , and  $\lambda_{AB}$  is the reaction rate for a particle pair of  $A$  and  $B$ . A similar equation can be written in the case of  $B$ . For species  $D$ , we would have

$$\frac{d}{dt}D = -\lambda_C N_C,$$

where  $\lambda_C$  is the decay rate for a single  $C$ . Finally, for  $C$ , we have

$$\frac{d}{dt}C = \lambda_{AB} N_A N_B - \lambda_C N_C,$$

Using these basic concepts, we can write a network for the CNO-cycle. The details of the network can be found in appendix B. Rather than looking at the evolution in terms of total abundance, it is typical to track molar fraction  $Y_i$ , defined as the moles of substance  $i$  per gram of total material.

Several comments should be made about the network. First, a few comments can be made about individual isotopes. Hydrogen is only destroyed in this network; since the process under consideration is a hydrogen burning mechanism, that is to be expected. Second, helium is only produced and never destroyed. At CNO-cycle temperatures, the rate for helium burning reactions is so slow that any helium consumption is negligible. Any  $\beta$ -unstable isotopes are produced in the burning cycles are always assumed to decay before any further reactions take place. This is the characteristic difference between the cold CNO-cycle and the so-called *hot* CNO-cycle. In the hot CNO-cycle, temperatures are sufficiently high that proton capture competes with  $\beta^+$ -decay. Finally, the network is assumed to stop at  $^{20}\text{Ne}$ .  $^{20}\text{Ne}$  is an important stopping point as any material processed to  $^{20}\text{Ne}$ , cannot be backprocessed to a CNO isotope via a  $(p, \alpha)$  reaction. Material lost to  $^{20}\text{Ne}$  is permanently lost to the cycle, violating one of the basic assumptions of the CNO-cycle, namely, that it is closed.

It is possible to write a network that does not make any of these sorts of assumptions. The rates for all possible processes can be entered and the network can be allowed to evolve as it will. This is often not practical as it discounts all of the knowledge about both the star and nuclear physics and instead relies on brute force to trundle through the sea of reactions. The price paid is a immense computational load. By using the basic nuclear physics to guide the creation of the network, it can be significantly simplified, allowing calculations to be done in a reasonable amount of time.

### 1.5 The Status of $^{19}\text{F} + p$

The  $^{19}\text{F} + p$  reaction is one that has a long history. Cockroft and Walton reported observing fluorine disintegrations from proton bombardment as early as 1932, the same year that they developed the first particle accelerator [17]. By 1934 Crane, Delsasso, Fowler, and Lauritsen Fowler had observed gamma-rays from the proton induced disintegration of  $^{19}\text{F}$  [19]. Given how early the first reaction studies were made, it is somewhat surprising that there is still significant uncertainty in the reaction rates. The difficulty arises primarily because the  $^{19}\text{F}(p,\alpha_2\gamma)$  reaction is so strong. The high-energy gamma-rays from the decay of the excited states of  $^{16}\text{O}$  cloud the gamma spectrum at low energies with a Compton continuum and at high energies with pile-up. The benefit has been in the determination of the spins, parities, energies, and total widths of the resonances at the energies of interest for this discussion.

The present status of the resonance information for low-energy radiative proton capture  $^{19}\text{F}$  is summarized in table 1.3. To date, no information is available on the interference effects between the various resonances. There are basically four measurements that have provided the data that has gone into these resonance width

parameters. These four measurements will be discussed, including limitations and benefits of the various techniques.

### 1.5.1 The Sinclair Measurement

The first significant measurement of the resonances of  $^{19}\text{F}(\text{p},\gamma)$  was made by Rolf Sinclair in 1953 [42]. Sinclair used a single NaI(Tl) at  $0^\circ$  to measure relative yield between the high-energy gammas and 6-8 MeV gammas. Rates were kept below 320 Hz in order to limit pile-up effects. Resonances were observed at proton energies of 669, 1092, 1324, and 1431 keV.

This early measurement recognized and accounted for one of the most severe problems facing these measurements—namely, the pile-up of the 6 MeV gamma-rays. Unfortunately, the necessity of a very low counting rate made it impossible to determine any information about the yield off resonance. Furthermore, the resolution of the NaI detector was approximately 1.5 MeV, limiting the ability to make a clean separation of the contribution from any other reactions.

Sinclair provided resonant cross-sections based on the proton widths reported by Bonner and Evans [12].

### 1.5.2 The Farney Measurement

Two years later, Farney *et al* made a series of measurements from 550-1450 keV proton energy [25]. Once again, a small, low-resolution NaI detector was used to measure the gamma radiation from the reaction. The yield was separated into a “high” energy and “low” energy regime and the contributions were correspondingly attributed to the  $(\text{p},\gamma)$  and  $(\text{p},\alpha\gamma)$  channels. They used both evaporated NaF and Ta etched with HF. Full excitation functions are shown for the energy regions studied. Pile-up effects were seen and a mathematical correction was made in an attempt to properly account for them. Farney *et al* reported resonances at 669, 874, 935, 980,

1090, 1280, 1320, 1335, 1380, and 1430 keV.

Once again, the issue of pile-up reared its ugly head, complicating the analysis and extraction of resonance parameters. While the detector only showed a resolution of about 1.1 MeV, the use of two different target types allowed a cleaner separation of contributions from  $^{19}\text{F}(p,\gamma)$  from contaminant reactions (like  $^{23}\text{Na}(p,\gamma)$ ). Unfortunately, the stoichiometry of the HF etched targets was not well known, allowing only relative measurements to the  $\alpha-\gamma$  channel. The inclusion of off-resonance data was a significant improvement, though no careful study was done of background contributions.

Only intensity ratios were reported by Farney.

### 1.5.3 The Berkes Measurement

Two measurements were made by Berkes, Keszthelyi, *et al* in 1962 and 1963 [32, 8]. A slightly larger NaI detector was used to investigate the resonances at 224, 340, 484, and 597 keV proton energy. The measurements were fairly comprehensive, looking at  $\alpha_0$ ,  $\alpha_2$ ,  $p'$ , and  $\gamma$  channels. Counting rates were kept below 300 Hz in order to minimize pile-up. An evaporated  $\text{CaF}_2$  target was used. All measurements were made on resonance in order to look specifically at the resonance parameters.

The Berkes measurement is the first measurement at significantly lower energies, starting to reach toward the region of astrophysical interest. No corrections were made for pile-up as it was determined that the low counting rate combined with a short trigger time made corrections unnecessary. The energy resolution of the detector, while significantly improved, was still quite poor by modern standards, with a resolution of only about 400 keV for 6 MeV gamma-rays. It is also worth noting that this is the only measurement that reported any strength for the 597 keV resonance, despite it being within the reach of both the Farney measurement

discussed above and the Subotić measurement which follows.

#### 1.5.4 The Subotić Measurement

The measurement of Subotić *et al* from 1979 took advantage of significant improvements in detector technology, using both NaI(Tl) detectors to measure the excitation function and a Ge(Li) detector to measure the contribution on resonance in order to cleanly determine that the de-excitations were in fact from  $^{20}\text{Ne}$ . Strengths were measured for resonances at 340, 484, 597, 669, 874, and 935 keV. Furthermore, an excitation function is given across the entire energy range. The authors attempted to avoid pile-up effects by running at very low countrates. This was coupled with the improved resolution of the Ge(Li) detector to make a clean determination of the high-energy gamma-rays.

This first measurement with a high-resolution detector exposed several shortcomings and discrepancies with previous measurements, with contributions differing by as much as a factor of 6. While the excitation function gives some information about an overall level of non-resonant contribution, the measurement was certainly not sensitive enough to observe interference effects between resonances.

Subotić reports resonance strengths which were normalized to the 669 keV resonances.

A comparison of all of the measurements can be found in table 1.3.

TABLE 1.3

PRIOR MEASUREMENTS OF RESONANCE PARAMETERS

$E_R$ (keV)	Sinclair [42]		Farney [25]		Keszthelyi and Berkes [32, 8]		Subotić [43]		Tilley [45]		
	$I_{11.2}/I_{6.13}$	$\sigma_R$ (mb)	$I_{11.2}/I_{6.13}$	$\Gamma_{\alpha_2}$	$\Gamma_p$	$\Gamma_{\gamma_1}$	$(\omega\gamma)_{\gamma_1}$	$\Gamma_{\gamma_1}$	$\Gamma_{\alpha_2}$	$\Gamma_p/\Gamma$	$\Gamma_{\gamma_1}$
224	—	—	—	1000	$\approx 0.45$	$< 0.06$	—	—	1000	—	—
340	—	—	—	—	—	0.28	0.01	0.84	2800	0.016	$0.28 \pm 0.06$
484	—	—	—	700	5	0.42	0.0026	0.62	700	—	0.42
597	—	—	—	—	—	12	0.0056	4.14	—	0.0012	12
669	1.8	0.48	$1.80 \pm 0.36$	—	—	—	—	—	—	0.98	2.2

NOTE: These are the observations previous authors have reported. If the author included a value that was taken from another work, that was not included in the table with the exception of Tilley, which is a compilation of recommended values. All resonance energies are given in the lab frame in keV. All widths are in eV.

### 1.5.5 The Present Status

The Subotić measurement and its improvements on the knowledge of the  $^{19}\text{F}(p,\gamma)$  reaction illustrate rather clearly the important effect that improvements in detector technologies can have on the reaches of experimental techniques. In the 25 years following that measurement, many advances were made, including the development of much larger volume (and correspondingly higher efficiency) high-purity germanium detectors and advances in acquisition technologies that make short time-scale coincident measurements a possibility. These combined make it possible both to re-evaluate the resonant contributions as well as make a first measurement of the as yet undetermined interference contributions which play such a significant role at astrophysical energies.

## CHAPTER 2

### EXPERIMENTAL APPARATUS AND PROCEDURE

The main body of the work was conducted in two separate experiments that were quite similar in philosophy but which utilized different equipment and detector arrays. As such, they will be discussed separately.

The primary difficulty in measuring the cross-section for the reaction of interest was a strong competing reaction that also produces  $\gamma$ -rays, the signature that was used to tag the reaction. The competing reaction,  $^{19}\text{F}(\text{p},\alpha\gamma)^{16}\text{O}$ , produces a single  $\gamma$ -ray of energy between six and eight MeV. The reaction of interest,  $^{19}\text{F}(\text{p},\gamma)^{20}\text{Ne}$ , decays either directly to the ground state or through a cascade with a minimum of 12.84 MeV of energy, the Q-value for this reaction [2], as is illustrated in the level diagram shown in figure 2.1. This difference in energy and decay multiplicity was exploited for both experiments to extract the cross-section of the proverbial “needle in the haystack.”

The first experiment described was used primarily as proof of principal. The main objective was to demonstrate that it was possible to effectively isolate the  $^{19}\text{F}(\text{p},\gamma)^{20}\text{Ne}$  reaction from the  $^{19}\text{F}(\text{p},\alpha\gamma)^{16}\text{O}$  reaction. The results of the first experiment were used to guide the design and planning of the second experiment.

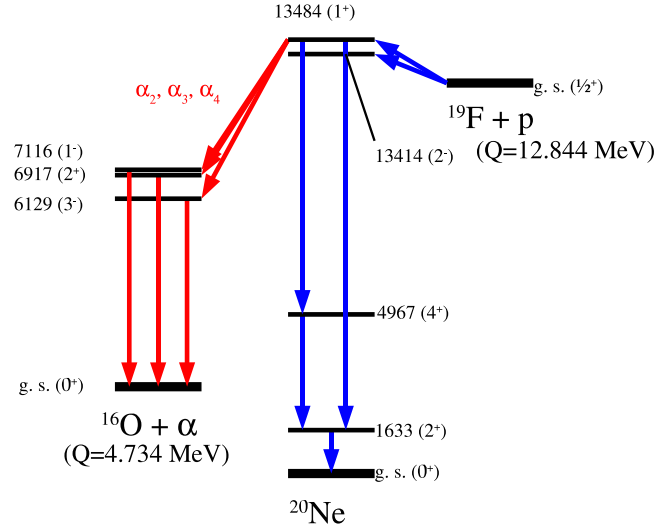


Figure 2.1. A energy level diagram of  $^{20}\text{Ne}$  as populated via the  $^{19}\text{F} + \text{p}$  reaction. Several of the possible gamma decay branches are shown in blue, including decay to the first and second excited states. To the left is shown  $^{16}\text{O} + \alpha$  together with the dominant gamma decay branchings.

## 2.1 Detector Types

Both scintillation and solid-state gamma-ray detectors were used in the experiments. These detectors have very different properties with regard to resolution and efficiency which were exploited in order to try to improved the measurements.

Barium Fluoride ( $\text{BaF}_2$ ) and Thallium-doped Sodium Iodide ( $\text{NaI}(\text{Tl})$ ) are both inorganic scintillator detectors. When a gamma-ray deposits energy in a scintillation detector, electrons are excited to the conduction or exciton bands of the material [35]. The de-excitation produces photons of a characteristic energy which are collected and converted into an electron cascade with a photomultiplier. Each compound has a distribution of wavelengths for the photons that are emitted. The reconstruction of the total gamma-ray energy is a statistical process and thus depends on, among other things, the total number of photons created, which is inversely proportional to the energy of each photon. This places a limit on the maximum resolution

which can be obtained with such a detector. When combined with the losses in resolution due to optical coupling and collection, the resolution of inorganic scintillators cannot compete with semiconductor detectors. This problem is exacerbated in BaF<sub>2</sub> crystals which have intrinsic alpha-activity due to trace amounts of radium present in the barium used to construct the crystals. On the other hand, the high density of the materials and ease of growing large crystals of inorganic scintillator make these materials ideal for high efficiency detectors.

In contrast, the germanium crystals for high-purity germanium (HPGe) detectors are very difficult to grow with sufficient purity to maintain the salient semiconductor properties, principally the small band gap. Typical impurities are better than one part in 10<sup>12</sup>, a rather stringent restriction [35]. As a result, the volume of HPGe detectors is much smaller than volumes available for inorganic scintillators. It is possible to create a detector of larger total volume by packing multiple crystals into a single housing and summing the total energy off-line. One such configuration is the “clover” detector, so named because of the four-leaf clover shape that the four crystals present. There are other significant advantages to the segmentation of the detector, but they were largely irrelevant in these experiments. The primary advantage of HPGe detectors lies in their resolution. The energy deposited in a HPGe detector excites the electrons in the germanium crystal to the conduction band. Rather than looking for photons from the de-excitations like in scintillation detectors, a bias is applied across the semiconductor so that the electrons in the conduction band are collected directly. The number of electrons collected is proportional to the total energy deposited in the detector and the energy required to excite an electron to the conduction band. The small size of the band gap results in exceptional resolution for HPGe detectors. Table 2.1 lists nominal properties of the different detectors used. A more detailed discussion of the properties and

TABLE 2.1

## DETECTOR PROPERTIES

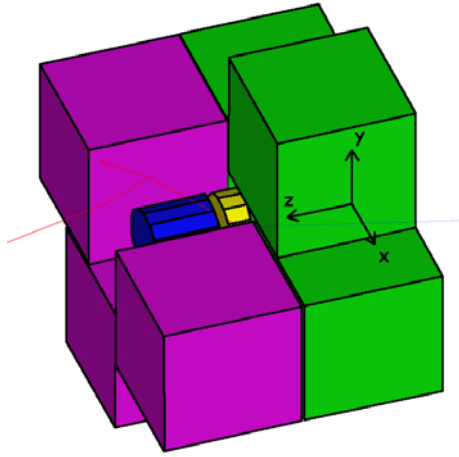
Detector	Active Volume (cm <sup>3</sup> )	Resolution at 1332 keV (keV)	Maximal Emission Wavelength (nm)	Band Gap eV
NaI(Tl)	4940	30	413	N/A
BaF <sub>2</sub>	3540	100	220/310	N/A
HPGe	354	2.4	N/A	0.785
HPGe Clover	≈700	2.4	N/A	0.785

NOTE: The active volumes and resolutions were for the detectors used in the measurements at the time of the experiments. The clover volume is the total volume for the four individual crystals. The maximal emission wavelength for NaI(Tl) is from Leo [35]. The HPGe band gaps are at 0 K and are the values reported by [35]. The maximal emission wavelength for BaF<sub>2</sub> is taken from Knoll [33]. BaF<sub>2</sub> exhibits two output components, thus the two wavelengths listed.

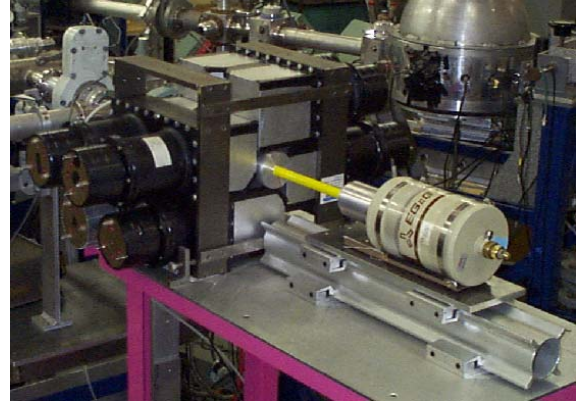
advantages of different types of gamma-ray detectors can be found in William Leo's excellent handbook *Techniques for Nuclear and Particle Physics Experiments* [35]. More detail on the use of HPGe detectors can be found in Debertin and Helmer's text *Gamma and X-ray Spectroscopy with Semiconductor Detectors* [20].

## 2.2 The BaF<sub>2</sub> Experiment

The first attempt made to measure the <sup>19</sup>F(p,γ) cross-section at Notre Dame utilized an array of BaF<sub>2</sub> detectors coupled with a single crystal HPGe in June of 2001. The goal was to detect the primary in the BaF<sub>2</sub> detectors and the secondary in the HPGe detector. This offers the advantage of high efficiency for the primaries and a clean reaction determination based on the high resolution of the HPGe detector. The KN model High Voltage Engineering accelerator was used for this first experiment.



a) GEANT Simulation of Array



b) Photo of Array as Used

Figure 2.2. On the left in panel a) is shown a visualization of the array. The HPGe detector is shown in blue while the brass target holder is shown in gold. The BaF<sub>2</sub> crystals are shown in green and purple with the purple detectors being at forward angles. One of the forward angle detectors is hidden to make it easier to see the target holder and HPGe position. The beam was incident in the positive z-direction from the right of the page. Panel b) is a photo of the array as used during the experiment.

### 2.2.1 Detector Array

In order to detect the  $\gamma$ -decay of <sup>20</sup>Ne, a detection array using eight BaF<sub>2</sub> detectors coupled with a single High-Purity Germanium (HPGe) detector was used. The BaF<sub>2</sub> detectors were each 6" x 6" x 6" cubes. The array was assembled so as to cover the largest solid angle in order to maintain the highest coincidence efficiency. A detector layout as well as a photograph of the array as used in the experiment can be seen in figure 2.2. The energy calibration of the detectors was carried out using a  $\gamma$ -ray source (<sup>60</sup>Co) as well as known decay lines in <sup>28</sup>Si from the <sup>27</sup>Al(p, $\gamma$ )<sup>28</sup>Si reaction.

### 2.2.2 Accelerator

The KN model Van de Graaff accelerator at the University of Notre Dame was used to produce a beam of protons for this stage of the experiment. The accelerator was run at voltages between 480-700 kV, below its optimized voltage range of 1.0-3.0 MV. As a result, the beam production and transmission suffered. At lowest voltages, only about 2  $\mu\text{A}$  of beam was delivered to target, effectively placing a lower limit on the range of the experiment. As much a 10  $\mu\text{A}$  of beam was available at higher energies, certainly better than the two available at lowest energies, but still a limitation for low counting rates. The accelerator was run with 141 psi of an 80/20 mix of  $\text{N}_2$  and  $\text{CO}_2$  gasses. The shorting rod was run in to limit the terminal voltage to 2.0 MV, effectively shorting out half of the column for the experiment.

A magnetic charge-to-momentum separation and beam selection technique was used to maintain a stable, mono-energetic beam on target. The initial beam from the accelerator passed through a  $17^\circ$  bending magnet. One hundred inches downstream from the magnet was a pair of horizontal slits, opened  $\pm 1$  mm. Only that beam with a given charge-to-momentum ratio given by equation 2.3 could pass through.

$$F_m = \frac{Q}{m} \vec{p} \times \vec{B} \quad (2.1)$$

$$F_c = \frac{p^2}{m\rho} \quad (2.2)$$

$\implies$

$$B\rho = \frac{p}{Q} \quad (2.3)$$

The relation between the momentum-to-charge ratio and the magnetic rigidity is given above for a beam of charged particles normal to the direction of the magnetic field.  $F_m$  is the magnetic force,  $F_c$  is the centripetal force,  $m$  is the particle mass,  $p$  is the particle momentum,  $Q$  is the charge state,  $B$  is the magnetic field and  $\rho$  is the bending radius of the magnet. Following from equation 2.3 and solving for the

energy,

$$p = \sqrt{2mE} \quad (2.4)$$

$\implies$

$$B\rho = \frac{\sqrt{2mE}}{Q} \quad (2.5)$$

$\implies$

$$B = \frac{\sqrt{2mE}}{Q\rho} \quad (2.6)$$

$$= k_p\sqrt{E} \quad (2.7)$$

where  $k_p$  is a constant dependent on the mass and charge state of the projectile as well as the bending radius of the magnet. A NMR gaussmeter was used to determine the resonant frequency directly proportional to the magnetic field, while the constant was determined experimentally for each different beam. The proton NMR constant for the KN was  $k_p = 212.72 \text{ MHz}/\sqrt{\text{MeV}}$ .

### 2.2.3 Targets and Charge Collection

The targets used were  $\text{CaF}_2$  evaporated on solid Ta backings. The backings were cut to 1.5" x 1.5" squares and were 0.010" thick. The targets were prepared first by cleaning the Ta with ethanol. Once cleaned, they were mounted in the evaporator on conducting posts. The evaporator was designed with externally exchangeable leads so that current could be sent through different paths without breaking vacuum. A 0.005" Ta boat was filled with  $\text{CaF}_2$  powder 4.4" below the target blank. The chamber was evacuated. Once down to a vacuum better than  $2 \times 10^{-6}$  torr, the Ta blank was heated by passing current through it. Once the Ta reached a dark orange glow, it was allowed to bake for five minutes to remove any organic surface contaminants. The targets were normally prepared in pairs, using a single 1.5" x 3.0" piece of Ta that was cut in half after evaporation as it was easier to heat

and allowed preparation of twice as many targets in the same time. Once the five minutes had passed, the current was turned down and the leads were transferred in order to pass current through the boat holding the  $\text{CaF}_2$  powder. The current was slowly increased on the boat until a reasonable evaporation rate was achieved. If the current was increased too rapidly, the evaporation would start too quickly, trapping a bubble under the powder which would blow the powder out of the boat when it was released. Five to ten minutes was a reasonable time for bringing up the current. The evaporation was monitored by employing a deposition monitor that was mounted near the Ta target blank and at a similar distance from the boat. It is worth noting that as long as the monitor was in a reasonable position, it was not important that it have exactly the same exposure as the target blanks since the actual target thickness was always measured with beam. The primary role of the deposition monitor was to allow reliable reproduction of targets of the same thickness. So long as its position relative to the targets was unchanged, this worked very reliably. Evaporation of  $\text{CaF}_2$  continued until a thickness of  $25 \mu\text{g}/\text{cm}^2$  was achieved. The targets were visually inspected after production to ensure that the evaporation was uniform over the surface of the target.

This thickness of Ta ( $0.010''$ ) was sufficient to completely stop the incident proton beam. The total number of protons impinging on the target was determined by collecting the charge accumulated on the target and integrating the current. Since the beam was homogeneous in charge state (+1), this current was directly converted into a number of protons. One possible difficulty is electrons scattering off of the target and drifting up the beam line, producing a current not related to the beam on target. To prevent this, the cold finger, to be discussed in more detail below, which extended to within  $0.5''$  of the target was biased to  $-300\text{V}$ , a potential that should be more than sufficient to repel any scattered electrons back to the target.

Because oil-based pumps were in use in the beamline leading up to the target station, there was concern that carbon could build up on the surface of the target during the run. To prevent this, a 8" long copper tube with a 1.25" inner diameter was connected to an liquid nitrogen (LN) dewar. The beam passed through this tube, or cold finger, just before reaching the target. As it was maintained at LN temperatures, any carbon traces moving with the beam would freeze onto the cold finger before reaching the target. There were no signs of carbon buildup seen either in the data or upon visual inspection of the target after the run.

In order to try to preserve the target integrity, the target was water-cooled throughout the experiment. Because of the geometry of the detector stand, the cooling lines had to exit along the beamline reaching the target. As a result, the target holder was slightly thicker than usual so that the cooling lines could be mounted. The target holder was made from 0.48" thick brass, with a diameter of 3.225". A reservoir was hollowed out behind the target through which to flow water. The reservoir was 1.09" in diameter and 0.39" deep, leaving only 0.10" of brass between the active target area and the HPGe detector. Finally, the beam was wobbled over the target area in X and Y to spread the beam damage over a larger area.

#### 2.2.4 Electronics

In order to try to measure the  $^{19}\text{F}(p,\gamma)^{20}\text{Ne}$  reaction, it was critical to isolate the  $(p,\gamma)$  events from the  $(p,\alpha\gamma_i)$  events. The detector array allowed this to be done by making a Q-value cut. Ideally, one would prefer to record events in list mode and write any time there was an event in any detector. Unfortunately, the event rate for the  $(p,\alpha)$  reaction was so high that this method was not feasible. As a result, some of the reduction of  $(p,\alpha\gamma)$  events had to be done in hardware before the data

was written to file. The disadvantage of this method was that the cut data was not recorded—thus, if there had been the desire to go back after the fact to try to analyze the data in another way, it would not have been possible. Much time and care was put into deciding how to construct the data trigger in a way that would both remove bad triggers and allow as much flexibility as possible post data-taking for further analysis.

The basic premise was to exploit the high efficiency of the BaF<sub>2</sub> detectors together with the high resolution of the HPGe detector. Because the <sup>19</sup>F(p,γ)<sup>20</sup>Ne reaction decays primarily through a cascade, a coincidence was required between the BaF<sub>2</sub> detectors and the HPGe. The goal was to look for the 1.63 MeV γ-ray from the transition from the first excited to the ground state in <sup>20</sup>Ne. Because of the strong background from the 6-8 MeV lines from <sup>19</sup>F(p,αγ)<sup>16</sup>O, previous authors [42, 25, 32, 8, 43] had not searched for this low energy transition, where the HPGe efficiency is highest. The construction of the trigger logic can be followed in figure 2.3. The gating of the analog-to-digital converters (ADCs) and NIM register can be followed in figure 2.4. The construction of the pulser trigger and energy signals can be seen in figure 2.5. A listing of all of the electronics abbreviations can be found in table A.1.

A constant fraction discriminator (CFD) was set on the BaF<sub>2</sub> detectors as well as the HPGe. The threshold for the BaF<sub>2</sub> detectors was at about 500 keV while the threshold for the HPGe was about 70 keV. The threshold for the BaF<sub>2</sub> detectors had to be set so high because of the intrinsic background in the BaF<sub>2</sub> detectors combined with the high countrates. A coincidence between any BaF<sub>2</sub> crystal and the HPGe would trigger an event. In addition to the recording of the signals in ADCs, the timing portion of the signal was fed into a NIM register. The register was gated with a 65 ns gate. Any signal from the CFD within that window would set a detector

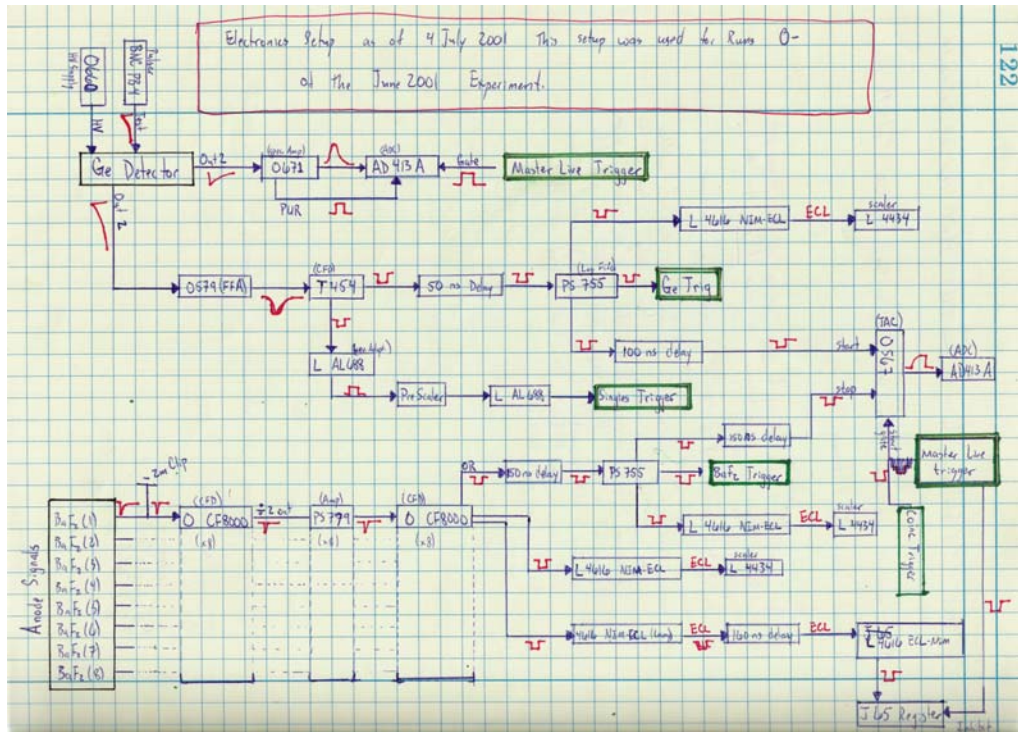


Figure 2.3. The electronics schematics for the BaF<sub>2</sub> experiment are illustrated above as recorded after the experiment. The processing of the timing signals and trigger generation is illustrated above.

by detector bit to true so that afterward it was possible to determine exactly which detectors had participated in the coincidence and only use those energy signals in the event reconstruction. Without the NIM register, a random event that was outside the 65 ns coincidence window but which arrived within the 2  $\mu$ s ADC gate could distort the energy reconstruction.

Next, a prescaler used on the output of the HPGe CFD signal. The output of the prescaler was OR'ed into the master trigger. This allowed a sampling of the singles spectrum from the HPGe. The prescaler could be adjusted for prescaling of 1, 2, 4, 8, 10, 20, 40, and 80. Any time a prescaler event was the source of a trigger, a prescaler bit was set to true in the NIM register so that the prescaled spectra could be disentangled from the coincident spectra offline. Effectively, this



allowed a pure singles spectrum to be taken to watch the  $^{19}\text{F}(\text{p},\alpha\gamma)^{16}\text{O}$  channel as the measurements were in progress. Since  $^{19}\text{F}(\text{p},\alpha\gamma)^{16}\text{O}$  has been better studied than  $^{19}\text{F}(\text{p},\gamma)^{20}\text{Ne}$ , it served as a useful diagnostic to ensure that what there was good understanding of the measurement underway.

Finally, a pulser signal was shaped to resemble a HPGe pulse and fed into the test input of the HPGe. The height was set to correspond to energy outside the range of experimental interest to prevent confusion in the later analysis. This signal produced an output both from the CFD and the shaping amplifier. There was not, however, a test input on the  $\text{BaF}_2$  detectors, so there would be no coincidence. Therefore, the logic output of the pulser was used to generate a trigger signal which was OR'ed with the master trigger. A pulser bit was set to true in the NIM register so that pulser signals could be separated from real events offline. By comparing the number of pulser events triggered to the number seen in the pulser spectrum from the HPGe, a deadtime measurement could be made. This was used to confirm the charge deadtime measurements made in real time.

This method significantly reduced the number of  $^{19}\text{F}(\text{p},\alpha\gamma)^{16}\text{O}$  events since it required multiplicity two. This does exclude any ground state transitions from being observed. They were not expected to contribute significantly to the reaction rate. Using this method, it was possible to maintain reasonable acquisition rates ( $\sim 2\text{kHz}$ ) with relatively high rates in the HPGe ( $\sim 15\text{kHz}$ ). The rates in the individual  $\text{BaF}_2$  detectors were in excess of  $50\text{kHz}$ . An acquisition rate of  $2\text{kHz}$  corresponded to 20% deadtime due to acquisition, the maximum deadtime that the system was allowed.

Because of the coincidence requirement, it was necessary to determine the coincidence efficiency. The  $^{27}\text{Al}(\text{p},\gamma)^{28}\text{Si}$  reaction was used to calibrate the efficiency. The level structure of  $^{28}\text{Si}$  is both well studied and similar to that of  $^{20}\text{Ne}$ . This makes it an ideal candidate for studying the systematics of the setup. The  $E_p=992\text{keV}$

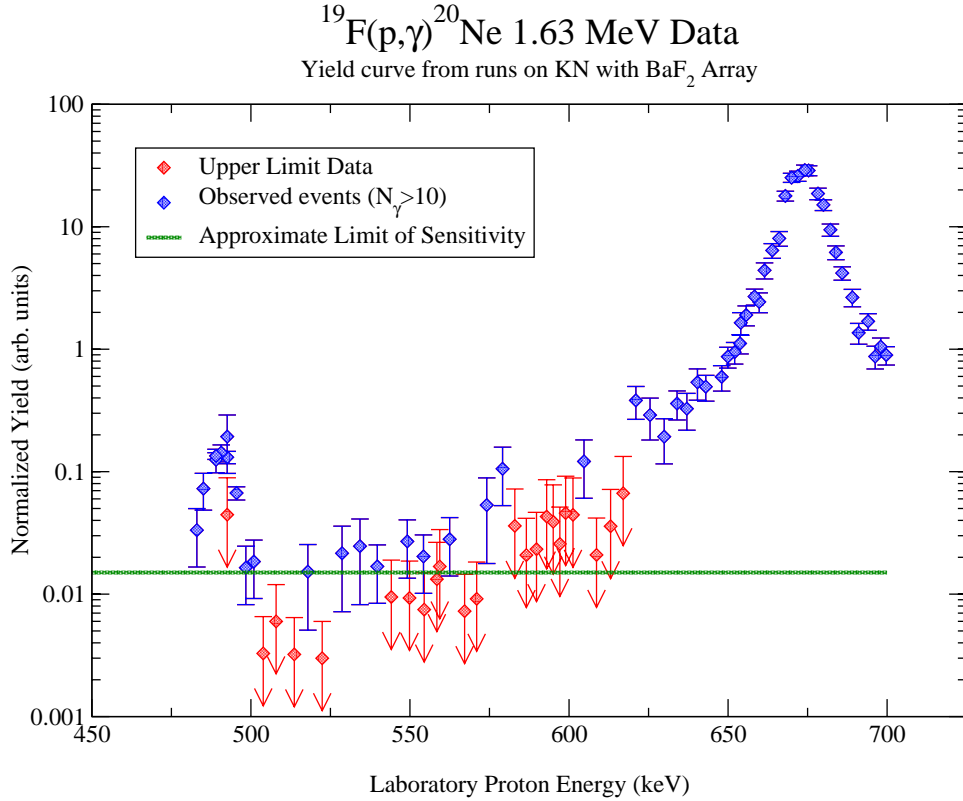


Figure 2.6. The yield curve from the experiment on the KN accelerator with the BaF<sub>2</sub> detector array is shown above. The yield is based on 1.63 MeV gamma-rays observed in the HPGe detector in coincidence with a total energy condition in the BaF<sub>2</sub> detectors. As can be seen, the sensitivity of the method is limited and had to be improved before more detailed studies could be done.

and 633 keV resonances were used in order to determine the detection efficiency. A detailed discussion of the efficiency determination will be given in section 3.1.3.

A yield curve showing the results of the initial experiment with the BaF<sub>2</sub> array can be seen in figure 2.6. It is worth noting that while it was possible to extract the (p, $\gamma$ ) channel, there are regions where greater statistics were needed. Furthermore, a rather narrow energy range was covered in this initial experiment.

### 2.3 The NaI(Tl) Experiment

Based on the analysis of the BaF<sub>2</sub> experiment, there were several objectives for further experimentation in order to make a significant impact on the present status of the data concerning the  $^{19}\text{F}(\text{p},\gamma)^{20}\text{Ne}$  data and reaction rates. First, from the previous measurements, it was clear that the basic concept behind the technique, utilizing high-efficiency inorganic scintillators coupled with high resolution HPGe detectors to identify the individual transition as part of a total cascade, was valid. It was also seen that the sensitivity needed to be improved by at least one order of magnitude, preferably two, if the inter-resonance region was going to be observed. Finally, it was necessary to reach to lower energies to probe the most sensitive regions and make further measurements on lower energy resonances.

These requirements were tackled by making significant improvements both from the point of view of the accelerator and the detector array. A significant technical hurdle that had to be overcome before starting the second phase of the experiment was the installation of a JN model Van de Graaff accelerator, previously located at the University of Toronto, which was brought to Notre Dame and brought on-line to provide higher intensity and lower energy beams than had been available with the KN accelerator used before. The opportunity was taken to reconstruct almost every subsystem on the accelerator, originally manufactured in the 1960's. The single crystal HPGe detector was replaced with a four element clover HPGe detector that had a significantly larger active volume, increasing the solid angle and detection efficiency of the high-resolution half of the detection scheme. Finally, the BaF<sub>2</sub> detectors were replaced with NaI(Tl) detectors. The efficiency of the NaI(Tl) detectors was less than that of the BaF<sub>2</sub> detectors, however, they exhibited significantly better resolution than the BaF<sub>2</sub> detectors and the array geometry decreased cross-talk between the detectors.

### 2.3.1 The JN Van de Graaff Accelerator

In order to extend to the lower energies needed for the second experiment, the JN model accelerator previously at the University of Toronto was brought to Notre Dame and reinstalled for nuclear astrophysics experiments. As part of the reinstallation, a major overhaul of the accelerator was made. An entire new beamline plan, shown schematically in figure 2.7, was developed as the space constraints at Notre Dame were significantly different than those at the University of Toronto. Furthermore, the JN had to feed in to the same switching magnet as that used for the KN accelerator so that beam could be delivered to the same beam lines. While the space constraints were relatively stringent, there was some flexibility in the final position of several of the optical elements, so beam optics calculations were made using the OPTIC-II beam simulation package in order to determine the optimum position of several elements, including a quadrupole doublet focusing magnet before the analyzing magnet. The use of a quadrupole prior to the analyzing magnet can present difficulties in beam tuning, but due to the divergence of the beam exiting the acceleration tube, it was mandatory to include the additional magnet in designing the beam line.

The analyzing magnet which came with the JN was a reused magnet originally designed for a different accelerator. The magnet box was poorly designed such that it was difficult to align. Furthermore, it was not fixed to the pole faces, meaning that even if the magnet box was aligned, there was no guarantee that the magnetic field was in the proper place. A new analyzing magnet was designed and built by Sigma Phi. Its specifications were for use with the JN accelerator. Most importantly, it was designed with an integrated magnet box, so that the pole faces actually form part of the vacuum chamber. This allowed pinholes to be placed in the lower magnet pole. By placing pins of the appropriate height in the holes, the actual pole faces could

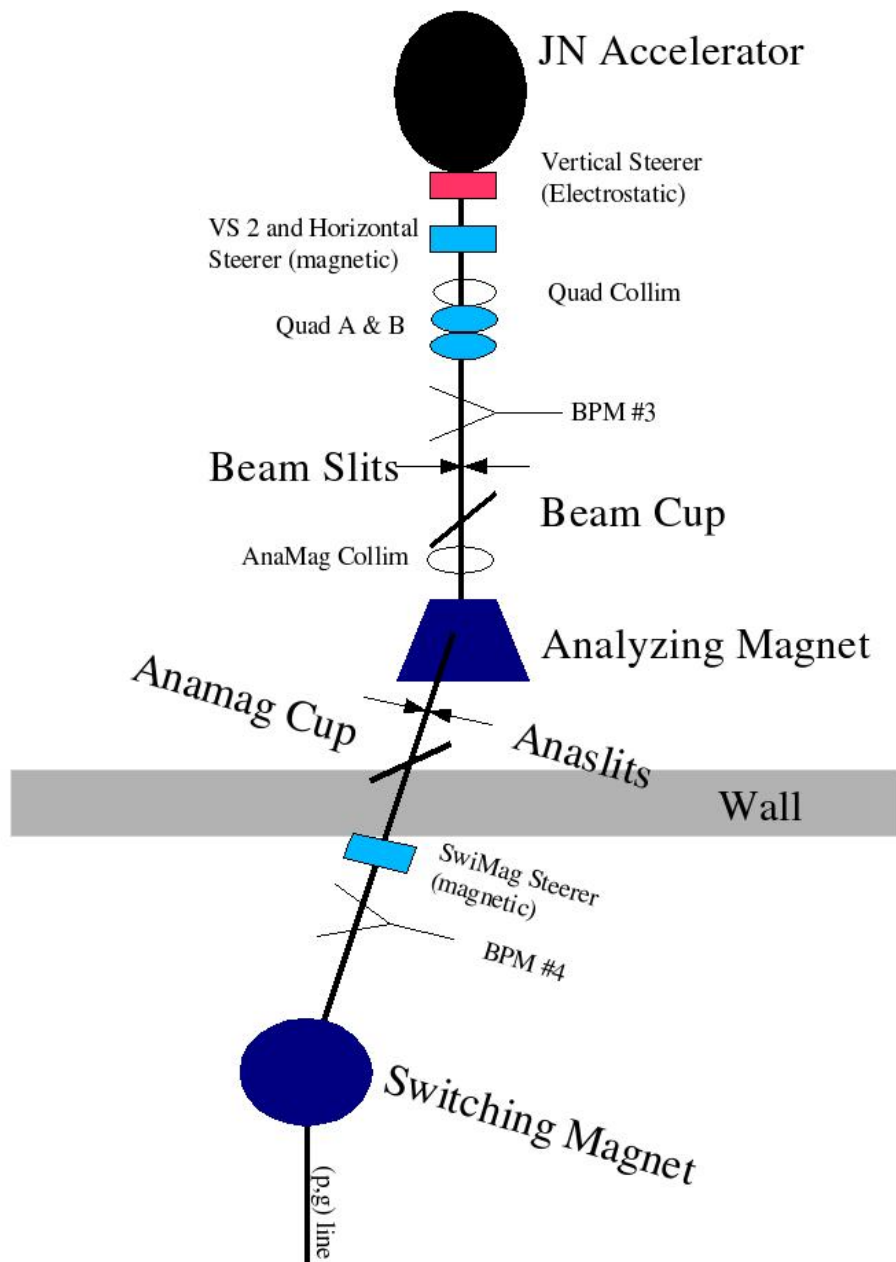


Figure 2.7. The optical elements and basic floor plan of the JN installation at Notre Dame are shown above. The drawing is not to scale.

be precisely aligned, a significant improvement over the previous analyzing magnet. The new analyzing magnet was purchased together with a matched supply capable of providing 10 ppm long term (over eight hours) current stability and better than 5 ppm short-term stability to make possible very stable field conditions.

The original vacuum pumps were mercury vapor diffusion pumps. While the pumping speed of diffusion pumps is hard to match, oil-based pumps pollute the beam with carbon. The health hazards of mercury have made it a difficult substance to work with because of the necessary precautions that must always be taken in its handling. For this reason, the vacuum pumps were replaced with turbo-mechanical pumps. Vacuum interlock systems were designed and built to both protect the pump and the beamline in the event of a vacuum accident.

The terminal was entirely rewired as the insulation was suspect in many places on the terminal. The accelerator allowed the production of both hydrogen and helium beams. A thermo-mechanical leak was used for the production of helium beams while a palladium leak was used for hydrogen beams. The acceleration tube was replaced with a rebuilt tube as the original tube had warped due to excessive heat in its previous incarnation. A Glassman 70 W, 35 kV, 2mA solid-state charging supply with <0.1% voltage stability replaced the previous system, allowing better control and monitoring of the charge delivered to terminal. The quadrupole power supplies were replaced with Hewlett-Packard 6653A power supplies. One of the significant advantages of the upgrade in the supplies across the board is that it allowed the implementation of computer control of the accelerator and optical systems.

Group 3 fiber optic control hardware was used to interface the entire acceleration system to a Labview computer control system, significantly simplifying the user control of the accelerator. Group 3 hardware offers the advantage of electrically isolating the accelerator hardware from the computer control system, an important

consideration for high-voltage systems. The implementation of a computer control system for the accelerator presented a significant technical challenge as no accelerator control via Labview had been done at the Nuclear Structure Laboratory prior to this installation. This required a redesign of the drive for the ion source control rods. The original installation used selsyn motors to adjust the control rods. Selsyn motors have the advantage of giving tactile feedback to the operator. This was not a reasonable design for a computer control system as it required a sense of touch to operate. Instead, stepper motors were used as the position could then be determined by a total number of steps that had been taken. Limit collars were designed to sense upper and lower limits on the travel in case zero was lost. Finally, additional isolation was provided so that an accelerator spark did not harm any of the distributed control modules. Furthermore, the Group 3 hardware did not offer the option of current measurement, only voltage sensing. All of the beam currents on the slits were converted to logarithmic voltage signals before they were read by the Group 3 Hardware. The use of the logarithmic amplifiers allowed beam current sensitivity over eight orders of magnitude.

Once the hardware was in place, it was still necessary to design and write the software interface. It was visually broken into three basic pieces— beam production (or ion source control), acceleration and optics, and output monitoring. The interface for each of these can be seen in figures 2.8, 2.9, and 2.10 respectively.

The one system which was not converted to computer control was the energy stabilizer. Instead, energy stabilization was controlled with an analog slit feedback system like the one described in section 2.2.2. The analyzing slits on the JN were 96" downstream of the analyzing magnet and set to counter settings of  $\pm 100$  from the zero. This corresponded to approximately  $\pm 1$ mm. Because the slits operated differently than the KN slits, it was not possible to get exact distances, only exact

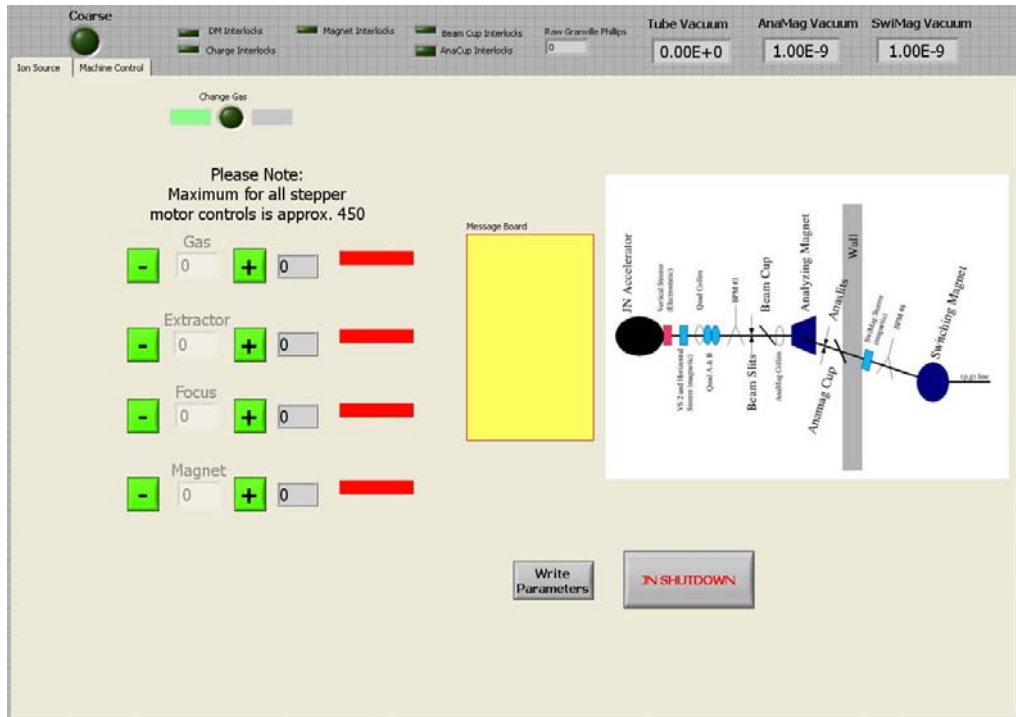


Figure 2.8. The ion source Labview control interface is shown above. Beam selection as well as control of the stepper motors for ion source controls in the terminal could be made via this interface.

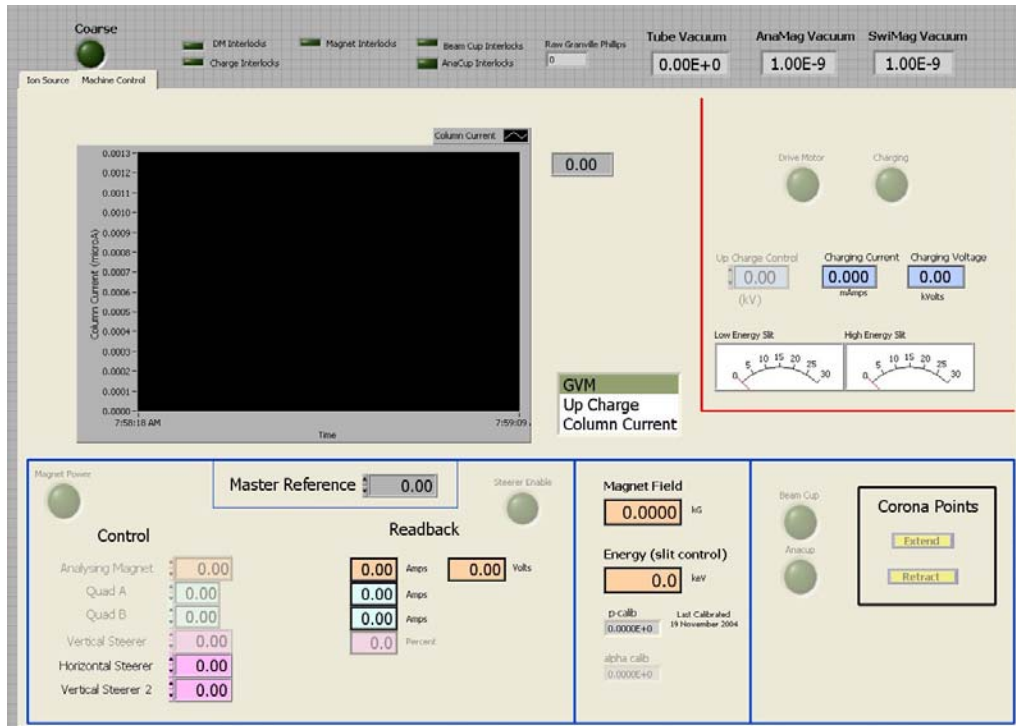


Figure 2.9. The voltage control of the accelerator as well as the focusing and steering of the beam is controlled via this interface. It is part of a shared panel with the ion source control, so that only one of them could be viewed at a given time. Several of the controls were interlocked such that they could only be activated when the belt was running.

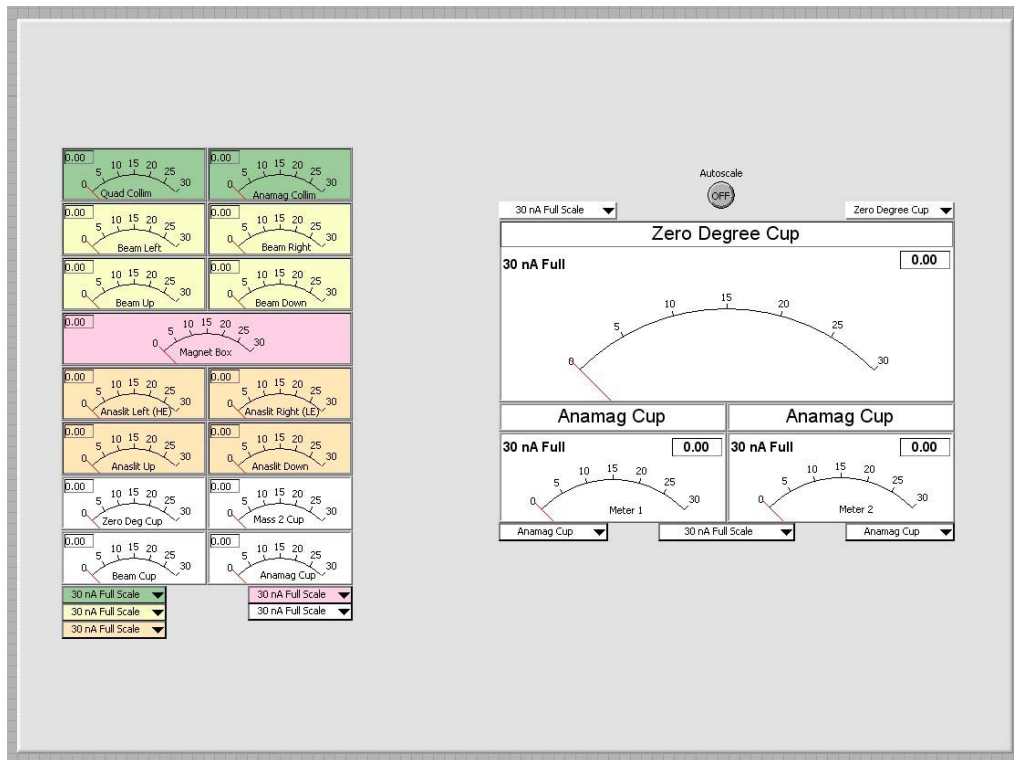


Figure 2.10. The beam seen by the various slits and apertures on the beamline could be monitored via this interface. All of the currents were converted back into a current value in software. An autoscaling feature was designed to make the interface more user friendly.

counter values. The JN accelerator was operated with 162 psig of tank gas, an 80/20 mix of N<sub>2</sub> and CO<sub>2</sub>. A Hall probe was used instead of the NMR system used for the KN. The Lakeshore 420 hall probe was outfitted with a transverse field probe. A housing was made so that the probe was fixed in position and rotation so as provide reliable readout. It had sensitivity ranges appropriate to the fields needed both for protons and alphas, the two planned beams for the JN accelerator.

The ion source bottle used during the experiment had an aluminum exit canal. While aluminum canals are known to degrade rapidly when running alpha beams, no significant loss of performance was seen from the ion source during the experiment.

The JN accelerator produced analyzed beams of up to 40  $\mu\text{A}$  of protons, though typically only  $\sim 20$   $\mu\text{A}$  were used in order to preserve the life of the targets. This already was an increase in beam of an order of magnitude from the KN accelerator at these energies. The region from 210 keV up to 700 keV was mapped with the JN accelerator. The KN accelerator was used to map energies from 650 keV up to 800 keV because the JN was unstable at energies above 700 keV during its first runs. Because the accelerators pass beams through the same switching magnet, the target and detector setup was unchanged, regardless of which accelerator was being used to produce beam. The 669 keV resonance in the region of overlap made sure that the yield curves could be smoothly matched. Typical running parameters for the JN accelerator during the experiment are listed in Appendix E

### *Energy Calibration and Reproducibility*

Because this was the first experiment conducted on the newly installed accelerator, it was particularly important to calibrate the beam energy to the magnetic field. The same well-studied  $^{27}\text{Al}(p,\gamma)^{28}\text{Si}$  reaction was used. Very sharp resonances at  $E_p = 632.23$  keV, 504.90 keV, and 405.5 keV have unique  $\gamma$  signatures [24] which were

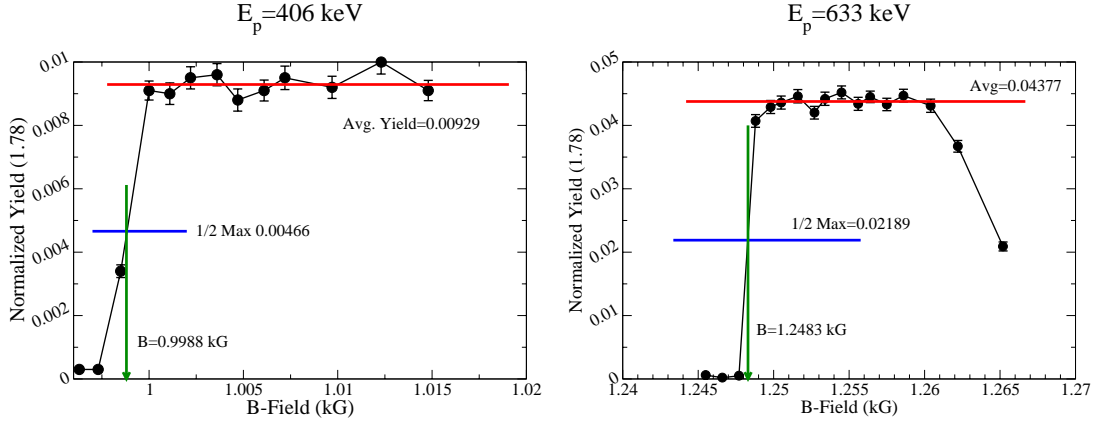


Figure 2.11. The energy calibration of the JN accelerator was determined by the extraction of the field corresponding to the 50% maximum yield. Two of the calibration points are shown above.

observed with a single crystal HPGe. By using a thick Al target, the resonance could be scanned from an energy above the resonance energy to below it. The half-point of the yield curve is the resonance energy. Fitting the field values to the literature values for the resonance energies with the relation from equation 2.7 allowed the extraction of a Hall probe constant for energy determinations. Figure 2.11 demonstrate the extraction of the fit points The calibration constant determined for the JN was  $4.96 \times 10^{-2} \text{ kG}/\sqrt{\text{MeV}}$ .

Magnetic hysteresis is a well-known phenomenon. While in principle, a known field should determine the bending of particles passing through the analyzing magnet, because the field measurement is only taken at one point and different regions of the magnet may well exhibit different hysteresis effects, it was necessary to establish a consistent procedure for changing the field of the magnet to ensure that the same hysteresis curve was followed, corresponding to passing the same energy particles through the entire magnet. As a result, it was important that the magnet be brought into the same state for each energy. The detailed system for doing this

can be found in Appendix C.

The same procedure was followed throughout the experiment. Effectively, the current was turned down to 0 for five minutes, and then increased to produce a field that would be appropriate for protons of approximately 1100 keV of energy, far above the region of interest. As a cross-check that the procedure was effective in reproducing the same energy, two resonances were scanned by three different operators. If the energy were dependent on different tuning procedures, it was expected that by having different operators and different energies, this effect would be seen. The results of the scans can be seen in figure 2.12. An implanted  $^{19}\text{F}$  target was used for these tests due to the very high stability of the F implanted in an Fe backing. A detailed discussion of the stability of implanted F targets can be found in the work of C. Ugalde [49]. As can be seen, the yield curves differ by less than 0.2 keV, at the front-edge 50% point, indicating that the procedure is a rather robust method of reliably returning the same energy.

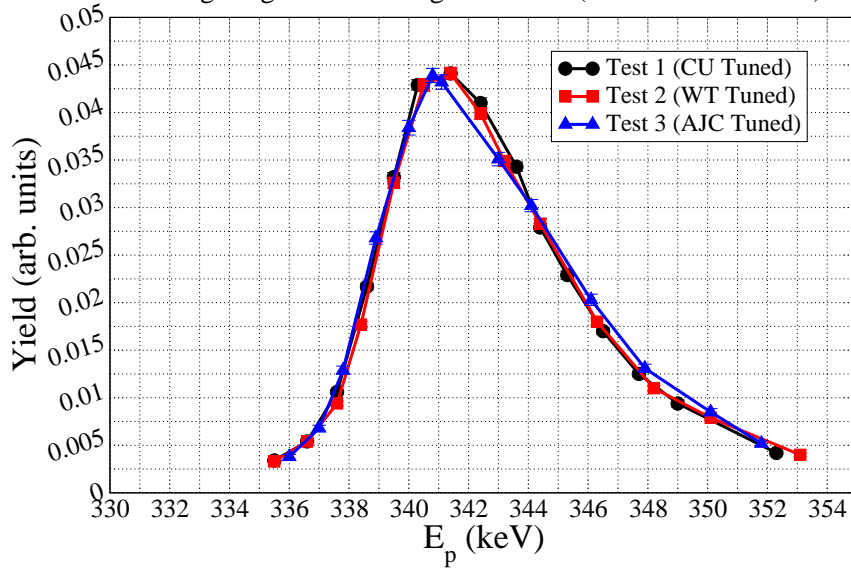
### 2.3.2 Detector Array

As was mentioned in the introduction to this section, conceptually, the detector array for this part of the experiment was quite similar to the detection scheme discussed above. Rather than  $\text{BaF}_2$  detectors, Tl doped NaI ( $\text{NaI}(\text{Tl})$ ) detectors were used. The single crystal HPGe was replaced with a four-element clover HPGe. Each element had a smaller active volume than the 55% HPGe, but the total active volume was much larger, boosting the relative efficiency to 155%.

#### *NaI(Tl) Detectors*

Four cylindrical  $\text{NaI}(\text{Tl})$  detectors were used at backward angles. The detectors were each 8" diameter x 6" deep crystals. They were mounted such that both the azimuthal and polar angles of the symmetry axis were  $45^\circ$  off of the beam axis,

Map of 340 keV Resonance, Implanted Target #205  
Using Magnet Refreshing Procedure (before recalibration)



Map of 484 keV Resonance, Implanted Target #205  
Using New Magnet Refresh Procedure (before recalibration)

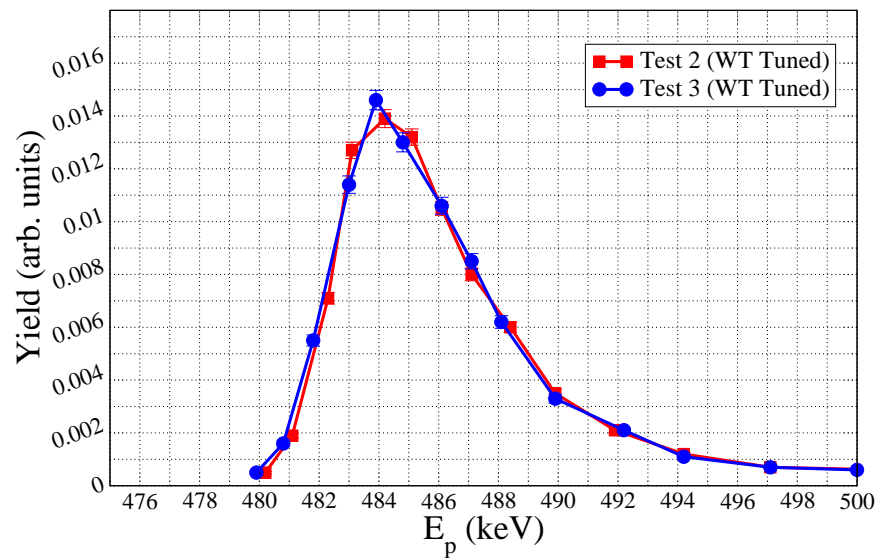


Figure 2.12. The energy reproducibility of the JN accelerator is demonstrated with two different  $^{19}\text{F}(p,\alpha\gamma)$  resonances. Three different operators tuned the beam and ran the excitation functions for these scans.

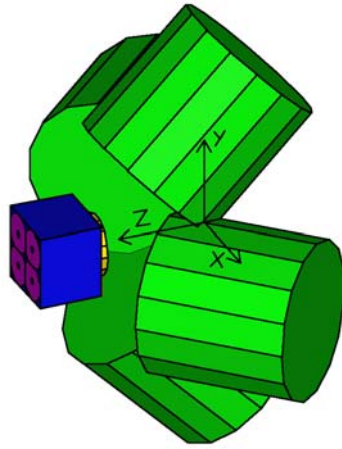
and arranged in such a way that each detector pointed inward toward the target. In order to optimize the solid angle coverage, the detectors were offset so that a perpendicular line from the detector face to the center of the target was 1.5" off of the central axis of the detector. This allowed the crystals to move 1.0" closer to the target, improving the solid angle coverage significantly. Finally, the entire array was positioned so that the viewing center of the four detectors converged 1.0" downstream of the target position. This setup was determined to give the maximum efficiency in a series of tests with a  $^{60}\text{Co}$  ( $E_\gamma=1173.2, 1332.5$  keV) source. A drawing of the setup can be seen in figure 2.13. The NaI(Tl) detectors covered  $\sim 30\%$  of  $4\pi$ .

The energy calibration of the NaI(Tl) detectors was carried out using gamma radiation from a  $^{60}\text{Co}$  source ( $E_\gamma=1173.2, 1332.5$  keV), the photopeak and single escape lines from the decay from the second excited state of  $^{16}\text{O}$  populated from  $^{19}\text{F}(p,\alpha\gamma)^{16}\text{O}$  ( $E_\gamma=6129.89, 5618.89$  keV) [1], and the decay lines from the the 12.194 MeV excited state of  $^{28}\text{Si}$  populated from the  $^{27}\text{Al}(p,\gamma)^{28}\text{Si}$  reaction at  $E_p=632$  keV ( $E_\gamma=10405.21, 9894.209, 7568.95, \text{ and } 1779.030$  keV) [24]. A linear fit to the the gamma-ray energies was sufficient.

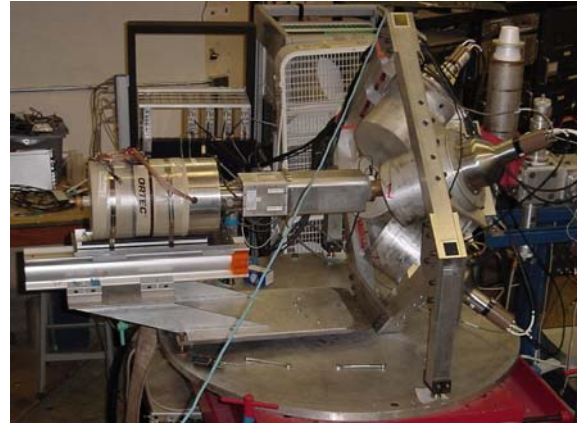
#### *HPGe Clover Detector*

A 155% HPGe clover detector was mounted at zero degrees with the central axis of the detector anti-parallel to the beam axis. The detector was designed with a 1.5 mm Al endcap; there was 5 mm of vacuum between the back of the endcap and the front face of the Ge crystals. A thin (0.010") sheet of Teflon was placed between the detector and the target holder in order to maintain the electrical isolation of the detector from the beam line. The total distance from the target to the front face of the Ge crystals was 19.2 mm. The clover detector covered 40% of  $4\pi$ .

The energy calibration of the Ge crystals was carried out using the same  $^{60}\text{Co}$



a) GEANT Simulation of Array



b) Photo of Array as Used

Figure 2.13. On the left in panel a) is shown a visualization of the array. The clover detector is shown in blue with purple crystals while the brass target holder is shown in gold. The NaI(Tl) crystals are shown in green. The rotation of the NaI(Tl) crystals allowed a better solid angle coverage. The beam was incident in the positive z-direction from the right of the page. Panel b) is a photo of the array as used during the experiment.

source,  $^{40}\text{K}$  ( $E_\gamma=1460.9$  keV), the photopeak, single-, and double-escape lines from the decay from the second excited state of  $^{16}\text{O}$  ( $E_\gamma=6129.98$ ,  $5618.89$ , and  $5107.89$  keV) and the decay of the first excited state of  $^{28}\text{Si}$  ( $E_\gamma=1779.030$  keV). The decays of the higher excited states of  $^{28}\text{Si}$  were not used because the detector resolution was sharp enough to make the doppler corrections to their energies significant. Because of the geometry, such corrections were sufficiently uncertain to warrant the exclusion of these data in the energy calibration.

### *Coincidence Efficiency*

The total efficiency of the array running in the detection mode that was being used was a critical factor since the goal was to measure an absolute cross-section. In order to determine both what the absolute efficiency of the setup as well as the coincidence efficiency was, several techniques were employed. First, a weak  $^{60}\text{Co}$

source was mounted in the target position. Because  $^{60}\text{Co}$  exhibits a two gamma cascade, it is an excellent choice for determining the coincidence of a setup. The activity of the source was known, so it was an elementary matter to determine the number of  $\gamma$ -rays emitted and compare it to the number seen.

The second method exploited the strength of one of the resonances in  $^{19}\text{F}(p,\gamma)$ , allowing the first excited state transition to be seen on top of the Compton background from the 6.13 MeV lines even in single mode. By comparing the losses by requiring the coincidence, the coincidence efficiency could be determined directly. The entire setup was then modeled using the GEANT3 simulation package [15]. Once the absolute calibration by the experimental study, the GEANT simulation was used to correct for the slight difference in  $\gamma$ -ray energies. A detailed discussion of the effect of the cut-energy on the efficiency will be given in section 3.1.3

### 2.3.3 Electronics

As was mentioned in the beginning of the discussion of the NaI(Tl) experiment, the basic concept behind the detection scheme and trigger logic from the first experiment was quite successful. For this reason, the electronics were very similar in the two experiments. The place of the eight  $\text{BaF}_2$  detectors was taken by the four NaI(Tl) detectors. The single crystal HPGe was replaced by a four element clover HPGe. The master trigger was again constructed by requiring a coincidence between any NaI(Tl) detector and any element of the clover. The OR'ed output from the four crystals in the clover was sent to a prescaler to allow simultaneous acquisition of singles spectra. The NIM register was once again used in order to reconstruct events from only those detectors which actually participated in the coincidence and to remove prescaled events from the coincidence spectra. The construction of the individual triggers can be followed in figure 2.14 while the construction of the master

trigger is shown in figure 2.15. The gating of the energy signals is shown in figure 2.16. Again, all electronics abbreviations can be found in table A.1.

There were several improvements to the electronics from the previous experiment. First, the NaI(Tl) energy signals were converted by an ORTEC 413A ADC, which had a much faster conversion and readout time than the ADC used for the BaF<sub>2</sub> detectors. This allowed an acquisition rate of almost 4.5 kHz while still maintaining a maximum deadtime of 20%. Because the NaI(Tl) crystals didn't have the intrinsic background present in the BaF<sub>2</sub> detectors, it was possible to lower the CFD threshold to approximately 200 keV. A fast summing module (Wiener 404 sum amplifier) made it possible to create a fast sum of the four clover signals. In addition to the standard CFD signal with a 70 keV threshold, this allowed the creation of a high-energy clover trigger. Any time that more than approximately 9 MeV was deposited in the four clover crystals, the event was written to disk, even if there was not a coincidence with the NaI(Tl) detector. This additional trigger had its own bit in the NIM register so that these signals could be separated afterward. The main benefit was that it added sensitivity to ground-state transitions. The one shortfall of the clover is that it did not have the test input that was available with the single crystal HPGe. As a result, it was not possible to use a pulser to confirm the deadtime measured from the charge integration. Since the pulser deadtime and the charge deadtime were in excellent agreement in the first experiment, this loss was expected to have a minimal impact on the uncertainty of the results.

#### 2.3.4 Target Production and Monitoring

A series of evaporated CaF<sub>2</sub> targets was used for the main portion of data taking with the improved detector setup. Table 2.2 lists the details of the separate targets. Both Ta and Ni backings were used for the targets. There was no apparent difference

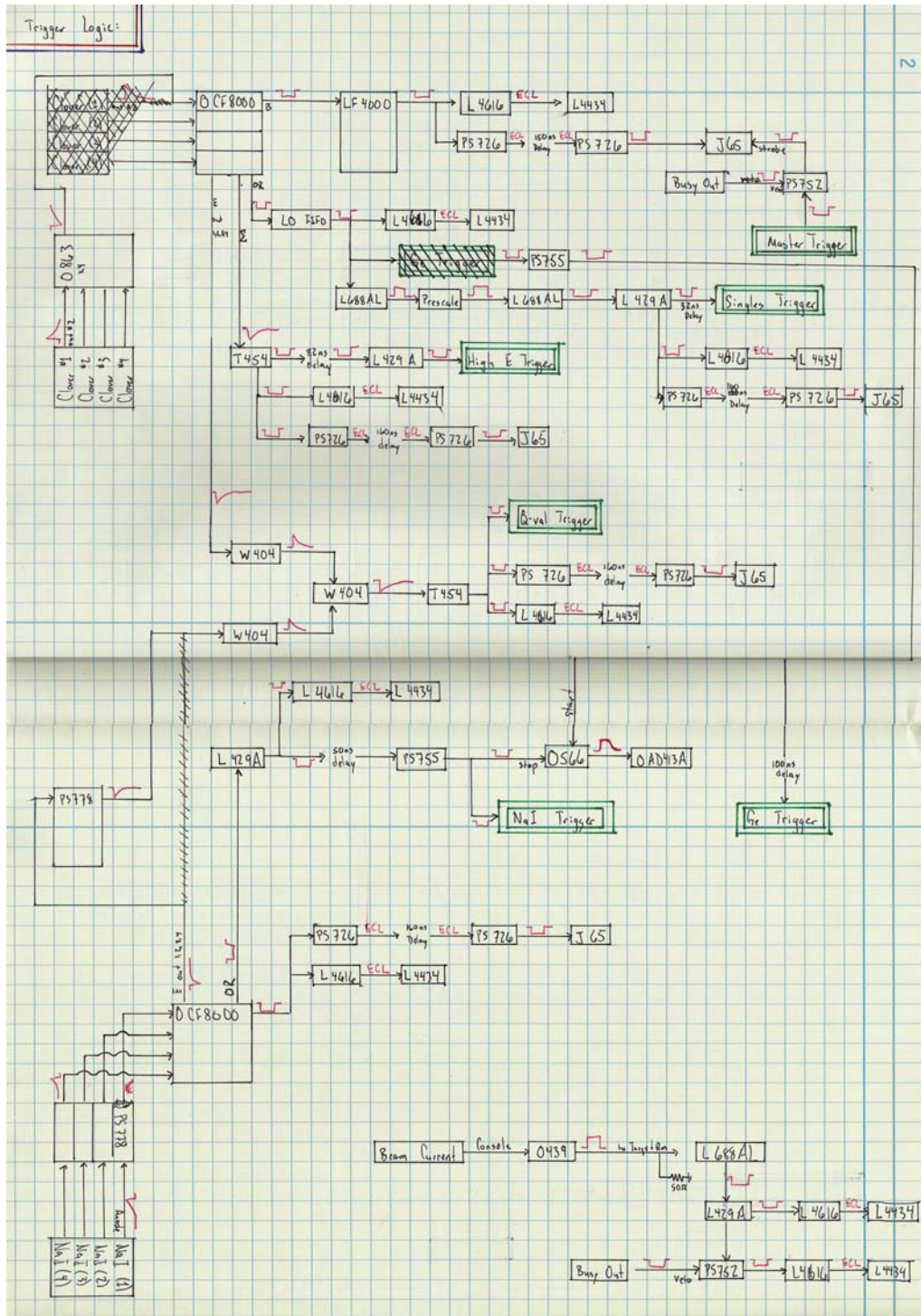


Figure 2.14. The electronics schematics for the NaI(Tl) experiment are illustrated above as recorded after the experiment. The processing of the timing signals and trigger generation is illustrated above. Note that the OR of the clover timing signals is used to create the Ge Trigger.

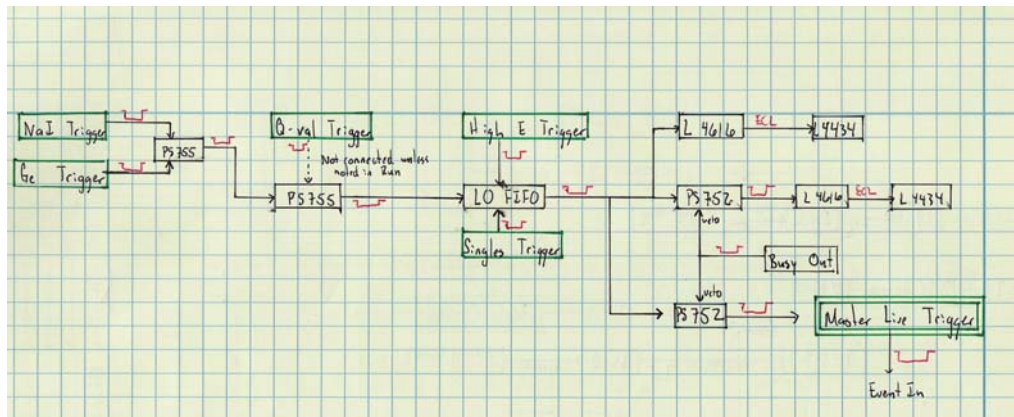


Figure 2.15. The various components of the master trigger are illustrated above. Note that while a coincidence was required between a NaI(Tl) crystal and clover crystal, the High Energy Ge and singles triggers are OR'ed in directly.

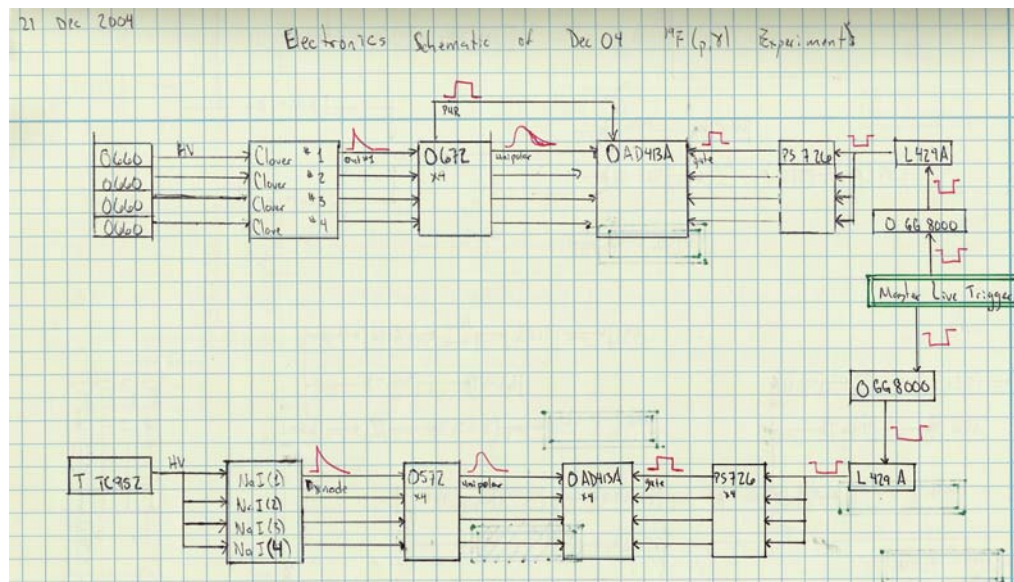


Figure 2.16. The shaping and processing of the energy signals sent to the ADCs is illustrated above. Note that all of the ADCs used were Ortec AD413As.

in F yield or stability for the two different backing materials. With the significantly increased beam currents, noticeable target degradation became a factor for which it was very important to properly account. In order to monitor the target status, scans of the 484 keV resonance were repeated frequently throughout the course of the experiment. Since it was only important to monitor the fluorine content, the  $^{19}\text{F}(\text{p},\alpha\gamma)^{16}\text{O}$  channel was used to check stability, looking at the yield from the 6.13 MeV transition to the ground-state of  $^{16}\text{O}$ . As this reaction is much stronger than the  $^{19}\text{F}(\text{p},\gamma)^{20}\text{Ne}$  reaction, it was significantly quicker to measure the target profile and could be done with a sufficiently small amount of beam so as to avoid affecting the target status by the scan. A more detailed discussion of the target scan results will be given later when discussing the data analysis.

A cold-finger was once again used to prevent carbon buildup on the surface of the target. The setup was identical to the setup described in section 2.2.3. The evaporation technique is also detailed there. An additional caution was taken of storing the targets in an argon atmosphere after production until they were put in to use in order to ensure that interaction with the water vapor did not change their composition before use. The beam was wobbled over a 0.5 x 0.6 in area on the target. The targets were water cooled as described above. The visual inspection of the targets upon removal from bombardment showed no signs of carbon buildup.

Some authors have reported that the evaporation of  $\text{CaF}_2$  changes the chemical composition and the material actually evaporated is  $\text{CaF}$  rather than  $\text{CaF}_2$  [37]. In order to check the Ca:F ratio in the target, the same evaporation technique was used to evaporate  $\text{CaF}_2$  on to a thin carbon foil. By using Rutherford back-scattering (RBS) it was possible to check the ratio directly. These results confirmed the Ca:F ratio was 1:2.

It is worth noting that two very thick targets were used in the course of the

TABLE 2.2

## TARGET PARAMETERS

Target No.	Comp.	Prod. Meth.	Backing	Thick. (Å)	$\Delta E$ (keV)
1	CaF <sub>2</sub>	Evap.	Ta	2550	24.5
2	CaF <sub>2</sub>	Evap.	Ta	2550	23.9
3	CaF <sub>2</sub>	Evap.	Ta	770	8.0
4	CaF <sub>2</sub>	Evap.	Ta	770	7.0
5	CaF <sub>2</sub>	Evap.	Ta	800	7.2
6	CaF <sub>2</sub>	Evap.	Ta	800	8.4
7	CaF <sub>2</sub>	Evap.	Ni	780	8.7
9	CaF <sub>2</sub>	Evap.	Ta	780	9.8
10	CaF <sub>2</sub>	Evap.	Ta	780	7.6
11	CaF <sub>2</sub>	Evap.	Ta	800	7.0
12	CaF <sub>2</sub>	Evap.	Ta	800	9.1
13	CaF <sub>2</sub>	Evap.	Ta	800	6.7
14	CaF <sub>2</sub>	Evap.	Ta	800	8.2
15	CaF <sub>2</sub>	Evap.	Ta	810	8.0
16	CaF <sub>2</sub>	Evap.	Ta	810	8.0
19	CaF <sub>2</sub>	Evap.	Ta	800	8.6
101	Al	Evap.	Ta	950	7.0
205	F	Impl.	Fe	N/A	5.0
301	Blank	N/A	Ni	N/A	N/A

NOTE: The first column is a record of target number to aid in keeping track of which target was which. The second column lists the material that was used to make the target. The production method, either evaporation or implantation, is in column three. The backing material is listed in column four. The fifth column lists the target thickness in Angstroms as reported by the deposition monitor. The final column lists the energy loss in the target material for 480 keV protons. Target 101 was an aluminum target used for various calibration purposes. Target 205 was an implanted target used for the energy reproducibility tests. Target 301 was a blank Ni backing used to check any proton induced background in the Ni backing that might differ from that seen from Ta.

experiment. The region from 340 keV up to 480 keV was particularly sensitive to the effects of interest. As a result, this region was scanned not only with the thinner targets to get a yield curve, but with the thicker target as well, both to provide better statistics and to confirm the observed yield. The thin target yield can be seen in figure 2.17.

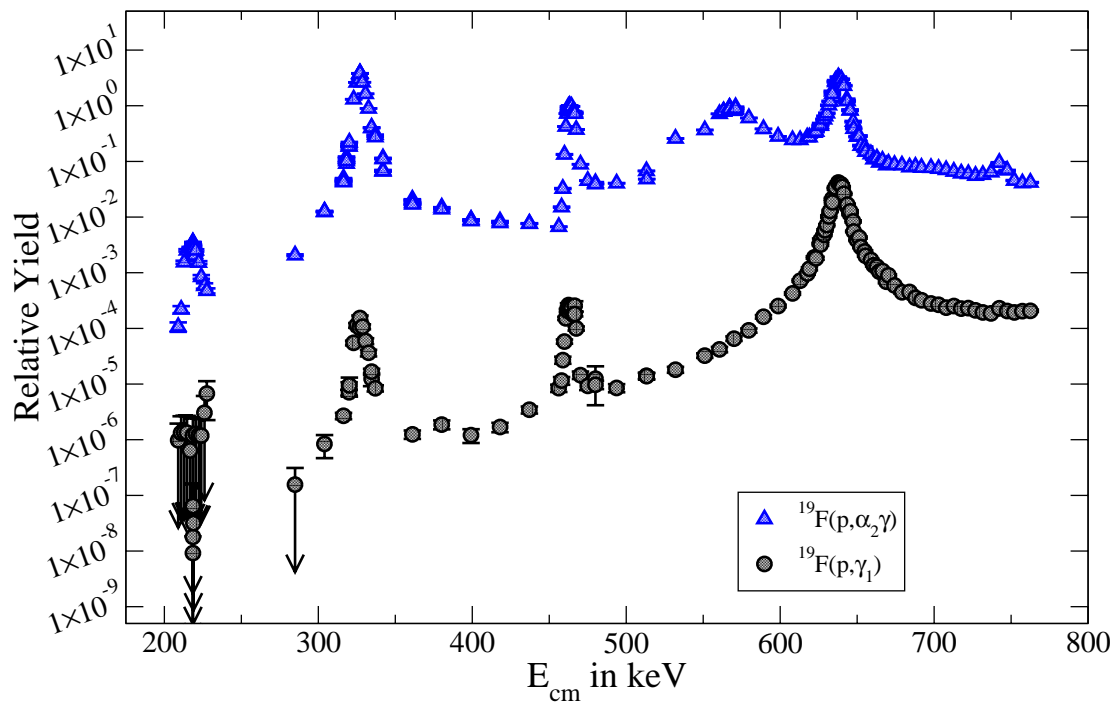


Figure 2.17. The yield curve from the experiment with the NaI(Tl) detector array is shown above. The triangular data is from the  $(p, \alpha_2)$  channel while the circles denote the  $(p, \gamma)$  channel. The yield is based on 1.63 MeV gamma-rays observed in the HPGe Clover detector in coincidence with a total energy condition in the NaI(Tl) detectors. Comparison with figure 2.6 will show the significant improvement in the sensitivity of the measurements. This is uncorrected for detector efficiency.

## CHAPTER 3

### DATA REDUCTION AND ANALYSIS

While the experiment was quite successful, there still remained a significant body of work in order to extract resonance parameters and cross-sections. The coincidence technique which made the experiment feasible also caused a reduction in the rate of good events. The intrinsic efficiency of the detectors affects the observed intensity. The targets were known to have degraded over time. All of these effects will change the excitation function and must be understood properly. Once the excitation function is well understood, there remains the difficulty of actually extracting the resonance parameters based on the fit of a Breit-Wigner cross-section. The role that each of these effects played and their attribution will be discussed in detail. The experiment using the NaI(Tl) detector array was the only one used in the final analysis because much more care was taken to make sure that the behaviour of the targets and detectors were well understood.

#### 3.1 Experimental Systematics

Before it was appropriate to consider the extraction of the resonance parameters, it was necessary to understand the components that contributed to the datasets, or the experimental systematics. This primarily included understanding the behaviour of the detectors and the targets.

### 3.1.1 Detector Calibration

In the preceding sections, it was indicated that the events were reconstructed counting on a total-energy sum over several detectors. In order to perform this type of summation, it was necessary to calibrate the energy response so that the energies from the different detectors could be added together and any binning artifacts were removed.

Some of this was accomplished by appropriately adjusting the spectroscopic amplifiers so that the gain from the individual detectors was close to the same. While this was useful for the online analysis, the precision was too poor for the offline analysis. For this reason, several gamma-ray standards were also used in order to rescale the energy of the detectors. The range of gamma-ray energies of interest was rather large, spanning from a few hundred keV up to 12 MeV. In order to determine the scaling, the gamma-rays listed in table 3.1 were fit to the corresponding channel number, yielding a channel to energy calibration for each detector as listed in table 3.2. A typical fit for a HPGe detector is illustrated in figure 3.1. For the NaI(Tl) detectors, the higher energies pose the potential for quenching, or a reduction in gain at higher energies. For this reason, a quadratic fit was done as well as a linear fit. There was no evidence of quenching in the fits, as can be seen in figure 3.2. A linear fit to the data was used.

It is worth commenting on the decision to not include the highest energy gamma-rays in the calibration of the HPGe crystals. First, the energy region of interest for the HPGe detector was near 1.6 MeV, meaning that an accurate calibration above 8 MeV was not critical to the success of the work. Second, the high-energy gamma-rays from  $^{28}\text{Si}$  as observed by the HPGe crystals would be doppler shifted. The clover was positioned at  $0^\circ$ , with each of the the crystals covering a close-geometry forward angle cone. The uncertainty in the doppler correction would have

TABLE 3.1

## GAMMA-RAY CALIBRATION ENERGIES

$E_\gamma$ (keV)	Source	Nucleus	HPGe	NaI(Tl)	Reference
1173.2	$^{60}\text{Co}$ Source	$^{60}\text{Ni}$	yes	yes	[47]
1332.5	$^{60}\text{Co}$ Source	$^{60}\text{Ni}$	yes	yes	[47]
1460.9	Natural $^{40}\text{K}$	$^{40}\text{Ar}$ , 1 $\rightarrow$ g.s.	yes	yes	[24]
1779.0	$^{27}\text{Al}(\text{p},\gamma)$	$^{28}\text{Si}$ , 1 $\rightarrow$ g.s.	yes	yes	[24]
5107.9	$^{19}\text{F}(\text{p},\alpha_2)$	$^{16}\text{O}$ , 2 $\rightarrow$ g.s. <sup>1</sup>	yes	yes	[1, 23]
5618.9	$^{19}\text{F}(\text{p},\alpha_2)$	$^{16}\text{O}$ , 2 $\rightarrow$ g.s. <sup>2</sup>	yes	yes	[1, 23]
6130.0	$^{19}\text{F}(\text{p},\alpha_2)$	$^{16}\text{O}$ , 2 $\rightarrow$ g.s. <sup>3</sup>	yes	yes	[1]
7569. $\pm$ 1.	$^{27}\text{Al}(\text{p},\gamma)$	$^{28}\text{Si}$ , R $\rightarrow$ 2 <sup>3</sup>	no	yes	[24]
9894. $\pm$ 1.	$^{27}\text{Al}(\text{p},\gamma)$	$^{28}\text{Si}$ , R $\rightarrow$ 1 <sup>2</sup>	no	yes	[24]
10405. $\pm$ 1.	$^{27}\text{Al}(\text{p},\gamma)$	$^{28}\text{Si}$ , R $\rightarrow$ 1 <sup>3</sup>	no	yes	[24]

NOTE: The gamma-ray energies for the calibrations are listed above. For several of the reaction-gammas, single- and double-escape lines were used in addition to the photopeak. All of the lines from  $^{28}\text{Si}$  came from the depopulation 12.194 MeV state. The lines which came from a full-energy peak are denoted with an upper 3 (<sup>3</sup>). The lines from a single-escape energy are denoted with an upper 2 (<sup>2</sup>). The lines from a double-escape are denoted with an upper 1 (<sup>1</sup>). The high energy gamma rays ( $E_\gamma > 5$  MeV) from  $^{28m}\text{Si}$  all doppler-shifted due to their short lifetimes. The detectors were assumed to be at 135° and the proton energy was 633 keV.

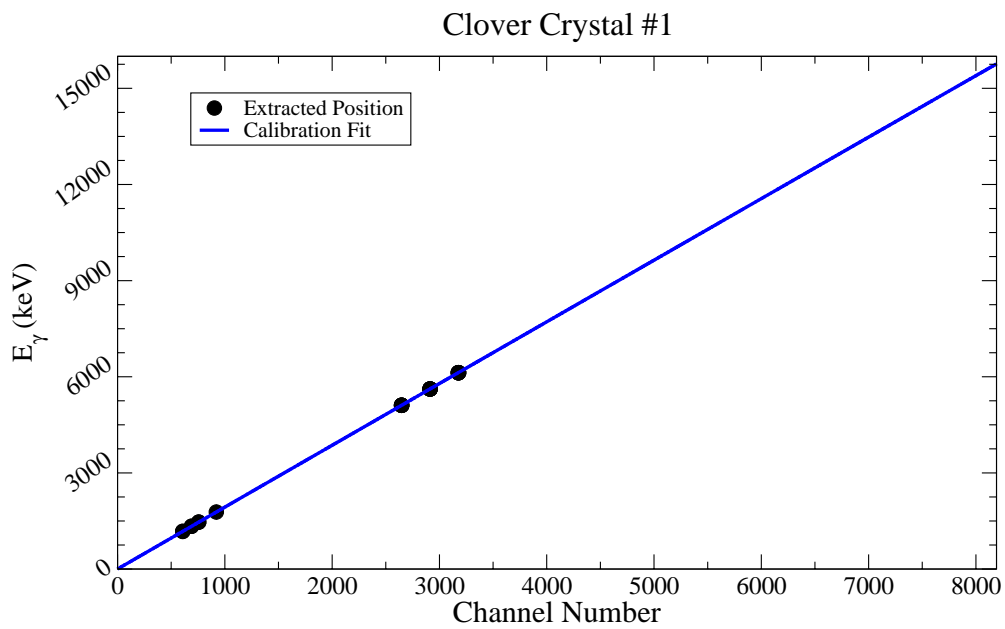


Figure 3.1. A typical fit of the channel-to-energy value for a HPGe crystal. There were no apparent non-linearities in the energy calibration. Each channel corresponded to approximately two keV before calibration.

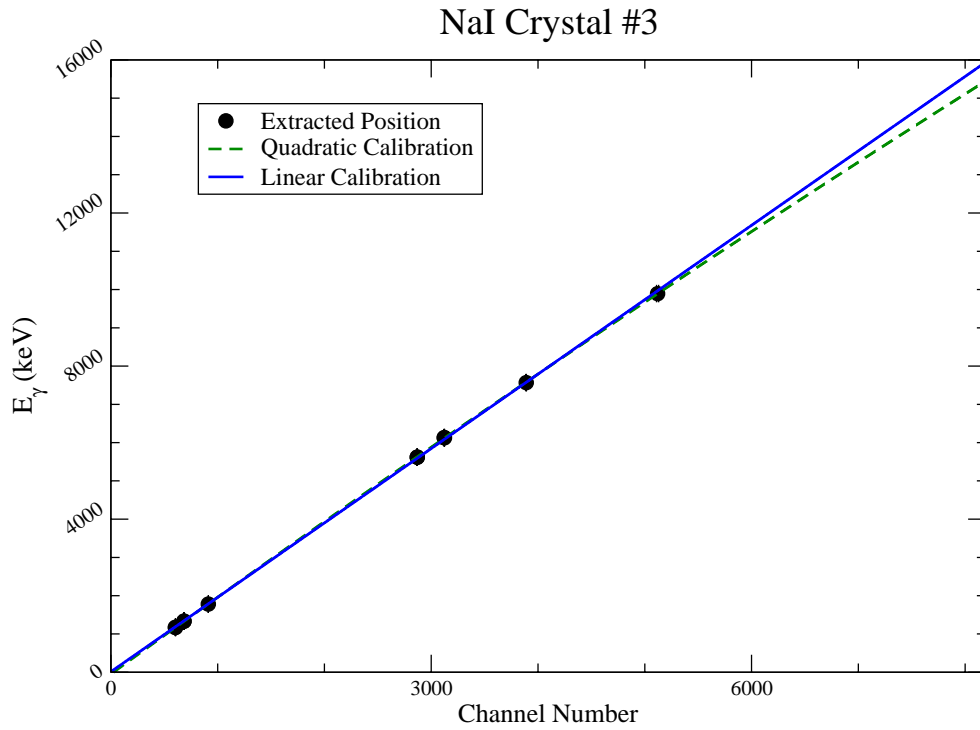


Figure 3.2. A typical fit of the channel-to-energy value for a NaI(Tl) crystal. It is worth noting the minimal difference between the linear (solid) and quadratic (dashed) fits, indicating that there was not significant signal quenching for high-energy gamma-rays. Furthermore, the curvature of the second order term is negative when quenching would lead to a positive term.

TABLE 3.2

## DETECTOR ENERGY CALIBRATION

Type	Det. No.	$a_0$	$a_1$
HPGe	1	3.0	1.9287
HPGe	2	5.2	1.9295
HPGe	3	18.5	1.9265
HPGe	4	1.3	1.9306
NaI(Tl)	1	13.6	1.9683
NaI(Tl)	2	-18.7	1.9575
NaI(Tl)	3	13.1	1.9442
NaI(Tl)	4	-8.4	1.9537

NOTE: The energy calibration constants of the individual detectors are given above. The gamma energy in keV was determined from the channel number by the formula  $E_\gamma = a_0 + a_1 * (\text{channel number})$

been much larger than the resolution of the detector, making these gamma-rays inappropriate for calibration. For the NaI(Tl) detectors, the geometry was simpler and the resolution was much worse, meaning that the remaining uncertainty to the energy was a relatively small correction. Furthermore, since the NaI(Tl) detectors were used to observe high-energy gamma-rays, it was important to have a high-energy calibration point to confirm that no quenching effects were observed.

In addition to the calibration, it was necessary to re-bin the data. A quick perusal of table 3.2 shows that while the calibration was about 2 keV/channel, this varies slightly from detector to detector. If there was no other correction made, the integer nature of the binning would result in significant artifacts which would skew the spectra. To correct for this, as each count was recorded in integer channel  $n$ , it was randomly reassigned to a real value  $x$  in the interval  $n - 0.5 \leq x \leq n + 0.5$ .

This value was then converted to an energy using the calibration determined above. It was re-binned to 2 keV/channel and the individual detectors could be summed together.

Finally, the absolute calibration, while reliable, need not be too robust for this work as the energies of the states of interest were fairly well known [1, 2]. It was only important that the calibration be the same across all of the detectors.

### 3.1.2 Corrections for Target Degradation

One of the most troubling experimental difficulties was the continual degradation of the fluorine targets. The problem is illustrated graphically in figure 3.3. As can be seen, over time the fluorine content is being removed from the target. Because the yield is turned directly into the cross-section, a changing yield due to a changing number of target atoms could lead to an incorrect cross-section if care was not taken to properly correct for it.

There are two effects which need to be accounted for separately. First, the width, or thickness, of the target changes over time. Second, the plateau height, or density of fluorine atoms, decreases over time. These two effects must be accounted for separately as they affect the yield differently at different energies. The change in plateau height is an effect that is independent of the yield structure present at a given energy. If there are less target nuclei at a given energy, less yield will be seen, regardless of the energetics of the cross-section at or near that energy. This situation can be very different for the width. Consider the yield from a narrow resonance. As long as the target thickness is much greater than the resonance width, the yield will be independent of target thickness because the resonant yield is orders of magnitude larger than the non-resonant yield. In a non-resonant region where the cross-section is relatively constant over the target thickness, however, the

Target 3,  $E_R=483.9$

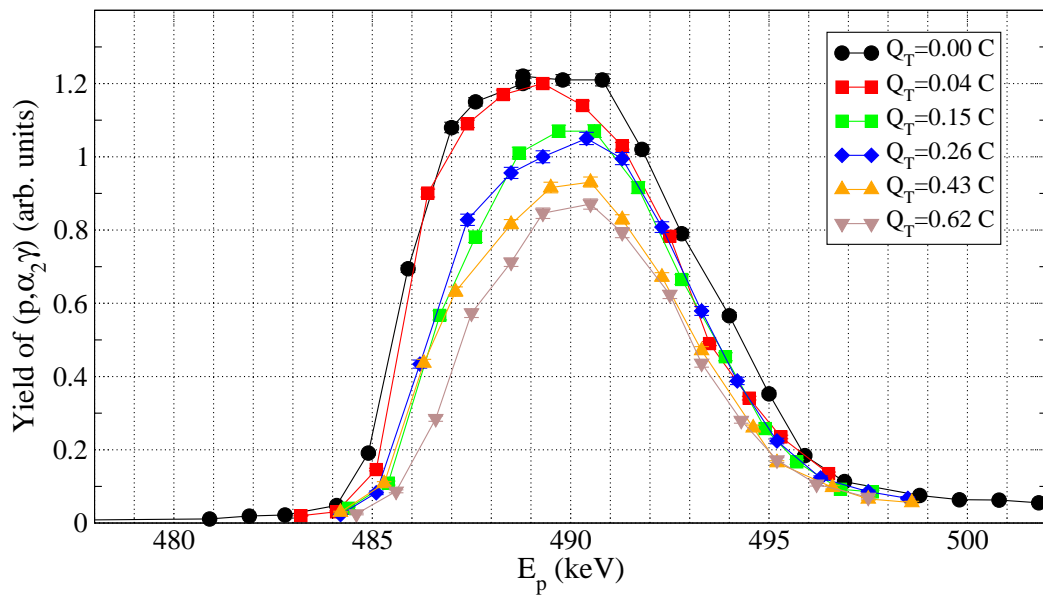


Figure 3.3. The target profile as a function of the total charge the target was exposed to is shown above. Most targets were removed after a total accumulation of  $\approx 0.5$  C. The loss of both FWHM and plateau height can be seen.

yield will be proportional to the target thickness. For this reason, it was necessary to separate out the two separate degradation effects. The target scans of the 484 keV resonance discussed in section 2.3.4 allowed corrections for both of these effects to be made. The total charge collected for a typical run ranged from a few mC up to several hundred mC. A typical target scan put less than one mC on target for the entire scan, so that the target was relatively unaffected by the additional charge deposited during a scan.

### *Target Thickness Correction*

First, the target width was parameterized as a function of charge by looking at the change in full-width half-maximum (FWHM) in the target scans. The FWHM was calculated by two independent methods in order to check the reliability. In the first methods, the data was fed into *Grace* (version 5.18) [48]. *Grace* will extract a FWHM based on the simplistic assumptions that the dataset is monotonically increasing and then monotonically decreasing. This was actually a reasonable assumption for a resonance scan. The deviations while on the plateau of the resonance did not affect the extraction. *Grace* then calculates the FWHM based on half-max crossings of the dataset.

The second parameterization made used the arctan form of the yield function given in equation 1.33. If the beam spread and straggling are both assumed to be negligible, then the general yield is integrable and can be reduced to the form

$$Y(E) = \frac{A_0}{\pi} \left[ \arctan \left( \frac{E - E_R - \xi}{\frac{\Gamma_T}{2}} \right) - \arctan \left( \frac{E - E_R}{\frac{\Gamma_T}{2}} \right) \right] [27]. \quad (3.1)$$

$A_0$  is a constant that has many things buried inside of it, but it is easy to see that it is proportional to the plateau height.  $\Gamma_T$  is the total resonance width.  $E_R$  is the resonance energy. The parameter  $\xi$  is the target thickness. This approximation is only valid the near vicinity of a resonance as it discounts any penetrability and

interference effects and only includes a single resonance. For the purposes of analyzing the target scans, this set of assumptions is reasonable. The arctan function was fit to the datasets to extract the target thicknesses as a function of accumulated charge. The results of both fits can be seen in figure 3.4. While there are outlying points, what is clear, is that there was a very rapid deterioration that thinned the target with very little charge. After this initial degradation, the target thickness was mostly constant, though there was a slight degradation. This would be consistent with the surface layer of fluorine being blown out of the lattice, leaving behind the  $\text{CaF}_2$  below it. It appeared that the Ca was not removed from the target, but remained behind, providing a buffer that slowed the liberation of further fluorine. The arctan fit was used over the *Grace* fit in the final analysis because it is less phenomenological and it measures target thickness rather than the target thickness folded in with the resonance width. It was useful to have the second method to verify that the behaviour observed was not an artifact of the method in which the width was extracted.

In the fitting of each data point, the initial thickness for that target was corrected for the total charge already deposited on the target and a new thickness was used for the target integration.

### *Plateau Height*

A similar type of exercise was necessary to correct for the change in plateau height over time. Equation 3.1 was again utilized, this time extracting the plateau height  $A_0$ . For these fits, the thickness was fixed to 20 keV and only the low-energy side of the data was used, effectively excluding any target thickness effects from influencing the fit. The second method of extracting the plateau height was much more old-fashioned, though still valid. Large size plots were printed and a plateau line was

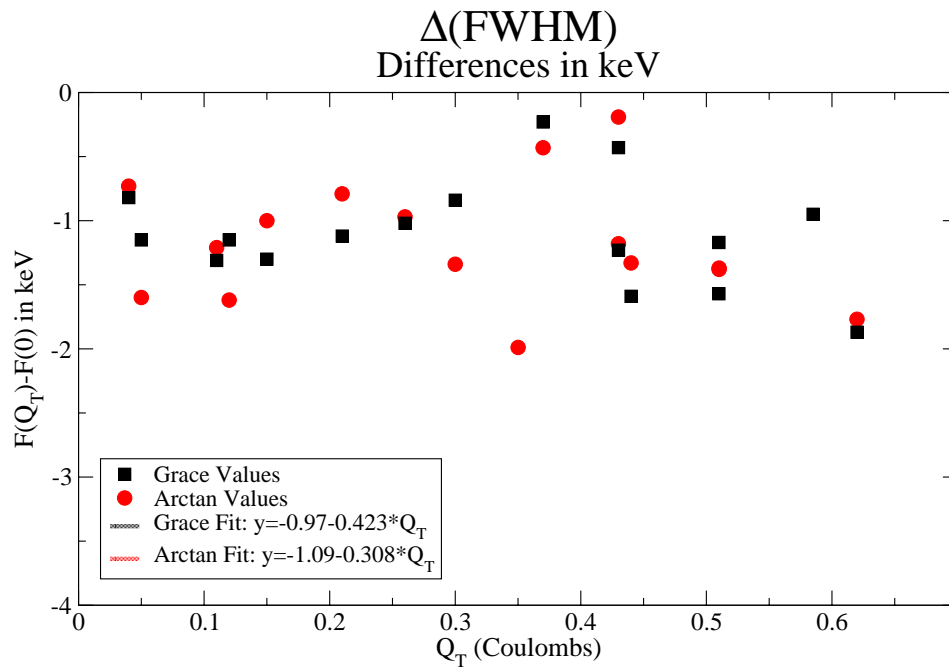


Figure 3.4. The FWHM parameterized versus total charge is shown above. For thin targets, the FWHM values ranged from about seven to nine keV.

### $\Delta(\text{Plateau Height})$

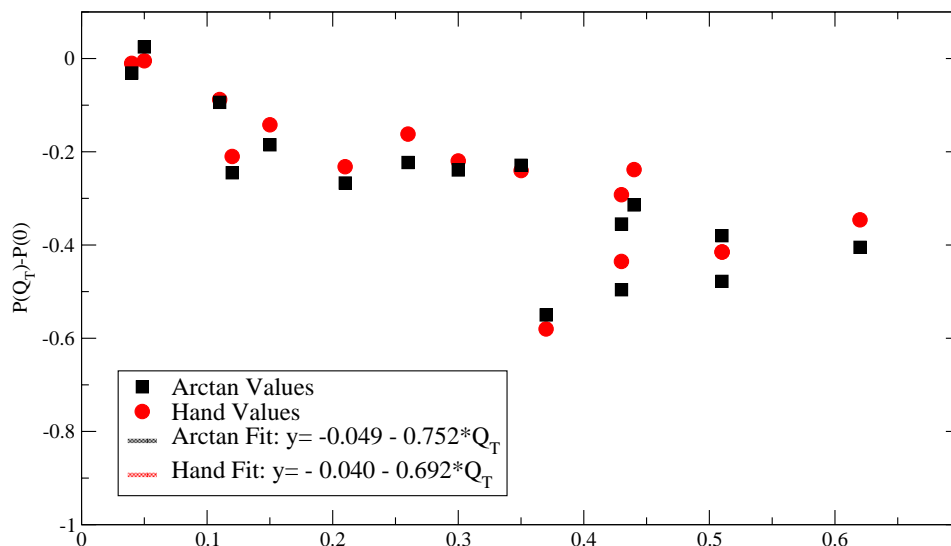


Figure 3.5. The loss of plateau height as a function of  $Q_T$  is shown above. Typical plateau heights were between 1.2 and 1.5 before seeing beam.

drawn in by hand through the target plateau. The height of the plateau was read off of the scale and later used to parameterize the loss in plateau height as a function of accumulated charge. The results of the parameterization can be seen in figure 3.5.

The plateau loss shows a rather different character than that seen for the FWHM. The “flash” effect of the initial beam that was the dominant component in the loss for the FWHM are not seen in the plateau loss. Instead, it seems to indicate that fluorine was slowly and steadily sputtered out of the target as time went passed. Typical plateau heights with this normalization ranged from 1.2 to 1.5 before seeing significant beam. The losses for targets seeing the most beam would be on the order of 30-40%. The yield for each datapoint was corrected for the expected plateau height when it was taken. The arctan fits were used for these recalibrations in order

to be consistent with the FWHM corrections.

As a final cross-check for these corrections, some crude area calculations were made and the different methods were used to determine a dependence of the target area on the accumulated charge. This is an indication of the total number of remaining target atoms, but because it neglects any information about the independent behaviour of the target width and plateau height, it is not useful as a parameterization. None-the-less, if the method used to correct for the width and height are robust, it should also properly predict the behaviour of the target area. The target area can be seen in figure 3.6. Three different methods were used to look at the area. The first was an area calculation from *Grace*. *Grace* used a Simpson's rule integration in order to find the target area. It suffers a deficiency due to the fact that the integration cannot be restricted to a certain region, but is carried out over the entire dataset. The second method, *Datint*, was a homemade Simpson's rule integration that could be restricted to the same region for all sets. Finally, the Arctan area was determined by taking the product of the arctan width and the arctan plateau height. The consistency of the fits, particularly of the slopes of the Arctan and *Datint* methods show the robustness of the correction.

### 3.1.3 Efficiency Calculations

The detection efficiency for a  $^{19}\text{F}(p,\gamma)$  event depends both upon the intrinsic efficiency of the detector and the efficiency of the detector array for capturing the total energy of the event. As such, the two components of the efficiency are discussed separately.

#### *Coincidence Efficiency*

One of the most noteworthy strengths of the detector setup was that by taking advantage of the multiplicity of the cascade and the decay energy, it was possible

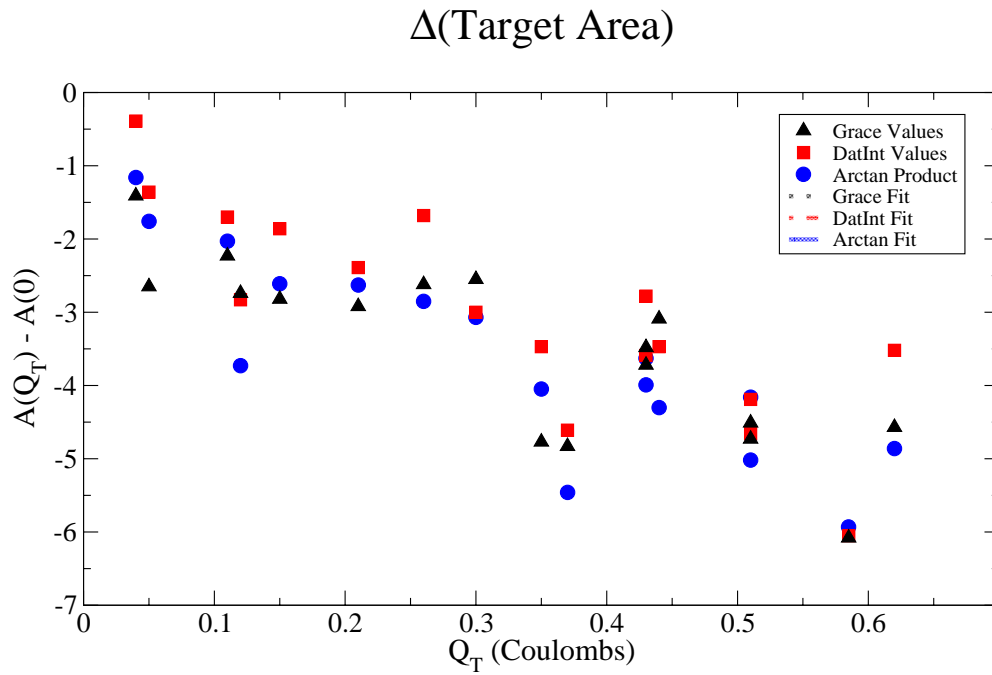


Figure 3.6. The total target area is shown versus accumulated charge. The consistency of the fits recommends the robustness of the correction procedure.

to reduce the background by several orders of magnitude. It is rare, however, that such improvements can be made at no cost. In this case, the price to be paid was in efficiency. Any time that a 1.63 MeV gamma-ray struck the HPGe detector and the corresponding primary was not detected in the NaI(Tl) detectors, a good event was thrown away. It was necessary to determine what the loss due to the coincidence requirement was.

There are several factors which contributed to the loss. The first is solid angle of the NaI(Tl) detectors. Any gamma ray that was not detected due to there not being a detector in its path was clearly a lost event. Second, any time that a high-energy gamma-ray interacted with the NaI(Tl) crystal, there is a finite probability of it depositing a majority of its energy in the detector. Since the total energy threshold was set at 9.5 MeV, the probability was dependent on the proton energy (and thus, the energy of the primary). It was reasonable to expect that there was a different probability for a 11.9 MeV gamma-ray to deposit 7.9 MeV of energy than for a 11.5 MeV gamma-ray to do the same. One of the advantages of choosing such a low threshold was that the difference in primary energies was small relative to the difference between the primary energy and the threshold energy. The effect of differing proton energies can be seen in figure 3.7.

Fortunately, near the resonance at 669 keV, the strength of the gamma branch was sufficiently strong to be seen in the singles spectrum. In order to determine the coincidence efficiency, the efficiency in the region near the resonance energy was measured by calculating the ratio of the yield of 1.63 MeV gamma-rays in the singles spectrum versus the yield in the gated spectrum. GEANT calculations for the coincidence efficiency in a  $2-\gamma$  cascade were then done for center of mass energies between 200 and 800 keV in order to determine the energy dependence of the efficiency. Because of the difficulty in properly simulating the background

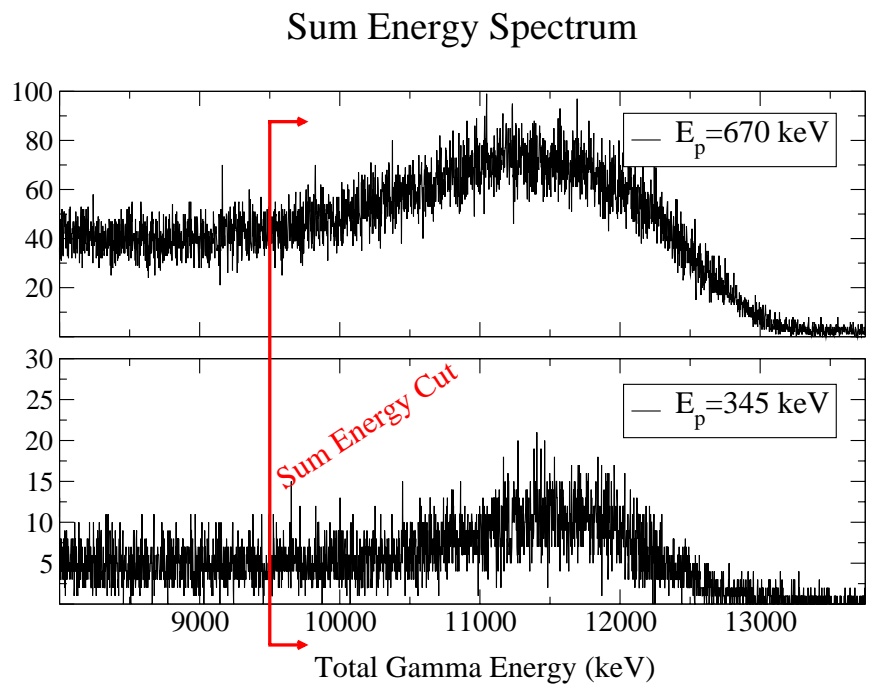


Figure 3.7. Shown above are sum energy spectra (summed over all detectors) at two different bombarding energies. The cut energy for the coincidence is also shown. Note the shift of the sum energy peak.

gamma-rays from the  $^{19}\text{F}(p,\alpha\gamma)^{16}\text{O}$  reaction, the absolute value of the efficiency was matched to the measured efficiency at the resonance energy. The efficiency did show a slight energy dependence that was included in the fitting. The coincidence efficiency was

$$C(E) = 0.193 + 1.91 \times 10^{-5} E_{cm}(keV) \pm 0.005. \quad (3.2)$$

### *Absolute Efficiency*

In order to get the efficiency of the setup, it was also necessary to determine the absolute efficiency for the detection of a single gamma-ray of energy  $E_\gamma$ . Furthermore, it was important to know not only the photopeak efficiency, but the single and double escape efficiencies as well since these lines were used in some of the yield calculations. The simplest method to determine efficiency is to use standard gamma-ray calibration sources. Because the gamma-ray energies of interest spanned from 1.6 up to 7.1 MeV, it was not possible to exclusively use gamma-ray sources. Gamma-rays from a  $^{60}\text{Co}$  source were used in addition to gamma-rays from the excited states of  $^{28}\text{Si}$  populated via  $^{27}\text{Al}(p,\gamma)$ . The  $E_p=679$  keV resonance was chosen for the calibrations because the decay scheme was relatively straight forward, there were no near-lying resonances that would be expected to contaminate the yield, the total width was rather narrow so that a thick target yield was observed, and because several transitions with gamma-rays close in energy to the gammas from  $^{19}\text{F} + p$  were strongly populated.

The absolute efficiency is simply the ratio of the number of gamma-rays observed to the number emitted. Of particular interest was the photopeak and escape efficiencies, or the number of observed gamma rays where the total gamma-energy was captured for the photopeak efficiency or total energy less the energy released from positron annihilation in the case of single and double escape efficiency.

$^{60}\text{Co}$  has a half-life of 1925.28 days [47], so the activity was effectively constant during the time of the calibration, which took only a few hours. The source had a reference activity of 10.0  $\mu\text{Ci}$  on 1 January 1969. The activity during the calibration was determined by the simple radioactive decay law,

$$A(t) = A_0 \exp\left(\frac{-t \ln 2}{t_{1/2}}\right). \quad (3.3)$$

The total number of gamma-rays from the  $^{60}\text{Co}$  source was then determined by multiplying the activity by the elapsed time.

For the number of gamma-rays from each branch of the decay of  $^{28m}\text{Si}$ , the total number of Si atoms created was first calculated. The total production of an excited state  $E_x$  for an infinitely thick target is given by the relation

$$\omega\gamma = \frac{2\epsilon}{\lambda^2} Y_\infty \quad [28] \quad (3.4)$$

where  $\omega\gamma$  is the resonance strength,  $\epsilon$  is the stopping power,  $\lambda^2$  is the center of mass wavelength, and  $Y_\infty$  is the number of excited states produced per incident particle for an infinitely thick target. While the target used in the experiment was not infinitely thick, the target thickness was greater than ten times the total resonance width, so it exhibited a full thick-target yield. Equation 3.4 can be rewritten as

$$Y_\infty = \frac{2\pi^2 \bar{\lambda}^2}{\epsilon} (\omega\gamma). \quad (3.5)$$

The stopping power  $\epsilon$  was calculated using SRIM. The value of  $\omega\gamma$  was taken from reference [38]. Finally,  $\bar{\lambda}^2$  is given by equation 1.19. It is then straight-forward to calculate the number of  $^{28}\text{Si}$  produced per proton, and consequently the total number of  $^{28}\text{Si}$  atoms in the chosen excited state.

### *Summing Corrections*

Once the total number of de-excitations is known, by comparing the number of observed gamma-rays of a given energy to the number known to have been emitted,

the absolute efficiency can be determined. Because of the close geometry and large volume of the HPGe detector, it was necessary to include a correction for summing effects. To explain the concept of summing, the decay of  $^{60}\text{Co}$  will be used. It is a simple  $2-\gamma$  cascade with exactly one path to the ground state. Suppose that the total energy of the first gamma-ray is captured in the detector. If the second gamma-ray goes in a direction such that it does not interact with the detector, this will unambiguously be identified as a photopeak for the first gamma-ray and the efficiency calculated from this event would properly reflect that the the total energy of the first gamma-ray was observed. Suppose instead, however, that the second gamma-ray interacted with the detector as well. Then the energy recorded would be greater than the total energy of first gamma-ray. An efficiency calculated based on this event would incorrectly show that the detector had not seen the total energy of the first gamma ray. Note that the amount of energy the second gamma-ray deposited is irrelevant. Any amount of energy deposited by the second gamma-ray will prevent proper identification of the first. Thus it is necessary to determine the probability that, on the condition that the first gamma-ray deposited its total energy in the detector, the second gamma-ray also deposited any amount of energy in the detector. In the case of a simple  $2-\gamma$  cascade, that correction is simply the total efficiency of observing the second gamma. That is, the true yield of the first gamma is given by

$$Y_{true}(\gamma_1) = \frac{Y_{exp}(\gamma_1)}{1 - \epsilon_{\gamma_2}^{tot}} \quad (3.6)$$

where  $Y_{exp}(\gamma_1)$  is the observed yield of  $\gamma_1$ . More generally, for a gamma-ray  $i$  in a cascade, the true yield is given by

$$Y_{true}(\gamma_i) = \frac{Y_{exp}(\gamma_i)}{1 - c_i} \quad (3.7)$$

where  $c_i$  is the probability that any other gamma-ray in the cascade was observed in the detector in addition to  $\gamma_i$ .

As is typical, the general case comes at the cost of additional complexity. All of the gamma-rays in a cascade can be indexed from  $i = 1$  to  $n$ . The choice of indexing is not important, though it is typically convenient to define  $\gamma_1$  as the decay with the highest energy decay from the resonant state  $E_x^R$ . Then  $\gamma_2$  is defined as the decay from  $E_x^R$  with the second-most energy and so on until all decays from the resonant state are exhausted. Indexing continues from the most energetic state below  $E_x^R$  that is populated by a cascade. A gamma-ray  $\gamma_i$  decays from a state  $E_{x_i}$  with probability  $P_i$ . It is worth noting that the excited states  $E_{x_i}$  are not necessarily uniquely labeled. The branching ratio  $B_i$  is defined as the probability that a decay from  $E_x^R$  will include  $\gamma_i$ . This is different from  $P_i$ , which is the probability that a decay from  $E_{x_i}$  will include  $\gamma_i$ . With this indexing the correction factor  $c_i$  for gamma-ray  $\gamma_i$  can be written as

$$c_i = \frac{1}{B_i} \sum_{\alpha_i} \left( \left( \prod_{a(\alpha_i)} P_{a(\alpha_i)} \right) \left( -\epsilon_i + \sum_{a(\alpha_i)} \epsilon_{a(\alpha_i)} \right) \right) \quad (3.8)$$

where

$$B_i \equiv \sum_{\alpha_i} \left( \prod_{a(\alpha_i)} P_{a(\alpha_i)} \right). \quad (3.9)$$

The sum over  $\alpha_i$  is a sum over all cascades that include  $\gamma_i$ . The index  $a(\alpha_i)$  indicates a sum (or product) over all gamma-rays in a cascade  $\alpha_i$ . Note that  $a(\alpha_i)$  includes  $\gamma_i$ , necessitating the somewhat clunky  $-\epsilon_i$  term before the sum. The  $\epsilon_i$  are the total efficiencies for detecting  $\gamma_i$ . The superscript “tot” used above was omitted for brevity. While a more complicated example will not be given here, the calculations of the summing corrections and branching ratios for the 679 keV resonance in  $^{27}\text{Al}(p,\gamma)$  and  $^{60}\text{Co}$  can be found and followed in Appendix D.

The total efficiencies were determined by integrating the energy dependent at-

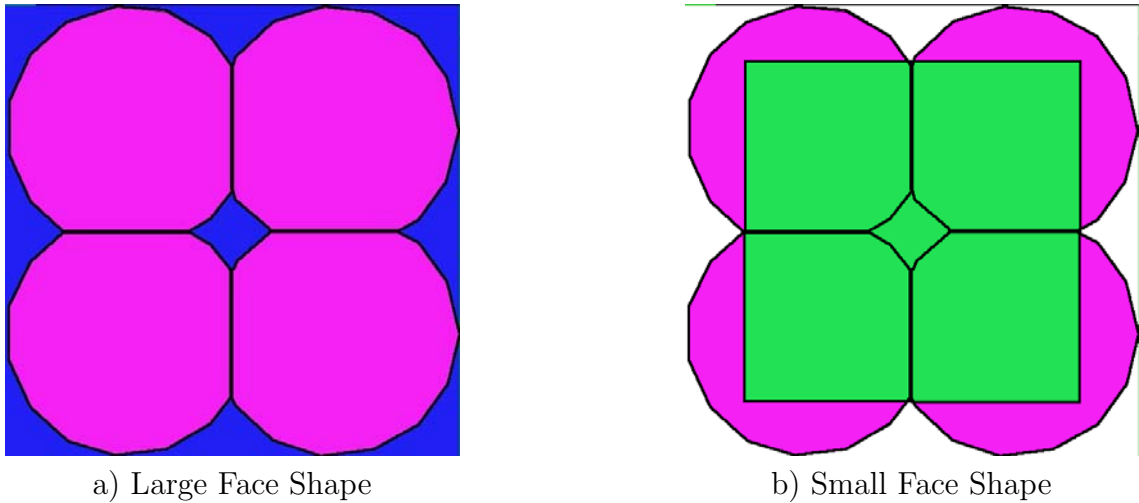


Figure 3.8. On the left in panel a) is shown a the area used for the of the total efficiency for a detector face larger than the actual clover. The region in blue (dark) tangent to the purple detector was included. On the right in panel b) shown in green (light) is the smaller detector area, lying entirely inside the actual detector volume, except for the small area directly at the center which contributed minimally to the solid angle.

tenuation coefficient for Ge over the solid angle subtended by the HPGe. The calculation assumed a rectangular crystal coaxial with the beam or source. Calculations were done for rectangular faces that were both larger and smaller than the actual crystal faces as illustrated in figure 3.8. The efficiencies showed a variation of 5%, so the two values were averaged and a 3% error was assigned to the efficiency. The method, both of calculating efficiency and determining the solid angle, is certainly not exact, but it is sufficiently accurate for determining the summing corrections [20]. By far, the largest source of uncertainty in the efficiency calibration came from the uncertainty in the resonance strength for the  $^{27}\text{Al}(p,\gamma)$  reaction.

Once the summing corrections were made, the absolute efficiency was extracted from the yield of the gamma-rays. The absolute efficiency as a function of energy for the photopeak is shown in figure 3.9. The photopeak efficiency was fit in two

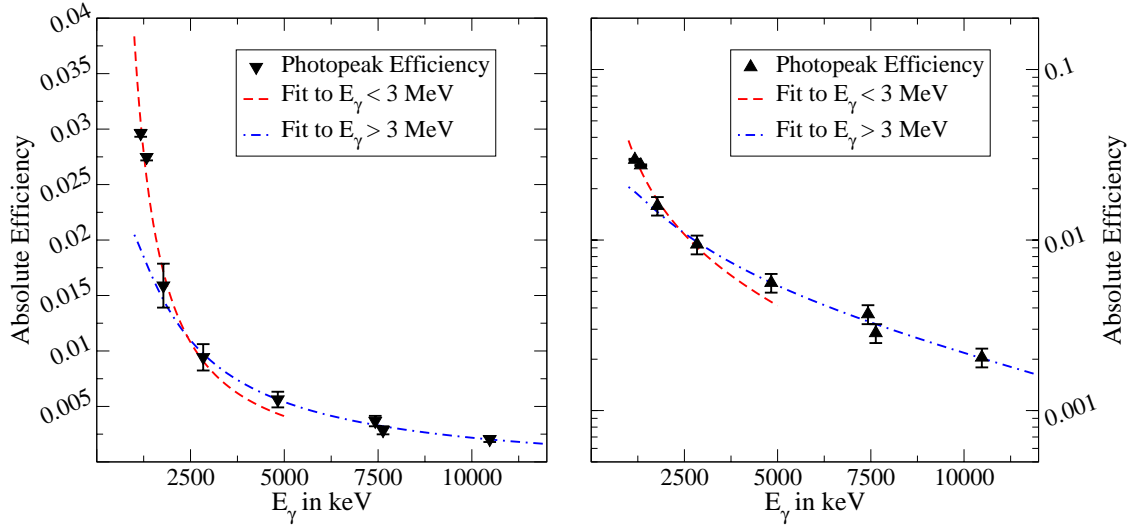


Figure 3.9. The efficiency illustrated on the left and right is the same. It has been shown both on a log plot as well as a linear plot in order to illustrate highlight the shape of the fit and the data.

separate regions, above and below 3000 keV. This was the level at which the escape lines started to make a contribution. The photo-peak efficiency was fit to a function of the form

$$\varepsilon = a_0 + \frac{a_1}{E_\gamma} + \frac{a_2}{E_\gamma^2}. \quad (3.10)$$

The choice of the fitting function was purely phenomenological. It does, however, nicely reproduce the shape and curvature of the the measured values both in linear and logarithmic scales. The goal of the efficiency calibration is to extract the efficiency for the gamma-rays observed in the  $^{19}\text{F} + p$  reaction. These gamma-ray energies fall between the calibration points. Since these can be obtained by interpolating between the measured values and whatever the true shape of the efficiency, it will be smooth, the decision to use a phenomenological fit is reasonable. The fit of the high and low energy regions is also illustrated in figure 3.9

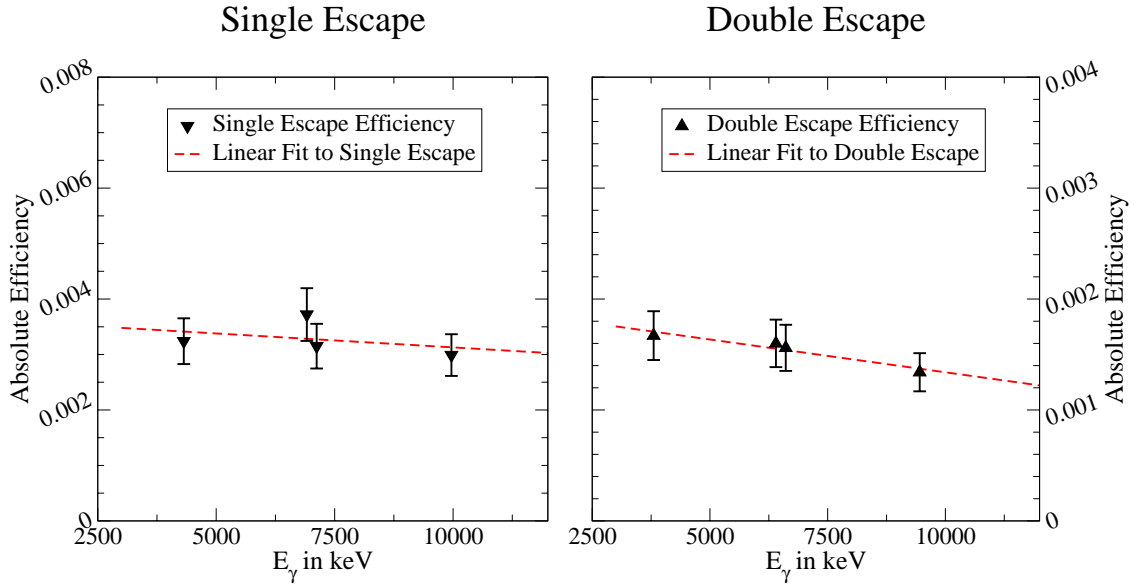


Figure 3.10. The single-escape efficiency is illustrated together with a linear fit to the data on the right. The left panel shows the double-escape efficiency. The efficiencies were very linear in the region of interest.

The efficiencies for the single- and double-escape peaks were also determined. Because of the higher energies necessary to observe these peak, there were fewer calibration points available. That being said, the efficiencies were very linear in the region of interest, so a linear fit was used to determine the efficiencies in those regions. The escape efficiencies are shown in figure 3.10.

Considerable effort has been dedicated to determining the summing correction factors for the gamma-decays of  $^{28}\text{Si}$ . It is important to say a few words about why it is not necessary to make such corrections for the cascade from  $^{20}\text{Ne}$ . First, the cascade from  $^{20}\text{Ne}$  was seen to be significantly simpler than the decay from  $^{28}\text{Si}$ . For one of the observed resonances, there was a weak ( $\approx 5\%$ ) branching to a state other than the first excited state. For all other measured resonances, the only branching which was observed was the  $R \rightarrow 1$  transition to the first excited state

followed by decay to the ground state. Second, and perhaps more importantly, the coincidence requirement, the geometry of the setup, and the sum-energy gating condition effectively excluded the possibility of summing out of the 1.63 MeV line in the HPGe detector. Recall the requirement for a “good” event to be looked for in the HPGe. First, there had to be observed gammas both in a HPGe crystal in the clover and a NaI(Tl) crystal within a 100ns window. Second, the total energy observed from the HPGe elements and the NaI(Tl) crystals within that 100ns window had to be in excess of 9.5 MeV. Because the decay was almost exclusively through a  $2\text{-}\gamma$  cascade, the only way to have a good event in the HPGe that is summed out is for the primary to interact with the HPGe clover, deposit less than  $\approx 2$  MeV, scatter out, and then deposit at least 7.8 MeV in a NaI(Tl) detector or to first hit the NaI(Tl), depositing at least 7.8 MeV before scattering out and depositing energy in an HPGe crystal. The energetic constraints are rather stringent, making it an unlikely event. Furthermore, the detectors were positioned to minimize cross-talk—exactly the type of event that would be needed for summing-out. If this is compared to the geometry used with the BaF<sub>2</sub> detectors described above in section 2.2, it becomes clear why some of the changes were made. By not having detectors surrounding the HPGe detector, the summing contributions for such a simple decay are made negligible.

Mention should also be made of the efficiency of the NaI(Tl) detectors. It was necessary to make careful, energy-dependent efficiency calibrations for the HPGe detector because there were gamma-rays of interest to be studied over a relatively wide range of energies and the efficiency had a strong energy dependence. In the case of the NaI(Tl) detectors, the basic question was “What is the efficiency for seeing more than 7.8 MeV of energy from a gamma-ray with energy between 11.4 and 12.0 MeV of energy?” The range of energies was small. The range of acceptance was large. Furthermore, the energy dependence of the efficiency of such large crystals

with high-energy gamma-rays is expected to be fairly flat [31]. The only important component of the NaI(Tl) efficiency is its effect on the coincidence efficiency. As a result, the determination of the coincidence efficiency folds in the absolute efficiency of the NaI(Tl) detectors. The relatively small energy dependence of the coincidence indicates that the assumption that absolute efficiency of the NaI(Tl) detectors was flat at the energies of interest was firm.

### 3.2 Fitting Systematics

There has already been rather lengthy discussion of the efficiency of various gating conditions, decisions on timing windows, etc. It seems appropriate at this point to actually show the results of these cuts and the resulting rather clean gamma-ray yield. Figures 3.11, 3.12, 3.13, and 3.14 display the gamma-ray spectrum for two different resonances with and without the gating conditions. Without question, if the only goal of the experiment were to measure the 633 keV resonance, then the gain in single-to-background is probably not great enough to justify the loss of efficiency. That being said, the gated spectrum is certainly cleaner. It is even possible to observe the transition to the second excited state which is typically buried in the Compton continuum.

Compare this with the case in figure 3.13. Here the gamma strength is clearly much smaller, making it impossible to isolate the 1.63 MeV transition. By applying the gating conditions as was done to give figure 3.14, the weak transition suddenly becomes much easier to observe. The gating technique does not remove all of the 6.13 MeV lines—in fact, they still are a majority of the spectrum. It does, however, clean out most of the noise at lower energies so that with the high resolution of the HPGe detector, the lines of interest are visible. It would have been possible to further reduce the lines from  $(p,\alpha)$ , but at a cost of coincidence efficiency. The

## Single Yield at 632 keV Resonance

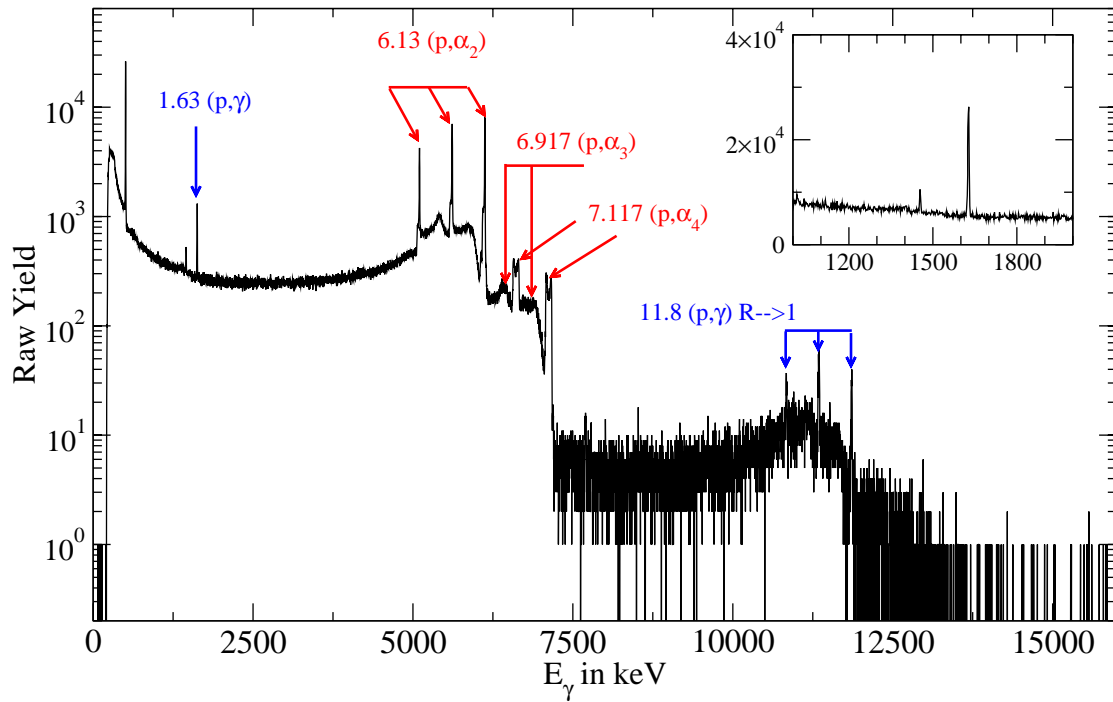


Figure 3.11. A gamma-ray singles spectrum is shown to illustrate the lines seen during the experiment. The spectrum is for  $E_{cm}=632$  keV. The inset is a linear look at the region around the 1.629 MeV gamma-ray. The ratio of (p, $\gamma$ ) to (p, $\alpha$ ) for this energy is by far the best for any of the energies measured

## Gated Yield at 632 keV Resonance

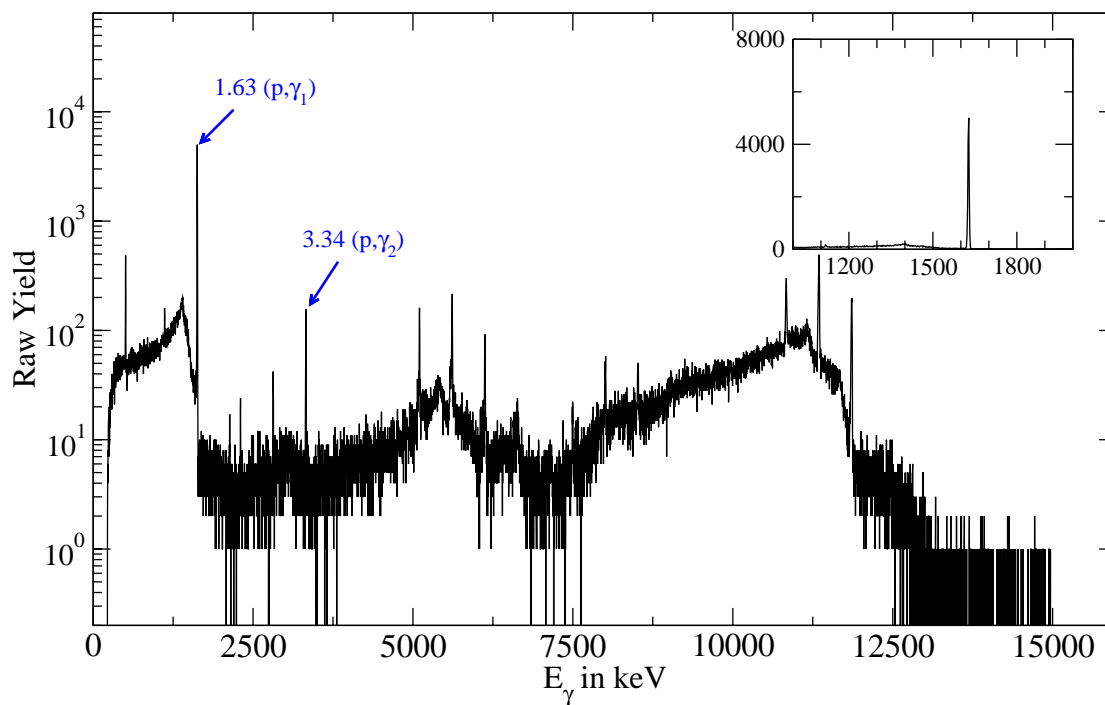


Figure 3.12. This is energy as shown before ( $E_{cm}=632$  keV), but this spectrum is gated on the Q-value and timing as discussed elsewhere. Note that the transition from the second excited state is now very clear where it was hidden before.

## Single Yield at 324 keV Resonance

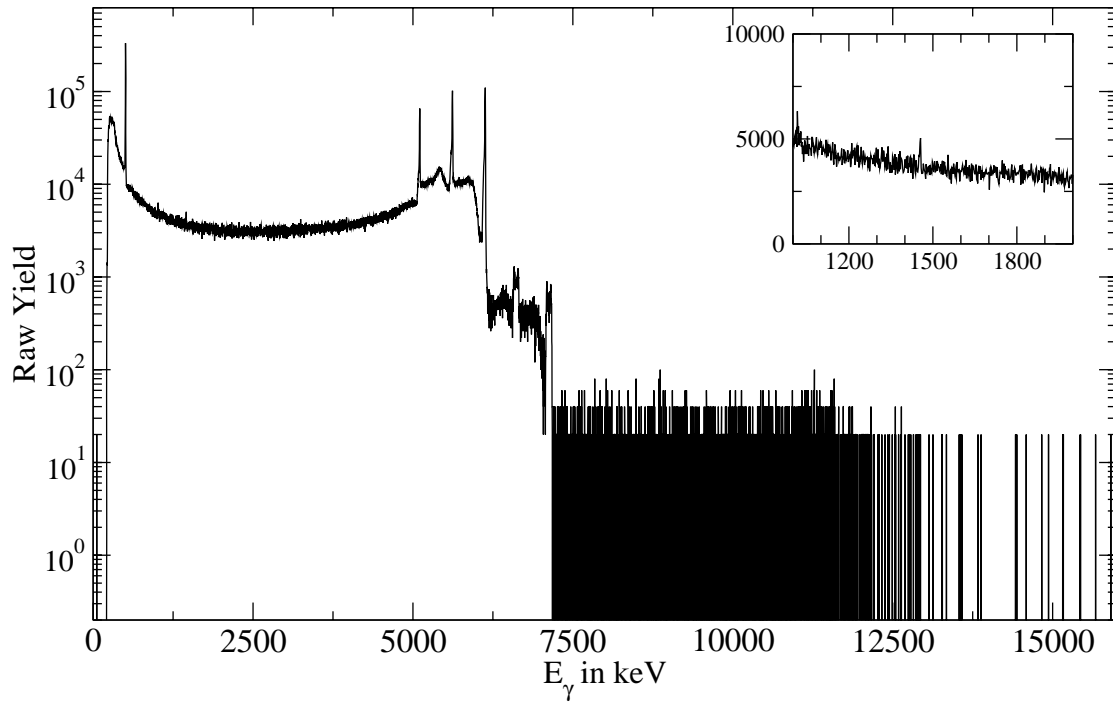


Figure 3.13. The gamma-ray singles for  $E_{cm}=324$  keV presents significantly more difficulty in isolating the 1.63 MeV transition from the first excited state. It is worth noting that the small line seen in the inset is actually from  $^{40}\text{K}$ , a contamination unavoidable in rooms with concrete.

## Gated Yield at 324 keV Resonance

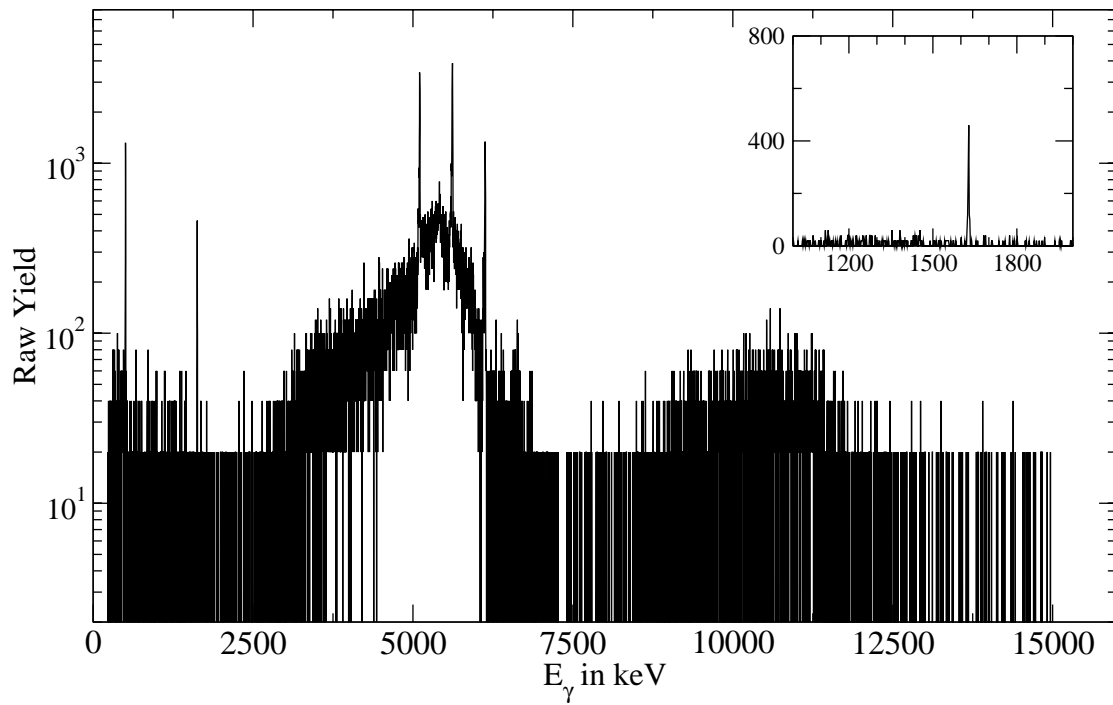


Figure 3.14. The true power of the gating conditions are seen here at the same energy as figure 3.13. While before the 1.63 MeV line was completely obscured, it now can be clearly seen.

decision was made that the spectrum was sufficiently clean at this level and that further gains in signal to background would be too expensive to be practical.

### 3.2.1 Yield Extraction

The gamma-ray yield was extracted by fitting the background near the peaks with a polynomial and then integrating the peak area. The background was subtracted from the raw integration. For the 1.63 MeV line, a linear fit was sufficient. For most of the other gamma-rays, a cubic was used. Each photopeak and escape line was integrated separately. All of the yields for the  $(p,\alpha)$  channels were determined from the singles spectrum that was taken in prescaling mode. The yield for the  $(p,\gamma)$  channel was determined from the gated spectrum. For the yield in the  $(p,\alpha)$  channels, the escape lines represented a significant fraction of the yield. The doppler broadening of the gamma-rays from the third and fourth excited states of  $^{16}\text{O}$  significantly increased the uncertainty in the yield of these lines as it spread the events over a range of 30-40 keV. It was an inconvenient accident that the fourth and second excited state of  $^{16}\text{O}$  differed by about 1 MeV. As a result, neither the photopeak of the  $(p,\alpha_2)$  nor the double-escape of the  $(p,\alpha_4)$  was usable. The yield for  $(p,\alpha_2)$  was based on the observed single- and double-escape events. The yields for  $(p,\alpha_{3,4})$  were determined based on the photopeak and single-escape lines.

All of the yields were normalized to the integrated live charge. The  $(p,\alpha)$  yields were then multiplied by the prescaling factor in order to properly represent the yield that would have been seen in a pure singles mode of running.

### 3.2.2 The Fitting Function

The yield was fit with a generalized version of equation 1.33. The energy range covered experimentally ranged from  $E_{cm} = \sim 200\text{-}760$  keV. The resonances included in the yield fitting corresponded to center-of-mass energies of 211, 324, 461, 563,

635, and 738 keV. The T=1 resonance at  $E_{cm}=1351$  and the giant dipole resonance (GDR) at  $E_{cm} \approx 5000$  keV were included in the fit though they were not measured directly. The GDR made little contribution to the yield, but the 1351 keV resonance turned out to be important to properly fit the high-energy tail of the (p, $\gamma$ ) dataset. The total yield was the sum of the yield from the individual channels. One of the major improvements in this measurement over previous measurements was that the yield between resonances was measured so that the interference effects could be observed. The interference cross-section for capture is

$$\sigma_{i,j}^{int}(E) = \pm 2 \delta_{l_i}^{l_j} \sqrt{\sigma_i(E)\sigma_j(E)} \cos(\phi_i - \phi_j) \quad (3.11)$$

where

$\sigma_i(E)$  is the resonant cross – section,

and

$$\phi_i = \arctan\left(\frac{\Gamma}{2(E - E_R)}\right) \quad (3.12)$$

is the hard – sphere phase shift.

The sign of the interference term is a parameter that can only be fixed by measuring the yield and determining when the interference is constructive or destructive. All of the terms were integrated over the target thickness in energy. Figure 3.15 shows a hypothetical predicted yield curve as well as the resonant yield contribution from each of the included resonances. It is a hypothetical prediction because target width and plateau height were fixed for the calculation, a useful assumption for pedantic purposes. Note that the total yield is not simply the sum of the different resonant contributions. For simplicity, the interference components are not illustrated in figure 3.15. Figure 3.16 shows selected resonances and the absolute value of interference components. Visual inspection shows just how important the inclusion of the interference components is in order to correctly fit the data. Near

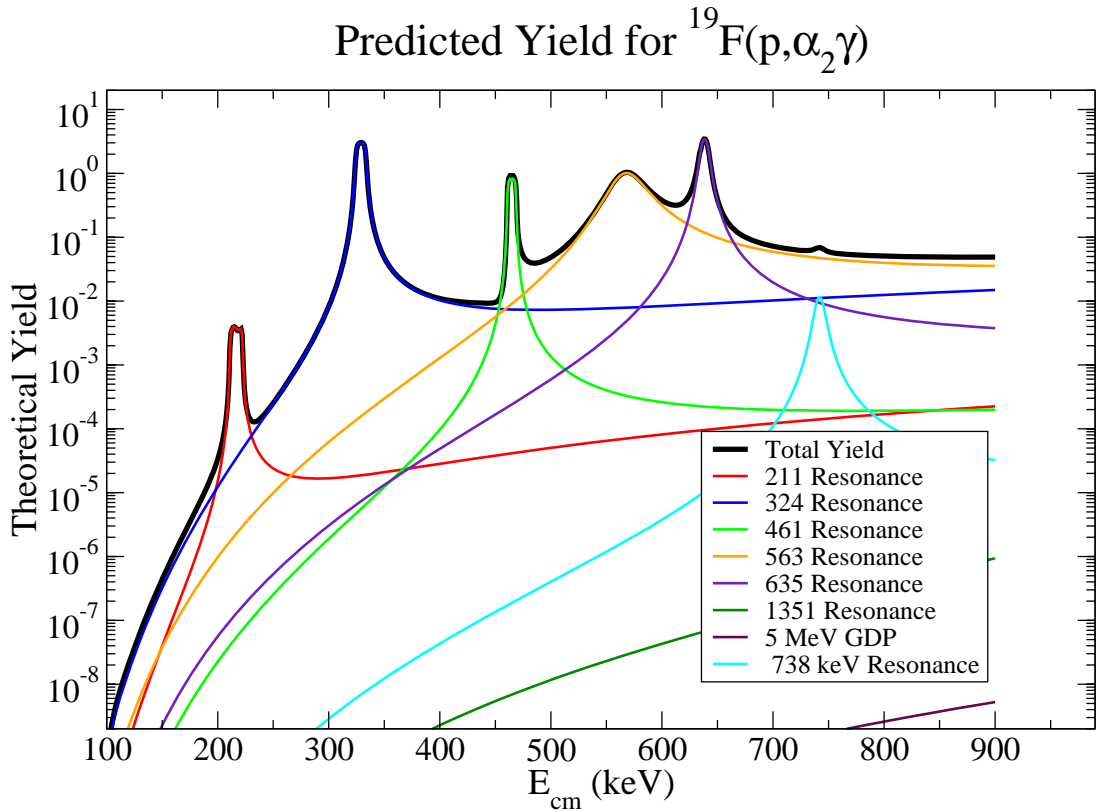


Figure 3.15. A hypothetical yield prediction is shown above for a target of fixed  $\text{FWHM} = 8 \text{ keV}$  is shown above. For this example, the target was assumed to be indestructible. The interference components of the total yield are not illustrated.

the 324 keV and 461 keV resonances, the interference components are the second largest component in the yield—thus the correct sign of that component is critical to a proper fit.

In the discussion of the absolute efficiency calculations, the yield from a thick target was given by equation 3.5. There is a similarly simple expression for the thin-target yield when the target thickness is much less than the resonance width. Because the resonance widths in the energy range of interest spanned from 900 eV up to over 30 keV [2], it was not practical to choose a target thickness that was

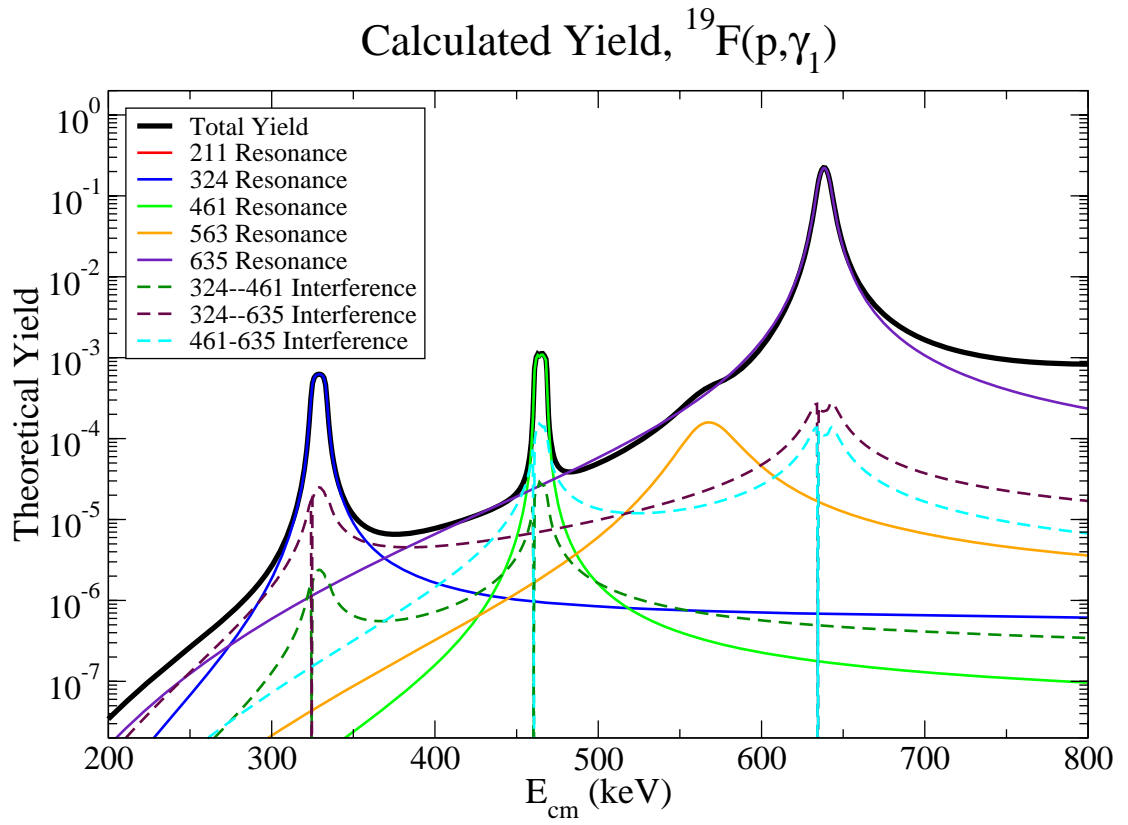


Figure 3.16. A hypothetical yield prediction is shown above for a target of fixed  $\text{FWHM} = 8$  keV is shown above. For this example, the target was assumed to be indestructible. Several interference components are shown in dashed lines. The resonant component of several resonances was omitted to reduce the clutter. Note that near the 324 keV and 461 keV resonances, the interference is a significant part of the total yield.

either thick or thin for all resonances. Furthermore, in order to include the interference terms, the simple forms are not appropriate. As a result, it was necessary to numerically integrate the Breit-Wigner form of the cross section with interference over the target thickness. The energy dependence of the energy loss was determined from the energy loss tables of SRIM-2003 [51].

Due to the careful experimental systematics, the target profile, both in plateau height and full-width-at-half-maximum had already been parameterized as a function of target number and total charge. This allowed a yield prediction for each data-point that used the same target profile as was seen by the beam. The curves shown in figure 3.15 and figure 3.16 were very smooth and well-behaved. The datasets exhibited more scatter which could be accounted for largely as target effects.

The computational intensity of this technique recommended neglecting the spread of the beam due to finite beam resolution and straggling. The bulk of the fitting was done with the functions  $g$  and  $w$  replaced by Dirac-Delta functions, collapsing the integration to a single integration over target thickness, reducing the calculation time many fold. As an additional concession to the need for rapid calculations, a table of the penetrabilities for each channel was calculated in keV steps over the energy range of interest at the beginning of the calculation and the penetrability needed for any given energy in the integration was interpolated from the table. The penetrability is a very smooth function and this should have introduced no instability in the fit.

Five reaction channels— $(p,\gamma_1)$ ,  $(p,\gamma_2)$ ,  $(p,\alpha_2)$ ,  $(p,\alpha_3)$ , and  $(p,\alpha_4)$ —were monitored over the experiment. Full datasets were available for the  $(p,\gamma_1)$  and the  $(p,\alpha_2)$  channels. The other  $\alpha$  channels exhibited strengths at some of the resonances and could have been more cleanly distinguished were it not for the doppler shift of the decays which spread the yield over about 30 keV. It was still possible to extract

resonance parameters, but the spectrum was not as clean as could be hoped. The  $(p,\gamma_2)$  was neglected as it only showed strength near the 632 resonance. In order to relate the normalized yield to the theoretical yield there remains a normalization factor which depends upon the stopping power, the target thickness and stoichiometry, and the detection efficiency. The relative normalizations between the different channels depend solely on the ratios of the absolute efficiencies. In the case of the  $(p,\gamma)$  channels, the coincidence efficiency also has to be included. It was decided to use the resonance strengths in the  $(p,\alpha_2)$  and  $(p,\alpha_4)$  channels from the thesis of Lorenz-Wirzba [37] to fix the resonance parameters  $\Gamma_p$  and  $\Gamma_{\alpha_2}$  for the 211, 324, and 460 keV resonances. The strength also fixed the partial widths  $\Gamma_{\alpha_4}$  of the 324 and 460 keV resonances. That work was a rather comprehensive measurement of the  $^{19}\text{F}(p,\alpha_i)$  reactions using Ge(Li) detectors. The systematics of that measurement were very robust, recommending the reliability of the resonance strengths. The partial widths were determined from the resonances strengths by making the basic assumption that  $\Gamma_p \ll \Gamma_{\alpha_i}$ . Since the resonance strength is defined as

$$(\omega\gamma)_i = \frac{(2J_1 + 1)}{(2J_0 + 1)(2j_0 + 1)} \frac{\Gamma_p \Gamma_i}{\Gamma_T} \quad (3.13)$$

where the  $J$ 's are defined as before, it was straightforward to deduce the partial widths.

### 3.2.3 The Fitting Methodology

With these values, the  $(p,\alpha_2)$  yield for energies below 480 keV was fit to with the yield function, allowing the resonance energies and the normalization constant to vary to achieve a minimum  $\chi^2$  deviation where  $\chi^2$  for a particular channels is given by

$$\chi^2 = \sum_{i=1}^N \left( \frac{Y_i - Y_t(E_i)}{\delta Y_i} \right)^2 \quad [40] \quad (3.14)$$

*where*

$i$  runs over all data-points,

$Y_i$  is the normalized yield for run  $i$ ,

$Y_t(E_i)$  is the predicted yield at energy  $E_i$ ,

$\delta Y_i$  is the statistical uncertainty in the measurement  $Y_i$ ,

*and*

$E_i$  is the energy of run  $i$ .

The total width was calculated internally as the sum of the partial widths to properly reflect the effect the changing partial widths would have on the total width. In addition to the six channels already mentioned, the contribution from inelastic scattering was included as a constant width. The inelastic width only contributed significantly to the width of the 1350 keV resonance. The resonance energies were treated as variables for several reasons. First, the experiment was not designed to measure the resonance energy. Second, slight changes in the resonance energy often made significant improvements in the quality of fit as the front edge would move to the front edge of the data.

With the now fixed normalization constant, the fit region was opened to the entire energy range, releasing the energies of the higher energy resonances as well as the partial widths for the higher energy resonances. Once a new minimum was found, the process was iterated to find a better normalization constant. The signs of the interference terms were manually varied to further minimize  $\chi^2$ . These iterations continued until the parameters stabilized with respect to further minimizations. The fitting of the  $(p, \alpha_2)$  set was used to determine the normalization, the observed resonance energies for all resonances, and the proton and  $\alpha$  widths for the 563, 632, and 739 keV resonances. The energies and widths of the two high-energy,

unobserved resonances were taken from literature values. A complete listing of the which datasets were used to determine which parameters can be seen in table 3.3. Once a best set of parameters was determined, the  $(p, \alpha_3)$  channel was considered. The  $\alpha_3$  partial widths and interference signs were varied to provide a minimized  $\chi^2$ . The same minimizations were made for the  $\alpha_4$  channel, subject to the constraints imposed by the Lorenz-Wirzba strengths. The  $\alpha_3$  and  $\alpha_4$  channels were important to the determination of the resonance parameters of the other channels because they contribute to the total width. Their contributions for some resonances were as much as 20-30%. With these new parameters, the fitting returned to the  $(p, \alpha_2)$  channel to iterate the effect of a potentially different total width. Once all of these fits had stabilized, the  $(p, \gamma_1)$  channel was fit with all of the  $\Gamma_{\gamma_i}$  and interference signs being open variables. Because the gamma widths were so small relative to the particle widths, they had no effect on the total width and consequently no effect on the fit of the other sets. The gamma width of the 1351 keV resonance was also varied to fit the high energy side of the 632 keV resonance. The *minuit* [5] minimization routine from the *cernlib* package was used for the minimization of the resonance parameters. This technique was highly iterative as can be seen, but tended to be fairly robust, with later iterations only making parameter adjustments on the order of a percent. The final resonance parameters are shown in table 3.5. The fits to the datasets are shown in figures 3.17, 3.18, 3.19, and 3.20.

The fits are generally very good, though there is some deviation at high energies in the  $(p, \alpha_3)$  and  $(p, \alpha_4)$  channels. It is most likely the tail of a high energy resonance that was not included in the calculation.

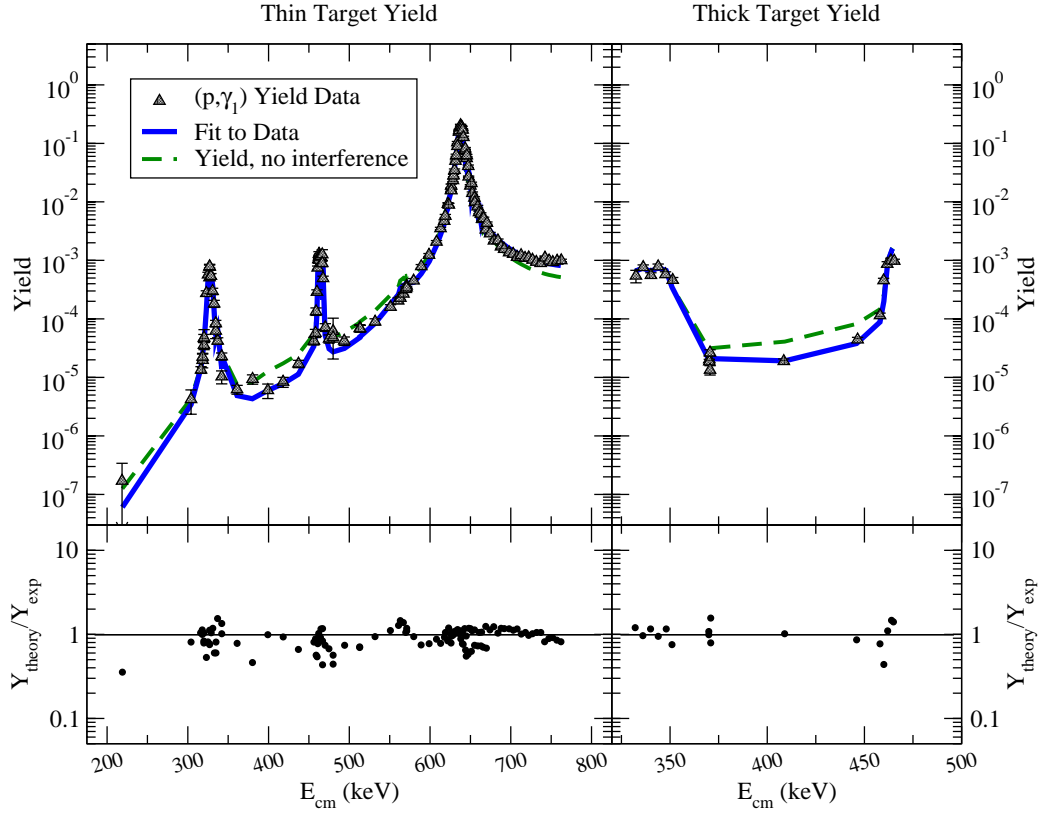


Figure 3.17. The fit to the  $^{19}\text{F}(p,\gamma_1)$  data is shown above. The gamma-ray yield is from the gated 1.63 MeV line in the clover HPGe detector.

TABLE 3.3

DATASETS USED FOR RESONANCE CONTRIBUTIONS

Channel	Norm	$E_R$	$\Gamma_T$	$\Gamma_p$	$\Gamma_{\alpha_2}$	$\Gamma_{\alpha_3}$	$\Gamma_{\alpha_4}$	$\Gamma_{\gamma_1}$
(p, $\alpha_2$ )	×	×	×	×	×			
(p, $\alpha_3$ )			×			×		
(p, $\alpha_4$ )			×				×	
(p, $\gamma_1$ )								×

NOTE: The dataset used for the determination of the resonance parameters is indicated. The proton and  $\alpha_2$  widths for the 221, 324, and 461 keV resonances were taken from reference [37].

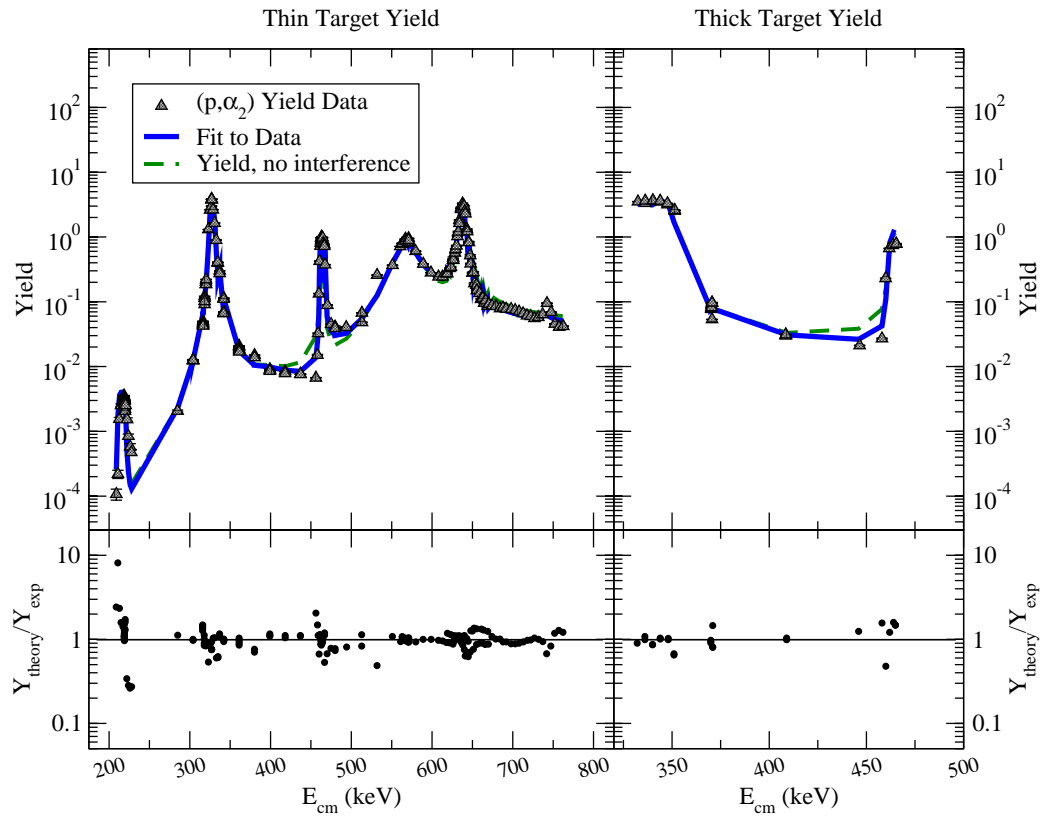


Figure 3.18. The fit to the  $^{19}\text{F}(p,\alpha_2)$  data is shown above. The yield is from the singles lines in the clover HPGe.

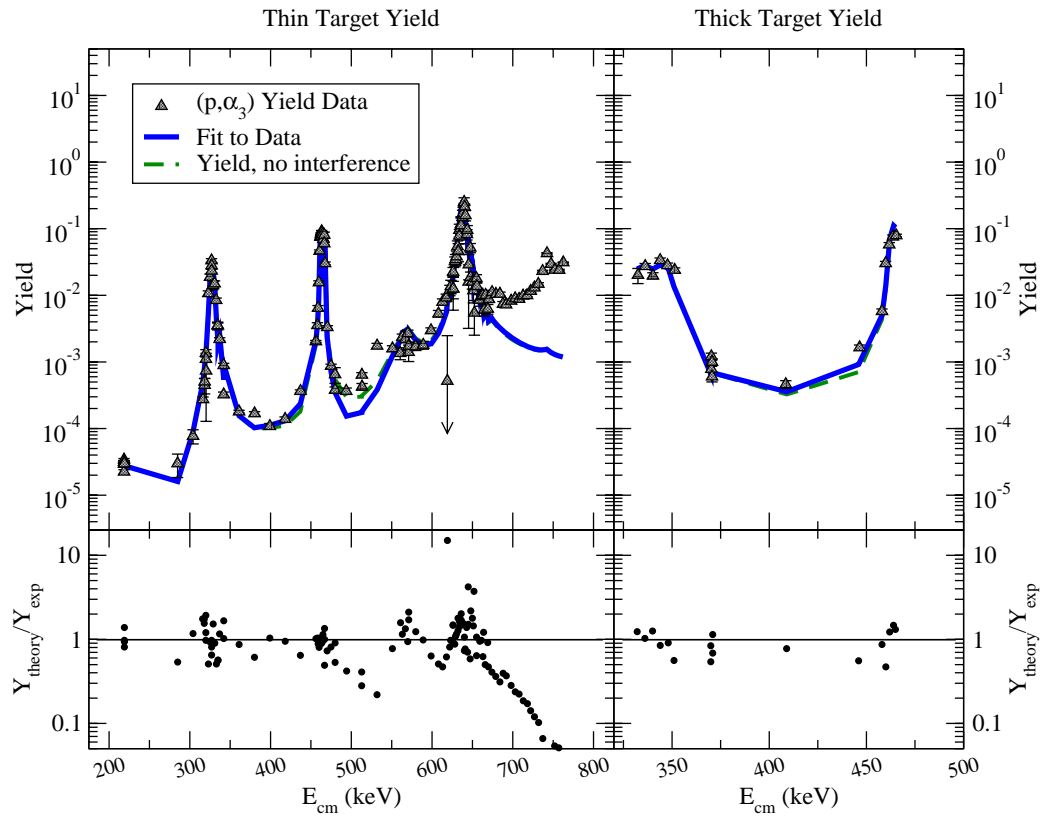


Figure 3.19. The fit to the  $^{19}\text{F}(p,\alpha_3)$  data is shown above. The yield is from the singles line in the clover HPGe.

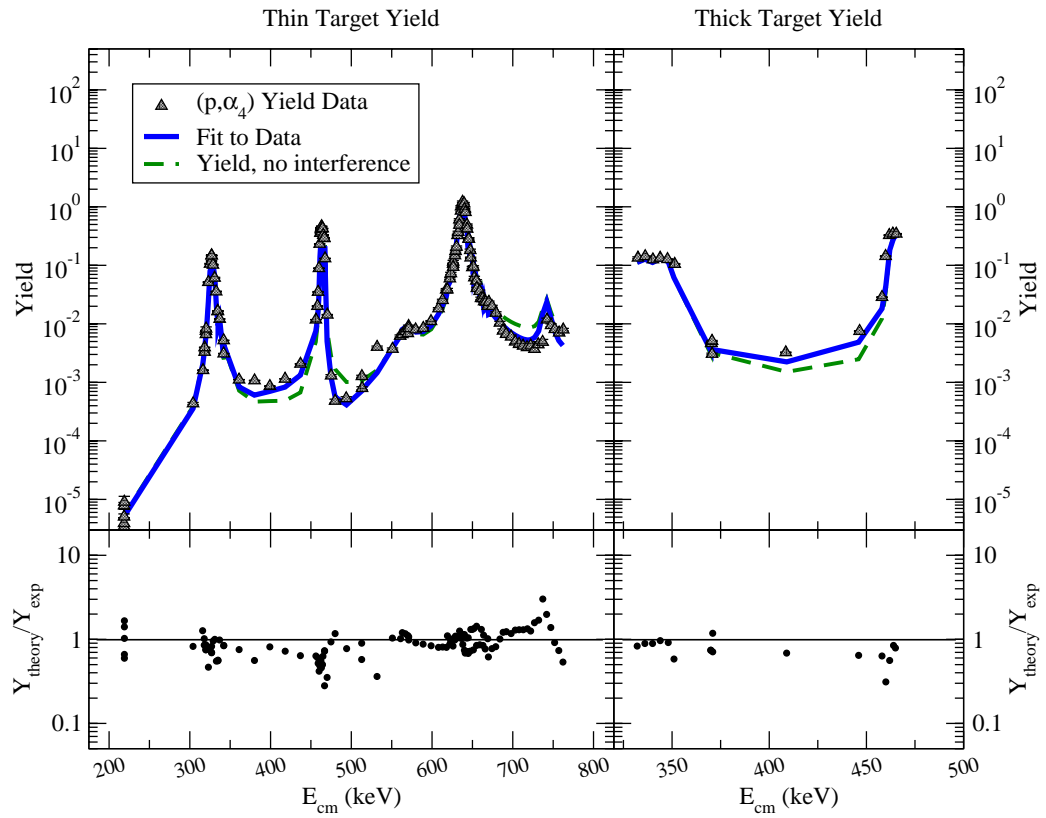


Figure 3.20. The fit to the  $^{19}\text{F}(p,\alpha_3)$  data is shown above. The yield is from the singles line in the clover HPGe.

### 3.3 Determination of Uncertainty

Until this point, the analysis has focused on the extraction of the resonance parameters and the corrections that are necessary in order to extract these values. Little has been said about the confidence that should be attributed to these values nor the effect that the treatment of the data has had on the uncertainty of the final values.

The final error in the resonance parameters comes from several different components, some more easy to attribute than others. There is the statistical error in the measurements, uncertainties due to fitting, and systematic uncertainties due to the uncertainty in prior measurements that were used as references. Each of these components will be discussed separately and then their effect on the final measurements will be given.

#### 3.3.1 Statistical Uncertainties

The observed number of a given energy for a given measurement obeys a Poisson distribution so that the  $1\text{-}\sigma$  uncertainty is given by  $\delta N = \sqrt{N}$  where  $N$  is the observed number of events [10]. Because background was subtracted from peak, the errors of the background-subtracted peak area and the background area must be added in quadrature in order to give the error in the net peak area. This process was carried out automatically by *jtek*. The excitation function which was fit was given by the events per  $10^{-8}\text{C}$  of live charge. In order to determine the error of a data-point in the excitation function it was assumed that the error in the live charge was negligible. Since the average values of the live charge ranged from  $10^5$  to  $10^7$  while typical net peak areas range from 40 up to 1000, it was a reasonable assumption. The error in the excitation function data-point was simply given by the error in the peak areas divided by the live charge in units of  $10^{-8}\text{C}$ . This was the error in the data values used for the calculation of  $\chi^2$  in equation 3.14.

### 3.3.2 Fitting Uncertainties

A significant advantage of using the *minuit* minimization package was that it can be asked to calculate the error in the minimization. A more complete discussion of the method *minuit* uses for the determination of error can be found in the Long Write-Up for the *minuit* package [5]. Both the MINOS asymmetric and HESSE parabolic errors were calculated. The errors were generally very small relative to the systematic uncertainties, and the differences between the parabolic and asymmetric errors were generally less than 5% of either error value. For this reason the parabolic errors were used for the final determination of the fit parameter uncertainty.

### 3.3.3 Systematic Uncertainties

The systematic uncertainties in these measurements deal generally with effects that will scale all of the values up or down together. They include the normalization to the Lorenz-Wirzba data, the target corrections, and efficiency corrections. They were the largest source of uncertainty in the data and will be addressed individually.

Because the systematic effects scaled the total yield, the final systematic uncertainty is

$$\frac{\delta(Y)_{sys}}{Y} = \sqrt{\sum_i \left(\frac{\delta A_i}{A_i}\right)^2} \quad (3.15)$$

where the  $A_i$  are the individual systematic correction factors and  $Y$  is the normalized yield.

#### *Lorenz-Wirzba Normalization*

Four resonance strengths from the work of Lorenz-Wirzba [37] were used to provide an absolute normalization for the measurements. Any uncertainty in the Lorenz-Wirzba values will directly introduce an uncertainty in the determination of the present values. The resonance strengths reported by Lorenz-Wirzba are shown in

TABLE 3.4

## LORENZ-WIRZBA RESONANCE STRENGTHS

$E_{R,lab}$ (keV)	Channel	$(\omega\gamma)$ (eV)	Percent Error
224	(p, $\alpha_2$ )	$(3.73\pm 0.3) \times 10^{-3}$	8%
340	(p, $\alpha_2$ )	$5.12\pm 0.25$	4.9%
340	(p, $\alpha_4$ )	$(1.3\pm 0.1) \times 10^{-1}$	8%
484	(p, $\alpha_2$ )	$1.88\pm 0.015$	0.80%
484	(p, $\alpha_4$ )	$(3.89\pm 0.04) \times 10^{-1}$	1.0%

table 3.4.

The uncertainty reported for the 484 keV resonance is suspiciously small, especially since the resonances were measured relative to the alpha yield of the 340 keV resonance. Thus the error in the normalization was conservatively set to 8%, the maximum uncertainty in any of the Lorenz-Wirzba values.

*Target Correction Uncertainties*

The importance of outliers, or data-points that fall rather far outside of the expected uncertainty, for the target corrections should not be underestimated. Inspection of figure 3.5 shows that while the fit of the plateau height versus total charge correctly interprets the trend, there still remains significant deviation. Part of the reason lies in the fact that the measurement of the target profile was very sensitive to the area of the target being scanned. The energy the beam deposited in the target layer was a function of energy, so it was reasonable to expect some energy dependence on the degradation as well. Because the some of the deviation was expected to be real and not merely statistical, it was deemed inappropriate to set the uncertainty to uncertainty in the fit which was less than 2%. Instead, the uncertainty was set to 10% of the total plateau height. The plateau height corrections were generally

less than 30%, so an uncertainty in the final plateau height of 10% will account for a significant, though still reasonable deviation from the predicted plateau height.

#### *Efficiency Correction Uncertainties*

There are two efficiency corrections which were made, one for the coincidence efficiency and the second for the relative efficiency for different energy gamma-rays. The uncertainty in the coincidence efficiency was reported with the determination of the coincidence efficiency in equation 3.2, but only contributes to the  $(p,\gamma)$  measurements. The relative uncertainty in the coincidence efficiency correction was 3%.

The uncertainty in the relative efficiencies depends on both the branching ratios and error in the fits. The errors in the fits were all less than 1% and thus, were neglected. Unfortunately, Meyer *et al.* did not provide uncertainties for the branching ratios of the primaries for the  $^{27}\text{Al}(p,\gamma)$  reaction [39]. They do provide some uncertainties for secondary decays, but since those decays are populated by the primaries, such information was of limited value, especially since the gamma-rays of most interest were  $2-\gamma$  cascades where the secondary was a ground-state transition. A 5% uncertainty was assigned to the uncertainty in the relative efficiencies.

### 3.4 Resonance Parameters

The final values for the resonance parameters are finally meaningful and can be seen in table 3.5. As expected, the systematic uncertainties dominated the total uncertainty in the values.

TABLE 3.5

## DEDUCED RESONANCE PARAMETERS

$E_{R,lab}$ (keV)	Channel	$\Gamma_i$ (eV)	Systematic	Fitting	Final
224	$\alpha_3$	6.0	0.84	0.11	$6.0 \pm 0.85$
224	$\alpha_4$	N.O.	—	—	—
224	$\gamma_1$	N.O.	—	—	—
340	$\alpha_3$	13.6	1.9	0.2	$13.6 \pm 1.9$
340	$\gamma_1$	0.13	0.02	0.003	$0.13 \pm 0.02$
340	$(\omega\gamma)_{\gamma_1}$	$(2.8 \pm 0.4) \times 10^{-4}$			
484	$\alpha_3$	58.8	8.2	0.5	$58.8 \pm 8.2$
484	$\gamma_1$	0.26	0.04	0.006	$0.26 \pm 0.04$
484	$(\omega\gamma)_{\gamma_1}$	$(6.6 \pm 1.1) \times 10^{-4}$			
597	proton	16.7	2.3	0.02	$16.7 \pm 2.3$
597	$\alpha_2$	37300	5200	56	$37300 \pm 5200$
597	$\alpha_3$	80.5	11.3	3.1	$80.5 \pm 13.7$
597	$\alpha_4$	197	28	3	$197 \pm 28$
597	$\gamma_1$	1.49	0.21	0.18	$1.49 \pm 0.28$
597	$(\omega\gamma)_{\gamma_1}$	$(8.4 \pm 1.6) \times 10^{-4}$			
669	proton	6720	940	47	$6720 \pm 940$
669	$\alpha_2$	26	4	0.13	$26 \pm 4$
669	$\alpha_3$	1.5	0.2	0.04	$1.5 \pm 0.2$
669	$\alpha_4$	7.3	1.0	0.04	$7.3 \pm 1.0$
669	$\gamma_1$	0.44	0.06	0.003	$0.44 \pm 0.06$
669	$(\omega\gamma)_{\gamma_1}$	$(3.3 \pm 0.7) \times 10^{-1}$			

## CHAPTER 4

### RESULTS AND CONCLUSIONS

#### 4.1 Comparison of Resonance Parameters

The new measurements recommend weaker resonance strengths in the  $(p,\gamma)$  channel, which can be expected to generally decrease the likelihood of breakout from the CNO cycle. A comparison of the results of this experiment to previous measurements can be seen in table 4.1. When possible, the results of previous measurements have been converted into resonance strengths for comparison. Since the strength is the term that enters directly into the calculation of the stellar reaction rate, it has the most direct impact. As a note on conventions, the energies discussed previously in the analysis were in the center-of-mass frame. For the comparison of the results, a switch will be made to the lab frame so that the measurements can be compared directly.

There are several general comments which should be made. First, comprehensive measurements are important. The advantages of having multiple channels to constrain the fitting of the data cannot be overstated. Second, advances in detectors have made attribution to the proper reaction clearer. Advances in computational speed have made it possible to include interference components which must be numerically integrated. In section 3.2.2 the importance of the interference terms was discussed. Previous authors did not have the luxury of fast computation nor did they have the data between resonances in order to see the interference.

TABLE 4.1  
COMPARISON OF MEASUREMENTS OF RESONANCE PARAMETERS

$E_{R,lab}$ (keV)	Sinclair [42]		Keszthelyi and Berkes [32, 8]			Subotić [43]		This Measurement				
	$\sigma_R$ (mb)	$(\omega\gamma)\gamma_1$ (meV)	$\Gamma_{\alpha_2}$ (eV)	$\Gamma_p$ (eV)	$\Gamma_{\gamma_1}$ (eV)	$\omega\gamma\gamma_1$ (meV)	$\Gamma_{\gamma_1}$ (eV)	$(\omega\gamma)\gamma_1$ (meV)	$\Gamma_{\alpha_2}$ (eV)	$\Gamma_p$ (eV)	$\Gamma_{\gamma_1}$ (eV)	$(\omega\gamma)\gamma_1$ (meV)
224	—	—	1000	$\approx 0.45$	$< 0.06$	$< 3 \times 10^{-2}$	—	—	(1000)	(0.0030)	N.O.	N.O.
340	—	—	{2800}	{46}	0.28	3.3	0.84	10	(2340)	(7.0)	$0.13 \pm 0.02$	$0.28 \pm 0.04$
484	—	—	700	5	0.42	1.8	0.62	2.6	(746)	(3.02)	$0.26 \pm 0.04$	$0.66 \pm 0.11$
597	—	—	{37000}	{40}	12	21.4	4.14	5.6	$37.3 \pm 5.2$ keV	$16.7 \pm 2.3$	$1.49 \pm 0.28$	$0.84 \pm 0.16$
669	0.48	820	{110}	{5600}	{2.2}	{1590}	[2.2]	[1610]	$26 \pm 4$	$6720 \pm 940$	$0.44 \pm 0.06$	$330 \pm 70$

NOTE: Shown is a comparison of the the resonance parameters obtained by previous authors to this measurement. The values from this measurement in parentheses were not measured, but taken from reference [37]. A value of N.O. meant that it was not observed. The values in braces from Keszthelyi and Berkes were taken from reference [3]. The values in brackets from Subotić for the 669 resonance were the values to which that measurement was normalized. They were obtained from reference [7]. The strengths for the Sinclair and the Keszthelyi and Berkes measurement were calculated from the parameters they reported in their measurements. All widths are reported in lab energies in eV unless otherwise noted. All strengths are reported in meV in the lab frame unless noted otherwise.

The history of the measurements of the  $^{19}\text{F} + p$  reaction is tragedy of partial measurements and unpublished results, leading to the schizophrenic datasets that result in such disparate resonance parameters. Each measurement will be considered separately in order to try to come to some understanding of the shortfalls of the measurements.

It is reasonable to start with the Sinclair measurement, the earliest shown. The measurements made by Sinclair as well as other authors [21] in the late 1940s and early 1950s resulted in an adopted gamma width of 2.2 eV. This width was determined by the ratios of the cross-sections of the  $(p,\gamma)$  to the  $(p,\alpha)$ . The alpha width reported in reference [3], the light isotope compilation at that time, was 110 eV. None of the later compilations report a width for the  $\alpha_2$  channel. The present measurement gives a value of only 26 eV. It is thus unsurprising that the gamma widths differ as much as they do. It is worth noting that yield ratio obtained in this experiment, 1.7%, is in relatively good agreement with that of Sinclair. The problem is that different cross-sections were measured for the alpha channels. There are a few possible explanations for the difference in the alpha width. First, the isospin of the state populated by the 669 keV resonance was not known, resulting in an inaccurate assumption that most of the width from this state came from the  $(p,\alpha_2)$  channel [12]. If it was assumed that the alpha channel carried most of the width, then it would force the gamma channel to be very strong in order to account for the observed cross-section. On the other hand, if the proton channel carries most of the width (as is the case), the gamma channel can be much more modest and the expected capture cross-section would still be the same. Secondly, all previous published measurements, in particular, those done in the late 40s and early 50s treated the yields as if they came solely from a single resonance, neglecting the effect of tailing from near-by resonances. There is a resonance at 597 keV with a total width

of  $>30\text{keV}$ . As can be seen in figure 3.18, the 669 resonance sits on top of the tail from the 597. The use of thick targets, typically ideal for absolute cross-section measurements, will only make this problem worse. Further measurements did not revisit the gamma-ray partial width for the 669 resonance.

The Subotić dataset was measured relative to the yield from the 669 keV state. They used the resonance width from Ajzenberg-Selove's 1972 compilation, exactly the values that were in disagreement before. If the Subotić data is normalized to resonance strength of 0.33 eV obtained in this measurement, the agreement is quite reasonable, with the exception of the 340 keV resonance. The excitation function obtained by Subotić for the 340 keV resonance disagrees with the excitation function obtained in this measurement. Fortunately, Subotić included the excitation function so that they could be compared. His yield for the 340 keV resonance is approximately twice that for the 484 resonance. Furthermore, Subotić calculated the strengths based on the ratio of the areas under the resonance shape, basically assuming a very thick target without correcting for the total resonance width. The targets used by Subotić were of comparable thickness to the total width of the 669 resonance. The total widths of the resonances in this region range from less than 1 keV up to 30 keV, meaning that corrections for target thickness and total width are essential. Since the total widths for the 340 and 484 differ by a factor of three, this effect should be significant.

The measurements by Keszthelyi and Berkes had the significant advantage over other authors of measuring multiple channels. This helps to remove the uncertainty in the dominant component of the total width. The gamma-widths are about a factor of two higher than those seen in this work with a notable exception of the 597 keV resonance. No excitation functions are shown, so it is not possible to comment directly on the interpretation. Other authors looked for but did not see

Calculated Yield  $\Gamma_{\gamma}=12$  eV for 597 Resonance

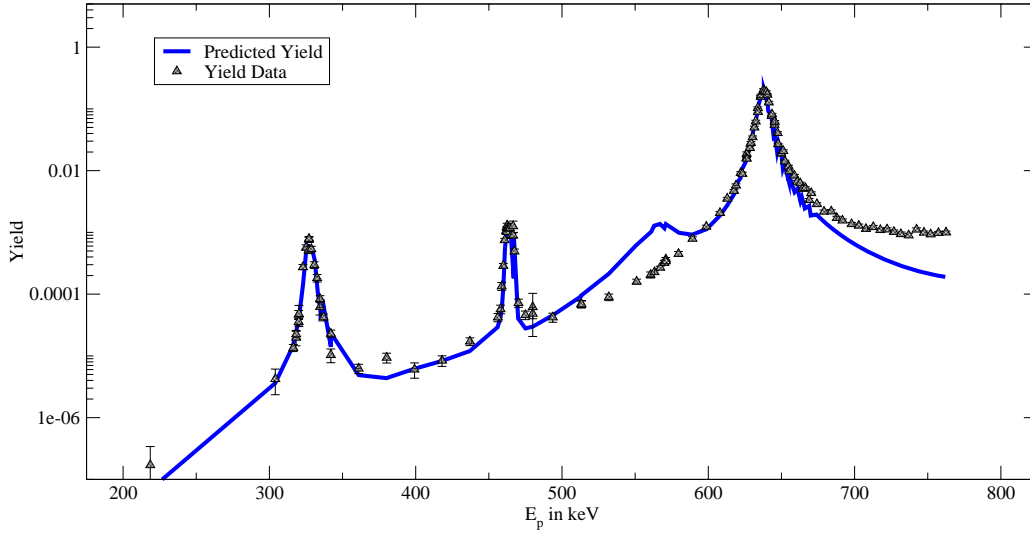


Figure 4.1. The predicted yield the 507 keV resonance with a 12 eV partial width for  $\Gamma_{\gamma_1}$  is illustrated. Clearly this is inconsistent with the data.

such strength. Subotić reports a weaker value of 4.14 eV, which would be pushed further downward if the smaller strength seen in this work were to be used. Clifford saw no contribution at 597 [16]. No evidence was seen in this measurement of a width approaching 12 eV. For comparison, figure 4.1 shows the predicted yield for this experiment had the gamma partial width been 12 eV. It has been suggested that there were impurities in the target which contaminated the spectrum. The deviation of the strengths of Keszthelyi and Berkes from those reported here arose primarily from the proton widths which Berkes and Keszthelyi took from the 1959 compilation [3]. The only measured proton width was for the 484 keV state.

This reduction of the resonance strengths for the  $(p,\gamma)$  channel results in even smaller stellar reaction rates for  $^{19}\text{F}(p,\gamma)$ , closing the lid completely on breakout from the CNO cycle. This validates the typical assumption that breakout reactions

need not be included as Ne production is negligible.

## 4.2 Astrophysical Implications

When this work was begun, the thought was that there were several scenarios in which the assumption that the CNO was closed could be flawed. The resonance at 597 keV is very broad, meaning that the anomalous strength observed by Berkes *et al.* could well tail down into astrophysically relevant temperatures. No measurements had been made of the lowest-lying (and thus closest to stellar burning temperatures) known resonance at 224 keV. Constructive resonant interference could enhance the reaction rate by as much as 50%. It is important to remember that even a small leak would be important because the CNO cycle is a catalytic process. The same seeds get used over and over again. Even a leak of 0.1%, in a scenario where the same seeds were used thousands of times, would have a huge impact.

What was observed, instead, seems to be closing the door at every opportunity for breakout. The resonance strengths for all of the resonances were lowered. No strength was seen at all for the 224 keV resonance. The anomalous strength Berkes *et al.* observed for the 597 resonance appears to be just that—an anomaly in their measurement. The interference terms appear to be destructive.

All of the effects work to push the reaction rate down. Figure 4.2 shows the effect of the new measurement on the reaction rate compared to the standard values of Caughlin and Fowler [14]. There is a reduction across the board of almost a factor of four in the rate.

A similar effect is seen on the rate of stellar  $^{20}\text{Ne}$  production. A simple isobaric, isothermal reaction network code was used to calculate the expected yield using the reaction network given in appendix B. The code was courtesy of Frank Timmes [46] and modified to include breakout to  $^{20}\text{Ne}$ . The resulting  $^{20}\text{Ne}$  production can be

## Stellar Reaction Rates

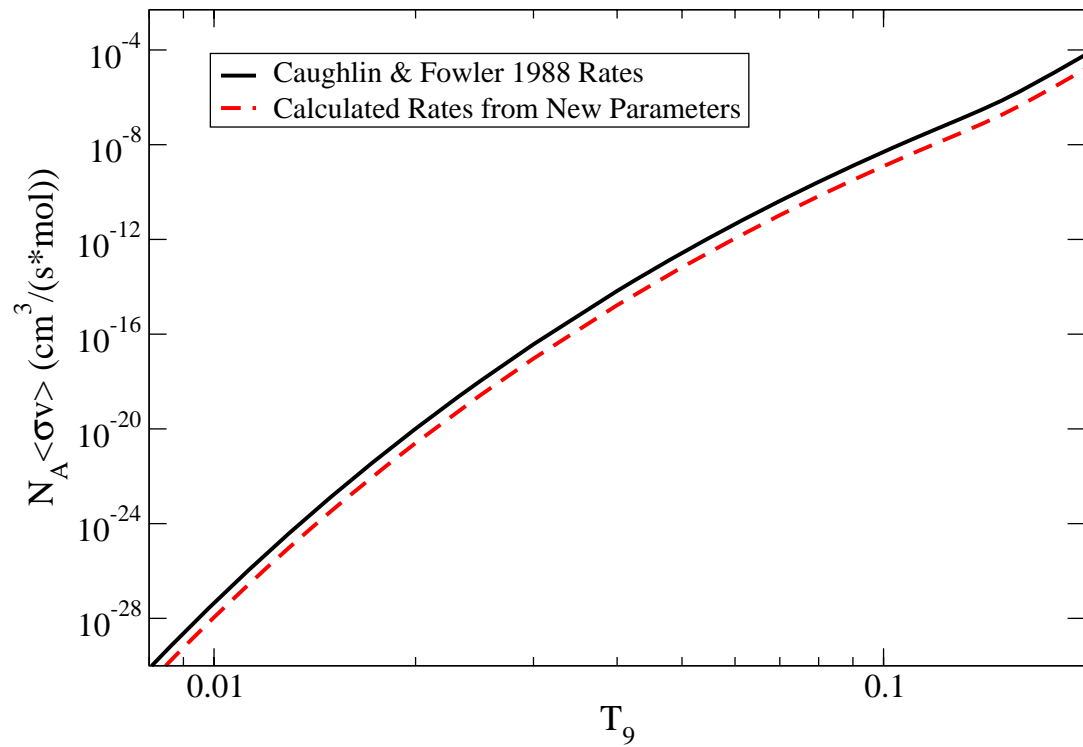


Figure 4.2. The reaction rate obtained from the new measurement is compared with the standard rates of Caughlin and Fowler. The rates are reduced by about a factor of four over the relevant temperature range.

Ne Production,  $X_{\text{Ne, sun}}=1.7 \times 10^{-3}$ ,  $X_{\text{CNO, sun}}=1.34 \times 10^{-2}$

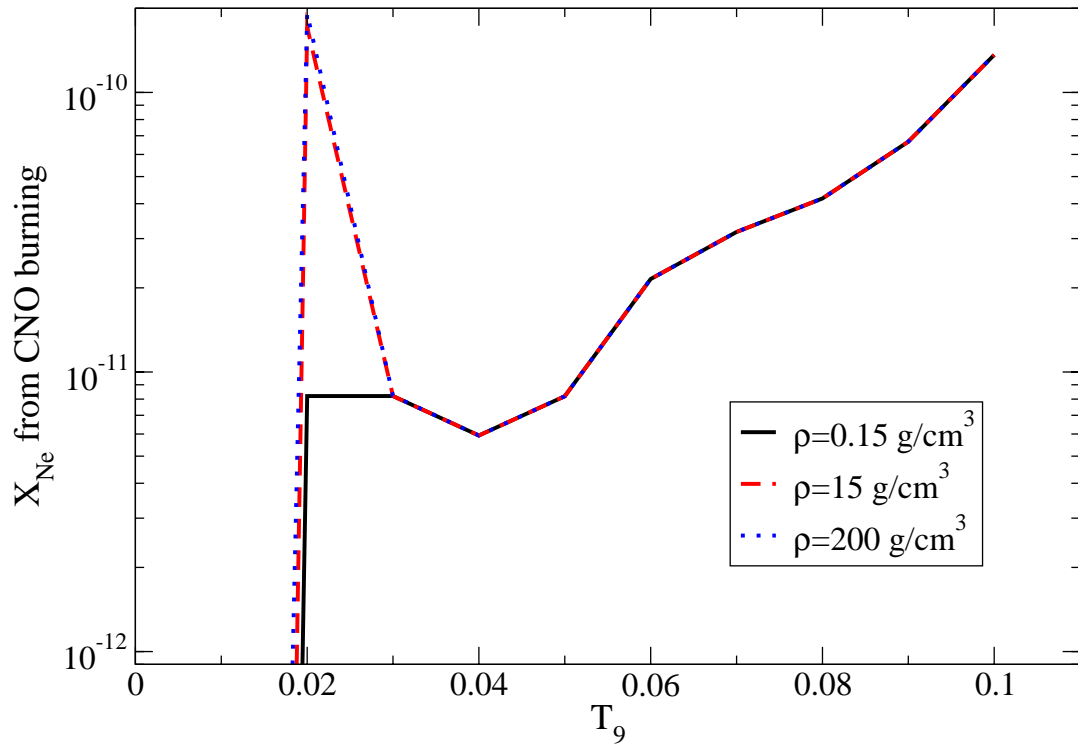


Figure 4.3. The production of neon during CNO cycle nucleosynthesis is shown above. The neon production remains far below the level of neon present in the solar system or the level of CNO isotopes present in a typical star.

seen in figure 4.3.

There are two things to look for. One, does the production contribute significantly to the amount of neon that is present at the end of the CNO cycle? Two, does the neon production impact the amount of CNO isotopes present in the star? The answer to both of these questions is a resounding “No.” The mass-fraction of neon in a modern star is on the order of  $10^{-3}$ . At best, a production on the order of  $10^{-10}$  is observed, a full seven orders of magnitude smaller. The same situation exist for the question of whether CNO isotopes are depleted. Any depletion is on

the order of one part in  $10^8$  over the entire CNO burning time scale, so small that it cannot have any possible effect on the CNO burning times or temperatures.

Together this says that CNO is completely closed. Even though a significant portion of the CNO isotopes start as  $^{16}\text{O}$ , already outside of the first CNO cycle, even if the CNO-II and CNO-III cycles are open at certain temperatures, the  $^{19}\text{F}(p,\alpha)$  reaction firmly closes the CNO cycle with no breakout to  $^{20}\text{Ne}$ .

APPENDIX A

ELECTRONICS ABBREVIATIONS

TABLE A.1

## ELECTRONICS ABBREVIATIONS

Abbreviation	Manufacturer	Description
BNC PB-4	Brookhaven Nucl. Corp.	Precision Pulse Generator
J 65	Jorway	NIM Register
KS 3610	Kinetic Systems	Hex Scaler
L AL688	Lecroy	Level Adapter
L 429A	Lecroy	Logic FIFO
L 4434	Lecroy	16 Channel Scaler
L 4616	Lecroy	ECL-NIM-ECL Level Translator
LF 4000	Ortec	Logic FIFO
O AD811	Ortec	Octal 2k ADC
O AD413A	Ortec	Quad 8k ADC
O CF8000	Ortec	Octal CFD
O CO4020	Ortec	Quad Four Input Logic Unit
O GG8000	Ortec	Octal Gate Generator
O RD2000	Ortec	Rate Divider
O 439	Ortec	Current Digitizer
O 566	Ortec	TAC
O 567	Ortec	TAC/SCA
O 572	Ortec	Spectroscopy Amplifier
O 579	Ortec	Fast Filter Amplifier
O 660	Ortec	Dual 5kV HV Power Supply
O 671	Ortec	Spectroscopy Amplifier
O 672	Ortec	Spectroscopy Amplifier
O 863	Ortec	Quad Timing Filter Amplifier
PS 744	Phillips Scientific	Quad Linear Gate FIFO
Prescaler	Custom ND module	TTL Prescaler
PS 726	Phillips Scientific	Level Translator
PS 752	Phillips Scientific	Logic FIFO with Master Veto
PS 754	Phillips Scientific	Quad Four-Fold Logic Unit
PS 755	Phillips Scientific	Quad Four-Fold Logic Unit
PS 778	Phillips Scientific	16 Channel Variable Amplifier
PS 779	Phillips Scientific	32 Channel Scintillator Amplifier
T 454	Tennelec	Quad CFD
TC 952	Tennelec	HV Power Supply
W 404	Wiener D	Quad Sum and Invert

## APPENDIX B

### CNO NETWORK

For simplicity, the time derivative  $\frac{d}{dt}$  is indicated by an upper dot. Secondly, rather than looking at the evolution in terms of total abundance, it will be tracked as molar fraction  $Y_i$ , defined as the moles of substance  $i$  per gram of total material. In order to distinguish the rates for the breakout reactions, a superscript has been added to indicate whether the  $\alpha$ -channel rate or the  $\gamma$ -channel rates is needed. If no superscript is present, then the  $\gamma$ -channel should be assumed.

$$\begin{aligned}
\dot{Y}_{12C} &= -\lambda_{1H^{12}C} Y_{1H} Y_{12C} + \lambda_{1H^{15}N}^{\alpha} Y_{1H} Y_{15N} \\
\dot{Y}_{13N} &= -\lambda_{13N} Y_{13N} + \lambda_{1H^{12}C} Y_{1H} Y_{12C} \\
\dot{Y}_{13C} &= -\lambda_{1H^{13}C} Y_{1H} Y_{13C} + \lambda_{13N} Y_{13N} \\
\dot{Y}_{14N} &= -\lambda_{1H^{14}N} Y_{1H} Y_{14N} + \lambda_{1H^{13}C} Y_{1H} Y_{13C} + \lambda_{1H^{17}O}^{\alpha} Y_{1H} Y_{17O} \\
\dot{Y}_{15O} &= -\lambda_{15O} Y_{15O} + \lambda_{1H^{14}N} Y_{1H} Y_{14N} \\
\dot{Y}_{15N} &= -\lambda_{1H^{15}N}^{\alpha} Y_{1H} Y_{15N} - \lambda_{1H^{15}N}^{\gamma} Y_{1H} Y_{15N} + \lambda_{1H^{18}O}^{\alpha} Y_{1H} Y_{18O} \\
&\quad + \lambda_{15O} Y_{15O} \\
\dot{Y}_{16O} &= -\lambda_{1H^{16}O} Y_{1H} Y_{16O} + \lambda_{1H^{15}N}^{\gamma} Y_{1H} Y_{15N} + \lambda_{1H^{19}F}^{\alpha} Y_{1H} Y_{19F} \\
\dot{Y}_{17F} &= -\lambda_{17F} Y_{17F} + \lambda_{1H^{16}O} Y_{1H} Y_{16O} \\
\dot{Y}_{17O} &= -\lambda_{1H^{17}O}^{\alpha} Y_{1H} Y_{17O} - \lambda_{1H^{17}O}^{\gamma} Y_{1H} Y_{17O} + \lambda_{17F} Y_{17F} \\
\dot{Y}_{18F} &= -\lambda_{18F} Y_{18F} + \lambda_{1H^{17}O} Y_{1H} Y_{17O} \\
\dot{Y}_{18O} &= -\lambda_{1H^{18}O}^{\alpha} Y_{1H} Y_{18O} - \lambda_{1H^{18}O}^{\gamma} Y_{1H} Y_{18O} + \lambda_{18F} Y_{18F} \\
\dot{Y}_{19F} &= -\lambda_{1H^{19}F}^{\alpha} Y_{1H} Y_{19F} - \lambda_{1H^{19}F}^{\gamma} Y_{1H} Y_{19F} + \lambda_{1H^{18}O}^{\gamma} Y_{1H} Y_{18O} \\
\dot{Y}_{20Ne} &= +\lambda_{1H^{19}F}^{\gamma} Y_{1H} Y_{19F} \\
\dot{Y}_{4He} &= +\lambda_{1H^{15}N}^{\alpha} Y_{1H} Y_{15N} + \lambda_{1H^{17}O}^{\alpha} Y_{1H} Y_{17O} + \lambda_{1H^{18}O}^{\alpha} Y_{1H} Y_{18O} \\
&\quad + \lambda_{1H^{19}F}^{\alpha} Y_{1H} Y_{19F} \\
\dot{Y}_H &= -\lambda_{1H^{12}C} Y_{1H} Y_{12C} - \lambda_{1H^{13}C} Y_{1H} Y_{13C} - \lambda_{1H^{14}N} Y_{1H} Y_{14N} \\
&\quad - \lambda_{1H^{15}N}^{\alpha} Y_{1H} Y_{15N} - \lambda_{1H^{15}N}^{\gamma} Y_{1H} Y_{15N} - \lambda_{1H^{16}O} Y_{1H} Y_{16O} \\
&\quad - \lambda_{1H^{17}O}^{\alpha} Y_{1H} Y_{17O} - \lambda_{1H^{17}O}^{\gamma} Y_{1H} Y_{17O} - \lambda_{1H^{18}O}^{\alpha} Y_{1H} Y_{18O} \\
&\quad - \lambda_{1H^{18}O}^{\gamma} Y_{1H} Y_{18O} - \lambda_{1H^{19}F}^{\alpha} Y_{1H} Y_{19F} - \lambda_{1H^{19}F}^{\gamma} Y_{1H} Y_{19F}
\end{aligned}$$

Several comments should be made about the network. First, a few comments can be made about individual isotopes. Note that hydrogen is only destroyed in this network. Since the process under consideration is a hydrogen burning mechanism, that is to be expected. Second, helium is only produced and never destroyed. At CNO-cycle temperatures, the rate for helium burning reactions is so slow that any

helium consumption is negligible. Several  $\beta$ -unstable isotopes are produced in the burning sequences. In the above network, they are always assumed to decay to stable isotopes before any further proton-capture reaction takes place. Finally, the network is assumed to stop at  $^{20}\text{Ne}$ .

## APPENDIX C

### MAGNET REFRESHING PROCEDURE

The following instructions were given to all accelerator operators throughout the experiment.

**Always go Down in B-Field** Because of the Hysteresis of the magnet, there is a significant energy shift based on magnet history. Therefore, it is important that we only go down in Energy. If you need to go up, use the following procedure to make sure that the hysteresis curve is reset.

1. The Analyzing magnet setting should be 10.14. If it is not, change it to that value.
2. In slit control, change energies to whatever energy you want to get to +5 keV (as in you should be 5 keV above desired energy).
3. Switch the coarse ON
4. Take the charging down, rather quickly. The terminal voltage should drop to zero. Once the Charging is at zero, turn off the Charging.
5. Turn the Master Reference down to 0.00. Wait 5 minutes.
6. Turn the Master Reference up to 75.00. Wait 5 minutes.
7. Turn the Master Reference down until the Energy (slit control) reads your desired energy +5 keV.
8. Bring the Charging back up until slit control grabs the beam.
9. It may take a few minutes for everything to equilibrate. Continue to add charge as necessary to keep the stabilizer balanced.
10. The magnet is now refreshed to run at the new energy. Run as needed, only going down.

## APPENDIX D

### SUMMING CORRECTION COEFFICIENTS

The details for the summing corrections for the 670 keV resonance in  $^{27}\text{Al}(p,\gamma)$  and the decay of  $^{60}\text{Co}$  are given here.

D.1  $^{28m}\text{Si}$ ,  $E_x^R=12239.4$  keV

The level scheme for the decay with gamma-ray indices is shown below. Only those decays with a probability of at least 1% were included in the table and the calculations.

The values of the summing corrections, decay probabilities, and branching ratios are given in table D.1. The terms will be shown below.

The terms for the summing coefficients  $c_i$  are given below.

$$\begin{aligned}
 c_1 &= \frac{1}{B_1}(P_1 P_{14}) \epsilon_{14} \\
 c_2 &= \frac{1}{B_2}(P_2 P_{13} P_{14}) (\epsilon_{13} + \epsilon_{14}) \\
 c_3 &= \frac{1}{B_3}(P_3 P_{12} P_{14}) (\epsilon_{12} + \epsilon_{14}) \\
 c_4 &= \frac{1}{B_4} \{ (P_4 P_{10}) \epsilon_{10} + (P_4 P_{11} P_{14}) (\epsilon_{11} + \epsilon_{14}) \} \\
 c_5 &= \frac{1}{B_5} \{ (P_5 P_8 P_{14}) (\epsilon_8 + \epsilon_{14}) + (P_5 P_9 P_{13} P_{14}) (\epsilon_9 + \epsilon_{13} + \epsilon_{14}) \} \\
 c_6 &= \frac{1}{B_6}(P_6 P_7 P_{14}) (\epsilon_7 + \epsilon_{14})
 \end{aligned}$$

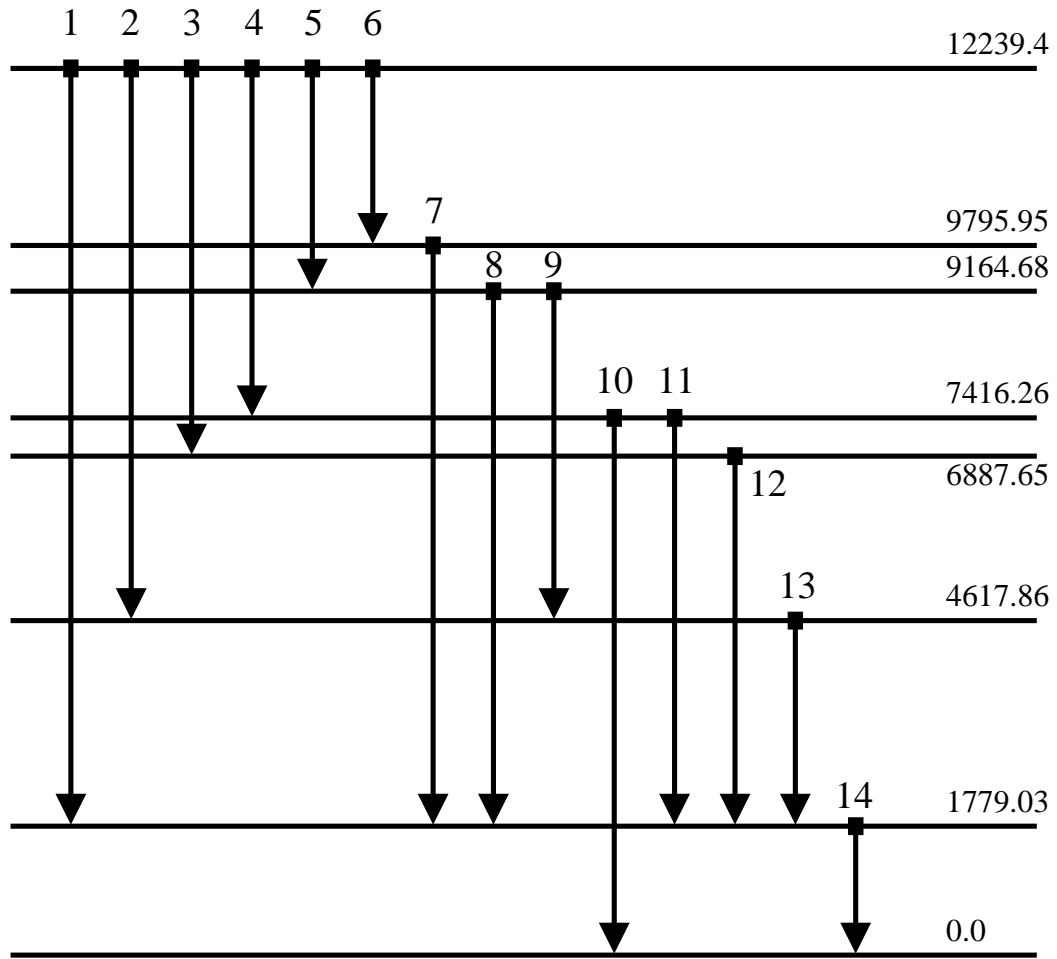


Figure D.1.  $^{28m}\text{Si}$  Decay Schematic,  $E_x^R=12239.4$  keV

TABLE D.1

 $^{28m}\text{Si}$  DECAY SUMMING PARAMETERS,  $E_x^R=12239.4$  keV

$^{27}\text{Al}(p,\gamma)$ , $E_R=679$ keV							
No.	$E_x$	$E_f$	$E_g$	$P_i$	$B_i$	$\epsilon_i$	$c_i$
1	12239.4	1779.03	10460.4	0.43	0.43	0.0839	0.0932
2	12239.4	4617.86	7621.5	0.26	0.26	0.0828	0.181
3	12239.4	6887.65	5351.8	0.014	0.014	0.0832	0.177
4	12239.4	7416.26	4823.1	0.21	0.21	0.0836	0.0884
5	12239.4	9164.68	3074.7	0.026	0.026	0.0871	0.216
6	12294.3	9795.95	2443.5	0.017	0.017	0.0895	0.176
7	9795.95	1779.03	8016.9	1.00	0.017	0.0829	0.183
8	9164.68	1779.03	7385.7	0.55	0.0143	0.0828	0.180
9	9164.68	4617.86	4546.8	0.45	0.0117	0.0839	0.268
10	7416.26	0.0	7416.3	0.94	0.197	0.0828	0.0836
11	7416.26	1779.03	5637.2	0.06	0.0126	0.0830	0.177
12	6887.65	1779.03	5108.6	1.00	0.014	0.0834	0.176
13	4617.86	1779.03	2838.8	1.00	0.272	0.0879	0.180
14	1779.03	0.0	1779.0	1.00	0.760	0.0932	0.120

NOTE: The details for the decay of the 12239.4 keV state of  $^{28}\text{Si}$  are given, including the decay probabilities and total efficiencies for each line. The energies of the states are taken from [24] while the decay scheme is from [39].

$$\begin{aligned}
c_7 &= \frac{1}{B_7}(P_6P_7P_{14}) (\epsilon_6 + \epsilon_{14}) \\
c_8 &= \frac{1}{B_8}(P_5P_8P_{14}) (\epsilon_5 + \epsilon_{14}) \\
c_9 &= \frac{1}{B_9}(P_5P_9P_{13}P_{14}) (\epsilon_5 + \epsilon_{13} + \epsilon_{14}) \\
c_{10} &= \frac{1}{B_{10}}(P_4P_{10}) \epsilon_4 \\
c_{11} &= \frac{1}{B_{11}}(P_4P_{11}P_{14}) (\epsilon_4 + \epsilon_{14}) \\
c_{12} &= \frac{1}{B_{12}}(P_3P_{12}P_{14}) (\epsilon_3 + \epsilon_{14}) \\
c_{13} &= \frac{1}{B_{13}} \{ (P_2P_{13}P_{14}) (\epsilon_2 + \epsilon_{14}) + (P_5P_9P_{13}P_{14}) (\epsilon_5 + \epsilon_9 + \epsilon_{14}) \} \\
c_{14} &= \frac{1}{B_{14}} \{ (P_1P_{14})\epsilon_1 + (P_2P_{13}P_{14}) (\epsilon_2 + \epsilon_{13}) + (P_4P_{11}P_{14}) (\epsilon_4 + \epsilon_{11}) \\
&\quad + (P_5P_8P_{14}) (\epsilon_5 + \epsilon_8) + (P_5P_9P_{13}P_{14}) (\epsilon_5 + \epsilon_9 + \epsilon_{13}) \\
&\quad + (P_6P_7P_{14}) (\epsilon_6 + \epsilon_7) \}
\end{aligned}$$

The terms for the branching ratios  $B_i$  are given below.

$$\begin{aligned}
B_1 &= P_1 \\
B_2 &= P_2 \\
B_3 &= P_3 \\
B_4 &= P_4 \\
B_5 &= P_5 \\
B_6 &= P_6 \\
B_7 &= P_6P_7 \\
B_8 &= P_5P_8 \\
B_9 &= P_5P_9 \\
B_{10} &= P_4P_{10}
\end{aligned}$$

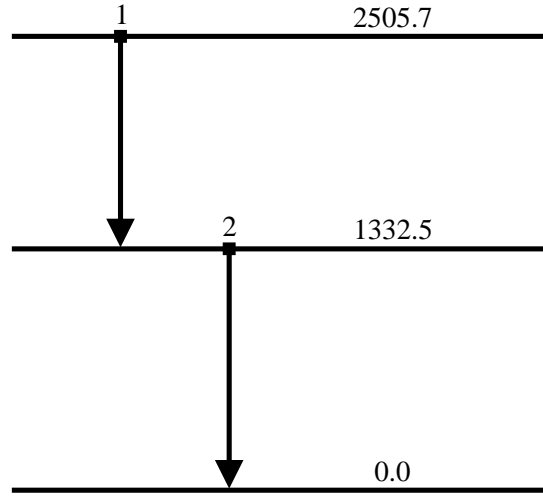


Figure D.2.  $^{60m}\text{Ni}$  Decay Schematic,  $E_x=2505.7$  keV

$$B_{11} = P_4 P_{11}$$

$$B_{12} = P_3 P_{12}$$

$$B_{13} = P_2 P_{13} + P_5 P_9 P_{13}$$

$$B_{14} = P_1 P_{14} + P_2 P_{13} P_{14} + P_3 P_{12} P_{14} + P_4 P_{11} P_{14} + P_5 P_8 P_{14} \\ + P_5 P_9 P_{13} P_{14} + P_6 P_7 P_{14}$$

D.2  $^{60}\text{Co} \rightarrow ^{60m}\text{Ni}$ ,  $E_x=2505.7$  keV

The level scheme for the decay with gamma-ray indices is shown below. The level scheme is for state of  $^{60}\text{Ni}$  that the Co populates.

The values of the summing corrections, decay probabilities, and branching ratios are given in table D.2. Though they are trivial, for completeness, the calculation of the terms will be shown below.

The terms for the summing coefficients  $c_i$  are given below.

TABLE D.2

 $^{60m}\text{Ni}$  DECAY SUMMING PARAMETERS,  $E_x=2505.7$  keV

$^{60}\text{Co}$ Source							
No.	$E_x$	$E_f$	$E_g$	$P_i$	$B_i$	$\epsilon_i$	$c_i$
1	2505.7	1332.5	1173.2	1.00	1.00	0.0979	0.0966
2	1332.5	0.0	1332.5	1.00	1.00	0.0966	0.0979

NOTE: The summing corrections for the  $^{60}\text{Co}$  source are shown. All energies and decay probabilities for  $^{60}\text{Co}$  are taken from reference [47].

$$c_1 = \frac{1}{B_1}(P_1 P_2) \epsilon_2$$

$$c_2 = \frac{1}{B_2}(P_1 P_2) \epsilon_1$$

The branching ratios  $B_i$  are given below.

$$B_1 = P_1 P_2$$

$$B_2 = P_1 P_2$$

## APPENDIX E

### JN RUNNING PARAMETERS

The parameters for the JN during a typical run are listed here. These were taken from a run at 11:50 AM, 9 December 2004. The settings are values that were set via Labview while the readback values were read either in Labview or an external meter.

TABLE E.1

## JN RUNNING PARAMETERS

Parameter	Setting	Readback Value
Tank Pressure (p.s.i.)		162
Base Vacuum (torr)		$8.5 \times 10^{-7}$
Beam Slits Left (Zero)	99350 (98950)	
Beam Slits Right (Zero)	00004 (98604)	
Beam Slits Top (Zero)	99857 (99457)	
Beam Slits Bottom (Zero)	99605 (99205)	
Anaslits Left (Zero)	00086 (98950)	
Anaslits Right (Zero)	99116 (98950)	
Anaslits Top (Zero)	03035 (98950)	
Anaslits Bottom (Zero)	02830 (98950)	
Ion	p	
Beam Line	(p, $\gamma$ )	
GVM (kV)		400
Corona Current ( $\mu$ A)		20
Column Current ( $\mu$ A)		14
Charging (kV)	6.05	
Up Charge ( $\mu$ A)		97
Focus	72	
Extractor	235	
Magnet (Ion Source)	140	
Gas	163	
Beamline Vacuum (torr)		$1.64 \times 10^{-6}$
Quad A	2.76	
Quad B	2.46	
Vertical Steerer	-8.00	
Anamag Setting	10.14	
Anamag Current (A)		9.43
JN Master Reference	4306	
Anamag Cup ( $\mu$ A)		40
High Energy Slit ( $\mu$ A)		0
Low Energy Slit ( $\mu$ A)		2
Switching Magnet Coarse	067	
Switching Magnet Fine	728	
Target Quad A	461	
Target Quad B	283	
Target MR Coarse	399	
Target MR Fine	196	
Gaussmeter (kG)		0.9928
Horizontal Steerer	-0.80	
Vertical Steerer #2	-0.12	

## BIBLIOGRAPHY

- [1] F. Ajzenberg-Selove, Energy levels of light nuclei  $A = 16-17$ . *Nucl. Phys. A*, 460: 1–110 (1986).
- [2] F. Ajzenberg-Selove, Energy levels of light nuclei  $A = 18-20$ . *Nucl. Phys. A*, 475: 1–198 (1987).
- [3] F. Ajzenberg-Selove and T. Lauritsen, Energy levels of light nuclei. VI. *Nuclear Physics*, 11: 1–340 (1959).
- [4] E. Anders and N. Grevesse, Abundances of the elements - Meteoritic and solar. *Geochimica et Chosmochimica Acta*, 53: 197–214 (January 1989).
- [5] Application Software Group, *MINUIT-Function Minimization and Error Analysis*. CERN, Geneva, Switzerland (1998), CERN Program Library Long Writeup D506.
- [6] G. B. Arfken and H. J. Weber, *Mathematical Methods for Physicists*. Academic Press, New York (1995).
- [7] F. Azjenberg-Selove, Energy levels of light nuclei,  $A=20$ . *Nucl. Phys. A*, 190: 1 (1972).
- [8] I. Berkes, I. Dézsi, I. Fodor and L. Keszthelyi, The resonances at 483 and 597 keV proton energies in  ${}^{19}\text{F} + \text{p}$  reactions. *Nucl. Phys.*, 43: 103–109 (1963).
- [9] H. Bethe, Energy production in stars. *Phys. Rev.*, 55: 434 (1938).
- [10] P. R. Bevington and D. K. Robinson, *Data Reduction and Error Analysis for the Physical Sciences*. McGraw-Hill, New York, second edition (1992).
- [11] J. M. Blatt and V. F. Weisskopf, *Theoretical Nuclear Physics*. Wiley (1952).
- [12] T. W. Bonner and J. E. Evans, Resonances in the disintegration of fluorine and lithium by protons. *Phys. Rev.*, 73: 666–674 (1948).
- [13] E. M. Burbidge, G. R. Burbidge, W. A. Fowler and F. Hoyle, Synthesis of the elements in stars. *Rev. of Mod. Phys.*, 29: 547 (1957).
- [14] G. R. Caughlan and W. A. Fowler, Thermonuclear reaction rates V. *Atomic Data and Nuclear Data Tables*, 40: 283–334 (1988).
- [15] CERN Development Team (2003).

- [16] E. T. Clifford, *An Investigation of the Isospin Properties of the 13.411 MeV State of  $^{20}\text{Ne}$* . Master's thesis, University of Toronto (October 1974).
- [17] J. D. Cockroft and T. S. Walton, Experiments with high velocity positive ions. II. the disintegration of elements by high velocity protons. *Proceedings of the Royal Society of London*, 137: 229–242 (1932).
- [18] J. J. Cowan and C. Sneden, Origin and evolution of the elements. In *Origin and Evolution of the Elements*, page 27, Cambridge Univ. Press (2004).
- [19] H. R. Crane, L. A. Delsasso, W. A. Fowler and C. C. Lauritsen, High energy gamma-rays from lithium and fluorine bombarded with protons. *Physical Review*, 46: 531–533 (1934).
- [20] K. Debertin and R. G. Helmer, *Gamma- and X-ray Spectroscopy with Semiconductor Detectors*. North-Holland (1988).
- [21] S. Devons and H. G. Hereward, Proton bombardment of fluorine. *Nature, Lond.*, 162(4113): 331–332 (1948).
- [22] A. Eddington, The internal constitution of the stars. *The Observatory*, 43: 341–358 (1920).
- [23] S. Eidelman, K. Hayes, K. Olive and *et al.*, Review of Particle Physics. *Physics Letters B*, 592: 1+ (2004).
- [24] P. M. Endt, Energy levels of  $A = 21-44$  nuclei (IV). *Nucl. Phys. A*, 521: 1–400 (1990).
- [25] G. K. Farney, H. H. Given, B. D. Kern and H. T. M., High energy gamma rays from the proton bombardment of fluorine. *Physical Review*, 97: 720–725 (1955).
- [26] W. A. Fowler, G. R. Caughlin and B. A. Zimmerman, Thermonuclear reaction rates. *Annual Reviews of Astronomy and Astrophysics*, 5: 525 (1967).
- [27] W. A. Fowler, C. C. Lauritsen and T. Lauritsen, Gamma-Radiation from excited states of light nuclei. *Rev. Mod. Phys.*, 20: 236–277 (1948).
- [28] H. E. Gove, Resonance reactions, experimental. In P. M. Endt and M. Demeur, editors, *Nuclear Reactions*, volume 1, chapter 6, pages 259–317, Interscience (1959).
- [29] H. E. Gove and A. E. Litherland, Gamma rays from unbound nuclear states formed by charged-particle capture. In F. Ajzenberg-Selove, editor, *Nuclear Spectroscopy: Part A*, pages 260–304, Academic Press (1960).
- [30] N. Grevesse and A. J. Sauval, Solar abundances. In P. Murdin, editor, *Encyclopedia of Astronomy & Astrophysics*, Institute of Physics (2005), <http://eaa.iop.org>.

- [31] R. L. Heath, Scintillation spectrometry: Gamma-ray spectrum catalogue. Technical Report IDO-16880-1, Idaho National Engineering & Environmental Laboratory (1997), Revised Electronic version of 2nd Edition.
- [32] L. Keszthelyi, I. Berkes, I. Demeter and I. Fodor, Resonances in  $^{19}\text{F}+\text{p}$  reactions at 224 and 340 keV proton energies. *Nucl. Phys.*, 29: 241–251 (1962).
- [33] G. F. Knoll, *Radiation Detection and Measurement*. Wiley, third edition (2000).
- [34] K. S. Krane, *Introductory Nuclear Physics*. Wiley (1988).
- [35] W. R. Leo, *Techniques for Nuclear and Particle Physics Experiments*. Springer-Verlag, New York, second revised edition (1994).
- [36] K. Lodders, Solar system abundances and condensation temperatures of the elements. *Ap. J.*, 591: 1220–1247 (2003).
- [37] H. Lorenz-Wirzba, *Untersuchung von (p, $\alpha$ )-reaktionen Unterhalb der Coulombsbarriere*. Ph.D. thesis, Westfälischen Wilhelms-Universität zu Münster (1978).
- [38] P. B. Lyons, J. W. Toevs and D. G. Sargood, Total yield measurements in  $^{27}\text{Al}(\text{p},\gamma)^{28}\text{Si}$ . *Nucl. Phys. A*, 130: 1–24 (1969).
- [39] M. A. Meyer, I. Venter and D. Reitmann, Energy levels of  $^{28}\text{Si}$ . *Nucl. Phys. A*, 250: 235–256 (1975).
- [40] W. H. Press, S. A. Teukolsky, W. T. Vetterling and B. P. Flannery, *Numerical Recipes in FORTRAN 77: The Art of Scientific Computing*, volume 1. Cambridge, second edition (1992).
- [41] C. Rolfs and W. Rodney, *Cauldrons in the Cosmos*. University of Chicago Press, Chicago (1988).
- [42] R. M. Sinclair, Gamma radiation from certain nuclear reactions. *Phys. Rev.*, 93: 1082–1086 (1954).
- [43] K. M. Subotić, R. Ostojić and B. Z. Stepančić, Study of the  $^{19}\text{F}(\text{p},\gamma)^{20}\text{Ne}$  radiative capture reaction from 0.2–1.2 MeV. *Nuclear Physics A*, 331: 491–501 (1979).
- [44] R. G. Thomas, On the determination of reduced widths from the one-level dispersion formula. *Phys. Rev.*, 81: 148–149 (1951).
- [45] D. R. Tilley, C. M. Cheves, J. H. Kelley, S. Raman and H. R. Weller, Energy levels of light nuclei  $a=20$ . *Nuclear Physics A*, 636: 249–364 (1998).
- [46] F. Timmes, public\_CNO.f. The JINA School on Tools and Toys in Nuclear Astrophysics: Astrophysical Reaction Networks (June 2005).
- [47] J. K. Tuli, Nuclear data sheets for  $A=60$ . *Nucl. Data Sheets*, 100: 347–481 (2003).

- [48] P. J. Turner and Grace Development Team, Grace-5.1.18. <http://plasma-gate.weizmann.ac.il/Grace> (2005), Distributed under the GNU General Public License.
- [49] C. Ugalde, *The  $^{19}\text{F}(\alpha,p)^{22}\text{Ne}$  reaction and the destruction of  $^{19}\text{F}$* . Ph.D. thesis, University of Notre Dame (2005).
- [50] M. Wiescher, J. Görres and H. Schatz, Break-out reactions from the CNO cycles. *J. Phys. G: Nucl. Part. Phys.*, 25: R133–R161 (1999).
- [51] J. F. Ziegler and J. P. Biersack, SRIM-2003.26 (2003).